

**PRE-CLINICAL EVALUATION OF THERANOSTIC
[¹⁷⁷Lu]Lu-PSMA617 PROSTATE CANCER TREATMENT IN COMBINATION
WITH ADJUVANT AGONISTIC OX40-TARGETING**

by

Marin Simunic

MD, Charité - Universitätsmedizin Berlin, 2012

A THESIS SUBMITTED IN PARTIAL FULFILLMENT OF
THE REQUIREMENTS FOR THE DEGREE OF

MASTER OF SCIENCE

in

THE FACULTY OF GRADUATE AND POSTDOCTORAL STUDIES
(Interdisciplinary Oncology)

THE UNIVERSITY OF BRITISH COLUMBIA

(Vancouver)

August 2020

© Marin Simunic, 2020

The following individuals certify that they have read, and recommend to the Faculty of Graduate and Postdoctoral Studies for acceptance, the thesis entitled:

Pre-clinical evaluation of theranostic [¹⁷⁷Lu]Lu -PSMA617 prostate cancer
treatment in combination with adjuvant agonistic OX40-targeting

submitted by Marin Simunic in partial fulfillment of the requirements for
the degree of Master of Science
in Interdisciplinary Oncology

Examining Committee:

Calum Macaulay, Interdisciplinary Oncology
Supervisor

Kuo-Shyan Lin, Interdisciplinary Oncology
Supervisory Committee Member

Urs Hafeli, Faculty of Pharmaceutical Sciences
Additional Examiner

Wan Lam, Interdisciplinary Oncology
Chair

Additional Supervisory Committee Members

Cathie Garnis, Interdisciplinary Oncology
Supervisory Committee Member

Abstract

Prostate cancer represents a significant disease burden worldwide. While recent advancements in diagnostics and therapy have increased both overall and progress-free survival in PCa, relapses are common, and progression to the metastatic phenotype continues to block therapeutic efforts, often leading to fatal outcomes in spite of multimodal therapy. In consequence, more potent treatment options are the subject of dynamic pre-clinical and clinical research. A substantial part of this research focuses on combination treatment strategies, such as therapy using theranostic targeted radioligands combined with immunotherapeutics. We proposed co-targeting of OX40, a T-cell surface antigen using an agonistic antibody OX86, in combination with a lutetium-177-labelled, PSMA antigen-binding radiopharmaceutical [¹⁷⁷Lu]Lu-(DKFZ)-PSMA617.

Based on the promising results from pre-clinical and clinical trials, we hypothesized that the combined treatment would have greater therapeutic effect than either treatment alone. First we isolated four clones of a doxycycline (Tet-On)-inducible cell line, deriving from a commonly used TRAMP-C2 cell line. Next, we conducted imaging and biodistribution studies and were able to prove inducibility of PSMA protein-expression upon induction, in a non-immunogenic model. Induction was visualized in PET/CT scans as increased [¹⁸F]DCFPyL uptake in the inoculated tumour region, and evident from the dosimetry analysis of gamma-counted organ samples *ex vivo*, whereas tumour tissue tracer uptake amounted to up to 26% ID/g.

Cells derived from excised tumours were viable in an immunocompetent model, which facilitated experiments aimed at comparing therapeutic efficacy of the proposed combination treatment. In the adapted therapy studies, tumour growth inhibition was achieved in both

treatment groups (^{177}Lu]Lu-PSMA617 alone and in combination with OX86 antibody). Growth dynamics of untreated tumours showed a high degree of variability, which negatively impacted the interpretative value of the results. However, underlying processes causing such non-uniformity of results were delineated in another set of experiments - the pilot autoradiography (betaimaging) and tissue architecture imaging studies concluding this thesis, identifying pronounced intra- and intertumoural heterogeneity.

To conclude, successful induction of PSMA-expression and the viability of used clones in immunocompetent models hold promise of applying this system as a gene-reporting tool, and further subcloning of the cell populations can pave a way for expanded therapy studies.

Lay Summary

For patients and the healthcare system, metastatic prostate cancer represents a challenge.

Numerous new treatments and treatment combinations are being identified, that can improve the quality of life and increase life expectancy for prostate cancer patients. Herein we studied a combination treatment consisting of a radioactive molecule called lutetium-177-PSMA617 and an immunotherapeutic called OX86, in laboratory experiments. Lutetium-177-PSMA617 has already shown promising results in clinical trials and larger trials are currently underway in order to assess whether it qualifies as a candidate for standard therapy of prostate cancer. OX40 is an immunotherapeutic with some already available results in clinical trials supporting its use. In our experiments, we first successfully engineered prostate cancer cells that can be used for our experiments. We could not confirm with certainty that the combination treatment was more effective than each of the drugs alone; however, the combination took certain effect in reducing tumour volume.

Preface

A version of Chapter 3 is currently being prepared for submission [M Simunic, J Joshi, H Merkens, N Colpo, HT Kuo, JJ Lum, F Bénard. Non-invasive in vivo proof of PSMA-expression in a novel inducible tumour model.] J Joshi and I were the lead members on this project. J Joshi conducted transfection procedures and isolated inducible TRAMP-C2 clones, J Pan, HT Kuo and Z Zhang performed the chemical and radiochemical synthesis of radiotracers. I conducted the biological evaluation experiments (biodistribution, monitoring). H Merkens assisted with animal procedures and monitoring. N Colpo, N Hundal-Jabal and H Merkens performed SPECT/CT and PET/CT image acquisition. H Merkens and K Gitschtaler assisted with cell culture procedures. J Lum and F Bénard were the supervisory authors and were both heavily involved in experimental design and manuscript input. The manuscript was drafted and finalized by me with critical input from J Lum, KS Lin and F Bénard.

The remainder of the thesis was contributed to as follows: for Aim 1, TRAMP-C2 clones 1, 14, 16 and 19 were generated, isolated and identified by Jay Joshi; subclone 16-Q13 was identified and isolated by Helen Merkens and me; inoculation and monitoring was fulfilled by Helen Merkens, Katrin Gitschtaler and me; FACS studies were performed by Helen Merkens, Jay Joshi, Julie Rousseau and me; for Aim 2-a, inoculation and monitoring was performed by Helen Merkens, Katrin Gitschtaler and me. For Aim 2-b, Jennifer Baker provided input regarding study design and performed the majority of the staining and imaging procedures, together with Jason Crawford who performed autoradiography studies. Navjit Hundal, Nadine Colpo, Hsiou-Ting Kuo, Katrin Gitschtaler and Helen Merkens assisted with biodistribution studies. Tumour harvesting, *ex vivo* processing and subcloning was conducted Helen Merkens, Katrin Gitschtaler

and me. Helen Merkens and I performed intraperitoneal doxycycline administration. Nadine Colpo, Helen Merkens and Hsiou-Ting Kuo performed lutetium- and fluorine-labelled tracer administration. Statistical analysis was performed by me.

In vivo studies were performed in accordance with the University of British Columbia Animal Care and Use Program protocol numbers #A16-0128 and #A16-0290 and the Biosafety Certificate #B15-0037.

Table of Contents

Abstract	iii
Lay Summary	v
Preface	vi
Table of Contents	viii
List of Tables	xiii
List of Figures	xiv
List of Abbreviations	xvi
1 Introduction	1
1.1 Prostate Cancer	1
1.1.1 Therapy of Prostate Cancer	2
1.1.2 Nuclear Medicine in Cancer Management	3
1.1.2.1 Theranostics	4
1.2 PSMA	7
1.2.1 PSMA-Targeting Radiopharmaceuticals	8
1.2.1.1 Lutetium-177-labelled Theranostic Agents in Cancer	
Management	9
1.2.1.1.1 [¹⁷⁷ Lu]Lu-PSMA617	11
1.3 Cancer Immunotherapy	12
1.3.1 Immune Checkpoint Blocking Therapeutics	13
1.3.2 PCa Immunotherapy	17
	viii

1.3.3 OX-40	20
1.3.3.1 OX86	23
1.4 Abscopal Effects of Radiation	24
1.5 Tumour Model	25
1.6 Thesis Aims	26
1.6.1 Rationale	26
1.6.2 Hypothesis	28
1.6.3 Specific Aims	28
2 Materials and Methods	30
2.1 Reagents and Instrumentation	30
2.2 Peptide Synthesis	30
2.3 Synthesis of [¹⁷⁷ Lu]Lu-PSMA-617	30
2.4 [¹⁸ F]DCFPyL Radiolabeling	31
2.5 Statistical tests	31
3 Cell Line Validation	32
3.1 Introduction	32
3.1.1 Tetracycline-Inducible Protein Expression	32
3.1.2 PSMA-Expression in Prostate Cancer Models	33
3.2 Materials and Methods	33
3.2.1 Peptide Synthesis	33
3.2.2 Synthesis of [¹⁷⁷ Lu]Lu-PSMA617.....	34

3.2.3 [¹⁸ F]DCFPyL Radiolabeling	35
3.2.4 Cell Cultures	35
3.2.5 Transfected TRAMP Cells	36
3.2.6 Isolating PSMA-expressing clonal populations	36
3.2.7 <i>In vivo</i> Studies	37
3.2.7.1 Quantification and visualization of PSMA-expression in an	
immunocompromised model	37
3.2.7.1.1 PET/CT Studies	39
3.2.8 Repassaging TRAMP-C2 Cells	39
3.2.9 <i>In vivo</i> proof of induced PSMA-expression in an	
immunocompetent model	40
3.3 Results	41
3.3.1 Transfected TRAMP Cells	41
3.3.2 Flow Cytometry	41
3.3.3 <i>In Vivo</i> Proof of Induced PSMA-Expression in an	
Immunocompromised Model	43
3.3.4 <i>In Vivo</i> Proof of Induced PSMA-Expression in an	
Immunocompetent Model	46
3.4 Discussion	49
4 PSMA617/Anti-OX40 Antitumour Potency Assessment	51
4.1 Introduction	51
4.2 Materials and Methods	51
4.2.1 Reagents And Instrumentation; Peptide And	

Radiotracer Synthesis	51
4.2.2 Cell Cultures	52
4.2.2.1 Transfected TRAMP Cells	53
4.2.3 Isolating PSMA-Expressing Clonal Populations	53
4.2.4 In Vivo Studies	54
4.2.4.1 PET/CT Studies	54
4.2.5 Repassaging TRAMP-C2 Cells	55
4.2.6 <i>In Vivo</i> Proof of Induced PSMA-Expression in an Immunocompetent	
Model	55
4.2.7 Initial Therapy Study Protocol	56
4.3 Results and Discussion	66
4.3.1 Tumour Growth Inhibition Curves	66
4.3.2 Survival	77
4.3.3 SPECT Imaging	78
4.4. Conclusion	84
5 Delineating Patterns of Tissue Response to PSMA617/OX40 Therapy	86
5.1 Introduction	86
5.2 Materials and Methods	86
5.2.1 <i>Ex Vivo</i> Studies	86
5.3 Results and Discussion	87
5.3.1 Autoradiography Studies	87
5.3.2 Tissue Marker Registration – Antibody- and Click-Chemistry Staining and	
Fluorescence Microscopy	89

5.3.3 Co-Registration and Interpretation	90
6 Conclusion and Future Directions	95
6.1 Results Summary	95
6.2 Future Directions	96
6.3 Concluding Remarks	98
Bibliography.....	99
Appendices	142
Appendix A – FACS Studies On TRAMP-C2 Clones	142
Appendix B – Growth Inhibition Curves	143
Appendix C – FACS Studies On Excised Tumours	150

List of Tables

Table 1.1. Common beta-emitters in use in nuclear medicine	6
Table 1.2. PSMA ligands used in therapy/palliation of PCa	10
Table 1.3. Immune checkpoint inhibiting agents approved for cancer therapy	15
Table 1.4. Studies reporting use of immune checkpoint inhibitors in non-melanoma patients ...	16
Table 1.5. Relevant clinical trials on prostate cancer immunotherapy	18
Table 3.1. Biodistribution results for C1R1 and C1RL	48
Table 4.1. Size of treatment groups according to the initial therapy study protocol	58
Table 4.2. Simplified scheme of study timepoints according to the initial protocol	62
Table 4.3. Simplified scheme of study timepoints in the first-pass experiment, according to the adapted protocol	63
Table 4.4. Size of treatment groups according to the adapted therapy study protocol	64
Table 4.5. Simplified scheme of study timepoints in the second-pass experiment according to the adapted protocol	65
Table 4.6. Tumour uptake values in %ID/g at day 3 and day 9 post injection	83

List of Figures

Figure 1.1. Scheme of currently available prostate cancer therapeutic options	2
Figure 1.2. PSMA homodimer structure scheme	8
Figure 1.3. Chemical structure of PSMA617 - unlabelled bioconjugate and labeled tracers	12
Figure 3.1. Initial flow cytometry study results for 4 hPSMA expressing clones	42
Figure 3.2. Comparison of uptake in induced and uninduced clones 1, 14, 16 and 19	44
Figure 3.3. Comparison of PET/CT images before (left) and after (right)	
doxycycline-induction <i>in Vivo</i>	45
Figure 3.4. PET/CT image of induction in an immunocompetent model	47
Figure 4.1. Proposed therapy study protocol.....	57
Figure 4.2. Tumour volumes in control group.....	66
Figure 4.3. Number of tumours 70 days post inoculation, sorted by volume.....	68
Figure 4.4. Volume of tumours monitored for growth inhibition in Treatment	
Groups #1 and #2	71
Figure 4.5. Volume of tumours monitored for growth inhibition in Treatment Group #1	72
Figure 4.6. Volume of selected tumours monitored for growth inhibition in Treatment	
Group #2, excluding tumours with large volumes at timepoint 1.....	74
Figure 4.7. Volume of selected tumours monitored for growth inhibition in Treatment	
Group #1,excluding tumours with large volumes at timepoint 1, and	
tumours monitored past day 26 post inoculation	75
Figure 4.8. Kaplan-Meier curve showing probability of survival in Treatment Groups #1 (combination treatment with [¹⁷⁷ Lu]Lu-PSMA617 and OX86; n=5) and #2 ...	

($[^{177}\text{Lu}]\text{Lu-PSMA617}$ only; n=5)	77
Figure 4.9. SPECT/CT image 24 hours post injection of $[^{177}\text{Lu}]\text{Lu-PSMA617}$ and the first dose of OX86 antibody, tumour ID C19L1	79
Figure 4.10. SPECT/CT image 24 hours post injection of $[^{177}\text{Lu}]\text{Lu-PSMA617}$ tumour ID tumour ID C9R1	80
Figure 4.11. SPECT/CT images 3 (left) and 5 (right) days post injection of $[^{177}\text{Lu}]\text{Lu-PSMA617}$ and the first dose of OX86 antibody, mouse ID C12RL	82
Figure 5.1. Overlaid beta- and optic images of tumour sections	88
Figure 5.2. Fluorescence microscopy registration/co-registration of markers of proliferation, viability, perfusion and vascularization	90
Figure 5.3. Fluorescence microscopy co-registration of 2-4 different markers of proliferation, viability, perfusion and vascularization	91
Figure 5.4. Fluorescence microscopy images of a section of tumour ID C8RL	92

List of Abbreviations

% ID/g percent injected activity per gram

¹¹¹In indium-111

¹³¹I iodine-131

[¹⁵³Sm]Sm-EDTMP Samarium-153-ethylene diamine tetramethylene phosphonate/samarium-53-
lexidronam; Tradename Quadramet

¹⁷⁷Lu lutetium-177

[¹⁷⁷Lu]Lu-PSMA617 or **[¹⁷⁷Lu]Lu-DKFZ-PSMA617** lutetium-177-labelled vipivotide
tetraxetane— a lutetium-177-labelled PSMA-targeting radioligand; DKFZ stands for
Deutsches Krebsforschungszentrum

¹⁸F fluorine-18

[¹⁸F]DCFPyL 2-(3-{1-carboxy-5-[(6-[¹⁸F]fluoro-pyridine-3-carbonyl)-amino]-
pentyl}ureido)-pentanedioic acid

²¹³Bi bismuth-213

²²⁵Ac actinium-225

⁶⁸Ga gallium-68

⁹⁰Y yttrium-90

^{99m}Tc metastable technetium-99

aa aminoacid(s)

Ac-225 actinium-225

ANOVA Analysis of variance – a statistical test

BCCA British Columbia Cancer Agency

B16 a melanoma cell line

B7 superfamily of peripheral membrane proteins found on activated antigen-presenting cells

Balb/c an albino strain of laboratory mice

Bcl-2 B-cell lymphoma-2 protein

Bcl-xL a transmembrane protein in the mitochondria, encoded by the Bcl2-like 1 gene

BCR biochemical recurrence

BMS Bristol-Myers Squibb

Bq becquerel

C57Bl/6 most widely used laboratory mouse strain

C57Bl/6J inbred strain of C57Bl/6 mice provided by The Jackson Laboratory

CAR-T chimeric antigen receptor-carrying T-cells

CD cluster of differentiation

CD103 integrin, alpha E protein (ITGAE)

CD134 same as OX40, a receptor from the Tumour necrosis factor receptor superfamily

CD16 Fc γ RIII protein

CD19 B-lymphocyte antigen

CD252 same as OX40-ligand

CD3 T-cell receptor subunit on mature lymphocytes

CD32 Fc γ RII

CD357 Tumor necrosis factor receptor superfamily member 18 (TNFRSF18) also known as
activation-inducible TNFR family receptor; a co-stimulatory immune checkpoint
molecule

CD4 a glycoprotein found on the surface of immune cells such as T helper cells, dendritic

cells, monocytes and macrophages

CD44 cell-surface glycoprotein involved in cell–cell interactions, cell adhesion and migration

CD44hiCD62Llo cells with high CD44-expression and low CD62L-expression

CD45 a membrane protein with intracellular tyrosinphosphatase activity

CD62L L-selectin

CD69 human transmembrane C-Type lectin protein encoded by the CD69 gene; an early activation marker

CD8 a transmembrane protein that binds to MHC-I complex

CD86 a co-stimulating receptor, an activator of T-cells

Ci curie

CT computed tomography

CTL cytotoxic lymphocyte

CTLA4 cytotoxic T-lymphocyte-associated Protein 4 (CD152)

Cu-67 copper-67

CUA Canadian Urological Association

d day(s)

DC dendritic cell(s)

DCFPyL see [¹⁸F]DCFPyL

DMEM Dulbecco's modified Eagle's medium

DMSO dimethyl sulphoxide

DOTA 1,4,7,10-Tetraazacyclododecane-1,4,7,10-tetraacetic acid, a commonly used chelator, also known as tetraxetan

DPBS Dulbecco's Phosphate Buffered Saline

EBRT external beam radiotherapy

EdU 5-ethynyl-2'-deoxyuridine

EMA European Medicines Agency

EMD Merck Pharmaceutical company (name used in North America)

et al. and others (Latin *et alii/aliae*)

EUA European Urological Association

FACS fluorescence-activated cell sorting

FBS fetal bovine serum

FcγR subtype of F_c-receptors important for phagocytosis

FcγRII CD32, a unique subtype of FcγR receptors

FDA Food and Drug Administration

FITC fluorescein isothiocyanate

FL1-H height in the FL1 channel

FOX a sequence of 80 to 100 amino acids forming a motif that binds to DNA, present in **FOX proteins** (Forkhead box) proteins – a family of transcription factors

FOXP3 FOX protein family member 3 - a protein regulating development and function of regulatory T-cells, also known as scurfin

g gram

Ga-68 gallium-68

G418 Geneticin, a selection antibiotic

GCPII Glutamate carboxypeptidase II (GCPII), also known as N-acetyl-L-aspartyl-L-glutamate peptidase I (NAALADase I), NAAG peptidase, or prostate-specific membrane antigen (PSMA)

GVAX pancreatic cancer vaccine

h hour(s)

HCC hepatocellular carcinoma

HEPES 4-(2-hydroxyethyl)-1-piperazineethanesulfonic acid

hPSMA human PSMA

I-131 iodine-131

ICD immunogenic cell death

IFN γ interferon gamma

IF immunofluorescence

Ig immunoglobulin

IgG immunoglobulin G

IgG1 subclass of immunoglobulin G

IgG2a isotype of IgG2 subclass

IHC immunohistochemistry

IL-10 interleukin 10

IL-17 interleukin 17

IL-2 interleukin 2

IL2RA interleukin-2 receptor alpha chain, a subunit of IL2 receptor

IMPACT PCR-based pathogen testing

In-111 indium-111

i.p. intraperitoneal(ly)

iTreg induced regulatory T cells

J591 a monoclonal antibody binding the PSMA-extracellular domain; can be radiolabelled

k kilo

keV kiloelectronvolt

l or **L** liter

LLC limited liability company

LNCaP human metastatic prostate cancer cell line (originated from a lymphnode metastasis
cancer of the prostate)

m milli

M molar

M. disease (Latin: *morbus*)

mAb monoclonal antibody

MC-38 a cell line derived from C57BL/6 murine colon adenocarcinoma

MDSC myeloid-derived suppressor cells

MHC-I major histocompatibility complex class I

MHC-II major histocompatibility complex class II

min minute(s)

MIP-1095 ((S)-2-(3-((S)-1-carboxy-5-(3-(4[(131)I]iodophenyl)ureido)pentyl)ureido)pentanedioic acid - a urea-based PSMA-
targeting ligand that can be labelled with iodine-131

mo month(s)

mol mole(s)

MRD minimal residual disease

MRI magnetic resonance imaging

MSD Merck Sharp & Dohme Pharmaceuticals

MSI microsatellite instability

n number

NAAG N-acetyl-L-aspartyl-L-glutamate peptidase I, NAAG peptidase, GCPII, PSMA

NAALADase I N-acetyl-L-aspartyl-L-glutamate peptidase I (NAALADase I), NAAG peptidase, GCPII, PSMA

NF- κ B nuclear factor 'kappa-light-chain-enhancer' of activated B-cells, a protein complex

nTreg natural regulatory T (nTreg) cells

Nu-serumTM a growth medium supplement

NK natural killer cells

NRG NOD.Cg-Rag1^{tm1Mom} Il2rg^{tm1Wjl/SzJ} ("NRG", NOD-Rag1^{null} IL2rg^{null}, NOD rag gamma) mice – an immunodeficient mouse strain

NSCLC non small cell lung cancer

OX40 same as CD134 - member of the TNFR/TNF protein superfamily, expressed on activated CD4 and CD8 T cells

OX40L same as CD252, OX40-ligand, stably expressed on many antigen-presenting cells

OX86 rat IgG1 anti-OX40 antibody

OR odds ratio

OS overall survival

p p-value

P passage number

Pen/strep penicillin/streptomycin culture medium supplement

PFS progress-free survival

p.i. post injection

PBS phosphate buffered saline

PCa prostate cancer

PD-1 programmed cell death 1-receptor

PD-L1 programmed cell death 1 ligand 1-receptor

PET positron emission tomography

Prostvac-VF vector-based PSA-targeting vaccine

PSA prostate-specific antigen

PSMA prostate-specific membrane antigen

PSMA617 (also **PSMA-DKFZ-617**) vipivotide tetraxetan

PSMA I&S a ^{99m}Tc -labelled PSMA-targeting tracer for use in imaging and surgery

PSMA I&T a urea-based PSMA-targeting theranostic ligand

Re-186 rhenium-186

RNA ribonucleic acid

RPM revolutions per minute

RPMI-1640 Roswell Park Memorial Institute 1640 - culture medium

RT radiotherapy

s second(s)

s.c. subcutaneous(ly)

SCC squamous cell carcinoma

SPECT single photon emission computed tomography

SV40 simian virus 40

t_{1/2} half-life

T-cell lymphocyte(s) primed in the thymus gland, expressing T-cell receptor (CD3⁺)

TCR T-cell receptor

TCR- β TCRbeta chain subunit

tet tetracycline

Tet-On tetracycline-controlled transcriptional activation in presence of tetracycline or its derivatives

Tet-Off tetracycline-controlled transcriptional activation in absence of tetracycline or its derivatives

TGF β transforming growth factor beta

TNF α tumour necrosis factor alpha

Th2 type 2 T helper cells

TIL/TILs tumour-infiltrating lymphocytes

TRAMP murine prostate cancer cell line (transgenic adenocarcinoma of mouse prostate)

TRAMP-C2 murine prostate cancer cell line mimicking intermediate metastatic progression

TG treatment group

T_{reg} cells or **T-regs** regulatory T cells

tRL targeted radioligand/targeted radioligand therapy

TSLP thymic stromal lymphopoietin

α alpha particle

β^- beta minus particle (electron)

β^+ beta plus particle (positron)

γ gamma ray

μ micro

$^{\circ}\text{C}$ degree celsius

Chapter 1: Introduction

1.1 Prostate cancer

In Canada, and in most western societies, prostate cancer is the most commonly diagnosed and the third most lethal malignancy in men, with over a million diagnosed cases and 359 000 deaths worldwide in 2018, and an estimate of 22,900 cases, and 4,100 deaths in Canada in 2019 [1-6]. Unambiguously linked to its development are the risk factors: age (most significantly), race/ethnicity, geography, family history and inherited genetic mutations [7,8]. Since 2001, the mortality due to prostate cancer is in decline by a rate of 3.3% per year, due to improved diagnostic testing and treatment options [9]. Despite advances in treatment, relapsed and refractory prostate cancer remain a significant cause of male mortality and morbidity across the globe. The vast majority of cases is detected before progression to a metastatic phenotype happens, since prostate cancer is known to show symptoms in the early stages [10]. Once metastatic disease has developed, the treatment efficiency is known to significantly diminish, and despite recent advancements in pharmacotherapy of prostate cancer, less than a third of patients with the disease spread to extrapelvic organs are expected to live 5 years or longer. Consequently, the clinical demand for more effective treatment in metastatic androgen-insensitive PCa remains high [11-15].

1.1.1. Therapy of prostate cancer

As recommended in the current Canadian Urological Association guidelines, prostate cancer management is multimodal and dependent on clinical features, such as presence of bone metastases, histological findings, tumour's androgen-dependence, or patient's age, among others [6, 16]. Traditionally applied surgical interventions, such as radical prostatectomy, still have a place in prostate cancer management - in localized disease, and in conjunction with patients' individual preferences. Androgen deprivation therapy, on the other hand, is a mainstay of a lifelong metastatic disease management. In addition, second- and third-generation anti-androgens have increased the lifespan of patients with metastatic disease and are currently given priority over taxane chemotherapeutics [6, 12, 16].

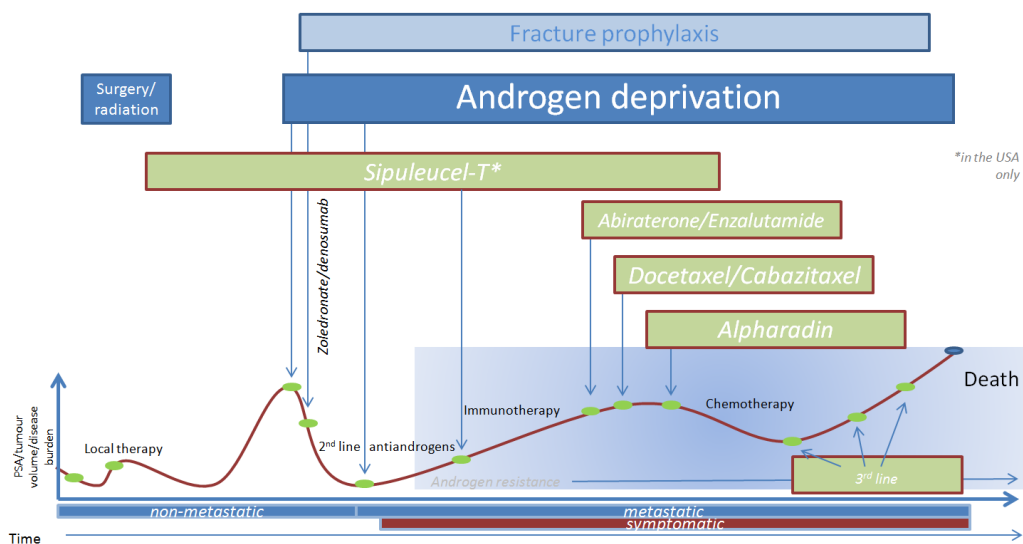


Figure 1.1: Scheme of currently available prostate cancer therapeutic options. Adapted with permission from [6, 16-18].

Typical disease course in PCa patients is marked by a loss of response to different therapy modalities and relapsing tendencies (Figure 1). Progression from metastasis to castration resistance occurs within 10-16 months median time [13]. Therefore, third-line therapy is a focus of dynamic ongoing research, involving hormonal, radio-, immuno- and chemotherapeutic strategies [19-27].

1.1.2. Nuclear medicine in cancer management

Use of radiation represents one of the long-established mainstays of cancer management [28-30]. In nuclear medicine, radionuclides bound to biomolecules are used for imaging and therapy, and a variety of applications is achieved by choosing the appropriate nuclide with (an) appropriate decay mode(s), half-life that matches the biological half-life of the biomolecule, and depth of particle's penetration in tissue. The radiotracer bioconjugate usually incorporates a so-called spacer (synonym: linker) that is responsible for modifications in chemical properties of the entire conjugate molecule. This can be essential for modifying compound's affinity for specific tissues, and in consequence, for an amplified tumour-to-background ratio [31-33]. Radiation originating from the radiometal can be used for diagnostic imaging, namely in single photon emission computed tomography - SPECT – via gamma emission, or positron emission tomography - PET, via positron emission. For imaging of prostate cancer, promising ^{18}F -labelled radiotracers have been investigated in the past several years, allowing for identification of distant

lesions and individualized decision-making regarding therapy. Moreover, alpha, Auger or negatron (beta, β^-) emission can be harnessed for therapy purposes, as a result of tumouricidal DNA double strand breaks. A substantial part (currently around 85%) of applied nuclear medicine is still oriented towards diagnostic procedures, whereby there is a tendency of its decrease in favour of therapeutic application. ^{177}Lu ($t_{1/2} = 6.65$ days), and ^{90}Y ($t_{1/2} = 2.67$ days), that emit beta particles have been studied as promising candidate isotopes for radioimmunotherapy (RIT) of cancer. Their ability to deposit radiation over up to a few millimeters in soft tissue makes them good candidates for therapy of tumours with large necrotic areas and high total volume, ^{177}Lu has additional advantages for targeting micrometastases. ^{177}Lu -labelled radiotracers are gaining popularity due to their dual purpose, as both SPECT-imaging and therapeutic agents [34-49].

1.1.2.1 Theranostics

Research in physics and nuclear medicine in the late 1990s created a novel concept of theranostics, that represented advancement in rational management of cancer patients. In brief, theranostic approach in nuclear medicine implies that the same biological target is used for binding imaging radiopharmaceuticals and as a target for cytotoxic radiation [28, 29, 39, 43, 47]. This can either be achieved by exchanging the imaging nuclide for a therapeutic radionuclide, or by using specific nuclides whose decay modes allow for both purposes. Use of theranostics facilitates diagnosis and tracking of the disease progress in conjunction with therapeutic anti-tumour performance. In other words, individual patient's disease state can be staged in order to

guide optimal personalized therapy options. Screening for the disease and oncotherapeutic efforts can, in this manner, be achieved with increased cost-effectiveness, since treatment efficacy can be monitored using tracers that are similar, or identical, to the therapeutic agent. By exchanging the positron- or gamma-emitting radiometal from a bioconjugate with a therapeutic radiometal (alpha- or beta-minus-emitters), cancer cells that express the targeted antigen are visually identified, and moreover, the targeted therapy response pattern can be demonstrated. In consequence, managing individual cases becomes personalized, leading to better selection of case-to-case therapy regimens and patients' overall improvement, while avoiding overtreatment of false-positive cases [27, 29, 39, 43, 47, 50-52, 62-65]. Lutetium-177 has been widely utilized as a radioisotope of choice for targeted radionuclide therapy (tRL) (Table 1), a type of cancer treatment wherein radioisotope-labelled compounds bind to antigens expressed in malignant tissue, causing irreversible damage to the cancerous cells. Furthermore, the simultaneous emission of imageable gamma photons [208 keV (11%) and 113 keV (6.4%)] along with particulate β^- emission [$\beta(\text{max}) = 497 \text{ keV}$] makes lutetium-177 a theranostically suitable radionuclide [65-68].

Radionuclide	Physical $t_{1/2}$ (days)	Radiation type and energy in (MeV)	Particle range (mm)
^{131}I	8	Beta (0.6), gamma (0.364)	2
^{90}Y	2.67	Beta (2.28)	12
^{67}Cu	2.58	Beta (0.54), gamma (0.185)	1.8
^{188}Re	3.77	Beta (1.08), gamma (0.131)	5
^{177}Lu	6.7	Beta (0.497), gamma (0.208)	1.5

Table 1.1. Common beta-emitters in use in nuclear medicine. The ideal radionuclide has a longer half-life (several days), short penetration in tissue, and deposits high energy. Compared to other emitters, lutetium-177 possesses most favourable traits. Adapted from [60].

1.2. PSMA

Prostate-specific membrane antigen (PSMA, also Folate Hydrolase 1 - FOLH1; glutamate carboxypeptidase II – GCPII; Figure 1) is a 750 aa type II transmembrane glycoprotein with enzymatic activity that is expressed on the cell surface of healthy prostate, and overexpressed (100 - 1000-fold) in aggressive forms of localized prostate cancer. Moreover, it is upregulated in poorly differentiated metastatic and hormone-refractory carcinomas. Its levels increase with higher tissue dedifferentiation, making PSMA a highly attractive target in nuclear medicine. The function of this enzyme in prostate cancer and healthy prostate is still unclear, although its respective folate- and NAAG-hydrolyzing activities in small intestine and nervous system have been clearly delineated thus far [69-79].

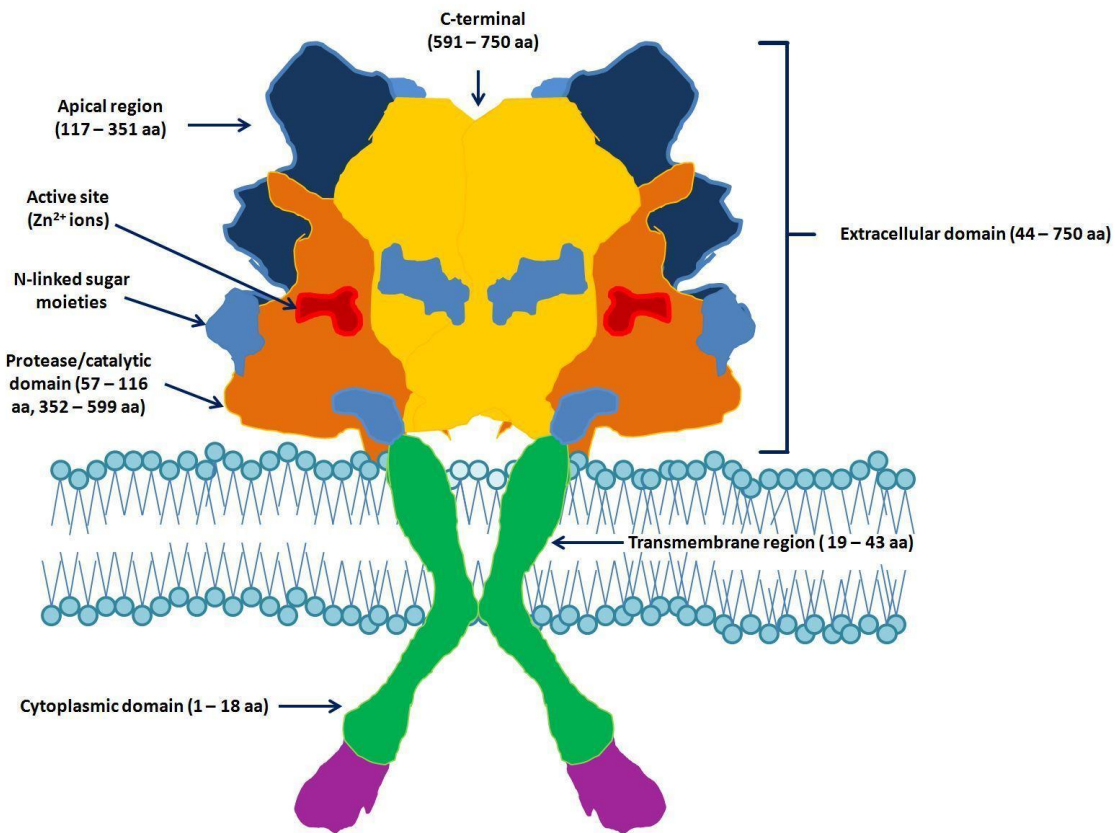


Figure 1.2. PSMA homodimer structure scheme. aa: aminoacid(s); C: carbon; N: nitrogen; Zn: zinc. Adapted with permission from [74] and [75].

1.2.1 PSMA-targeting radiopharmaceuticals

Small peptide-like molecules that bind to its active extracellular domain have emerged as state-of-the-art prostate cancer imaging radiotracers [101-103], capable of imaging PCa with

remarkable tumor-to-background ratios [34, 35, 40, 42, 43]. Currently, most widely used PSMA-targeting PET tracer both in PET/CT and in PET/MRI, is ^{68}Ga -labelled PSMA-11 (or HBED-PSMA) [81-85], an example of PSMA-binding compounds with Glu-urea-Lys binding motif. Compared to conventional PCa imaging, PSMA PET has demonstrated superior specificity and sensitivity, with the ability to identify subcentimeter and distant lesions, in prostate, bone, lymph nodes and soft tissue. PSMA PET has gained clinical value in high-risk primary lesion staging and disease localization in cases of biochemical recurrence. Low-volume lesions can, compared to conventional techniques, be easily identified at very low PSA levels due to the high sensitivity of PSMA PET. Use of PSMA PET for therapy monitoring in mCRPC radionuclide therapy is a subject of ongoing dynamic research. Recent meta-analyses showed extraordinary diagnostic performance for primary and secondary staging (re-staging following BCR) due to its ability to detect lesions even at very low serum PSA levels [80-89]. Therefore, for example, the most recent EAU guidelines recommend PET/CT using PSMA-targeting radiotracers at low serum PSA levels (≥ 0.2 ng/ml) [87].

1.2.1.1 Lutetium-177-labelled theranostic agents in cancer management

The radioactive emission of beta particles by radionuclides such as ^{177}Lu can exert their effect on the tissue over several cell diameters [65, 66]. In case of tumour cells, this toxic effect ideally damages tumour DNA and, by causing stable mutations, cancerous cells' progression is thwarted. Due to the shorter range of β emissions, ^{177}Lu is preferred to ^{90}Y since renal or marrow

toxicity is an important factor to consider in mCRPC [45, 90-92]. This tRL has significant advantages over local RT as it systemically targets disseminated cancer cells. To date, [¹⁷⁷Lu]-PSMA617, applied for both dosimetry and therapy purposes in prostate cancer, has shown highest efficiency in reducing pain and biochemical disease markers, and prolonging survival in early non-randomized clinical trials (Table 1.2).

Ligand	Radionuclide	Status according to clinicaltrials.gov
MIP-1095	¹³¹ I	Compassionate use
PSMA I&T	¹⁷⁷ Lu (⁶⁸ Ga, ¹¹¹ In)	Compassionate use
J591	¹⁷⁷ Lu	Phase I
PSMA617	¹⁷⁷ Lu (also ⁶⁸ Ga and ²²⁵ Ac)	Phase I/Phase II/Phase III
PSMA I&S	^{99m} Tc	Not yet recruiting

Table 1.2. PSMA ligands used in therapy/palliation of PCa. PSMA: prostate-specific membrane antigen; Ac: actinium; Ga: gallium; I: iodine, In: indium; Lu: lutetium; Tc: technetium.

1.2.1.1.1 [¹⁷⁷Lu]Lu-PSMA617

Due to significantly lower PSMA-expression levels in healthy versus diseased tissue [74, 75], targeting this membrane glycoprotein has the potential to meet the clinical requirements for high-dose/low-toxicity endoradiotherapy of PCa. Once bound to the glycoprotein's extracellular active centre, the PSMA ligands are internalized into the cytosol, making them a reliable source of endoradiotherapeutic activity and a tool in localizing disease foci [93-96]. In recent years, lutetium-177-labelled PSMA-targeting radioligands have rapidly gained worldwide attention for the treatment of metastatic castration-resistant prostate cancer (mCRPC). In 2015, another Glu-urea-Lys-based, PSMA-binding, DOTA-conjugated biomolecule - [¹⁷⁷Lu]Lu-PSMA617 (or [¹⁷⁷Lu]Lu-DKFZ-PSMA617) - was synthesized in Heidelberg, Germany. It emerged as a theranostic compound with promising results in up to 70% of non-responders to first- and second-line prostate cancer treatments [97, 98] and its efficacy has been confirmed in a series of retrospective studies [103, 104]. A non-randomized trial showed a sustained PSA response (with no significant toxicities) in ~60% of heavily pre-treated patients (n=30) receiving [¹⁷⁷Lu]Lu-PSMA617 [103]. As long as results from randomized prospective (phase III) trials are still being anticipated (release planned in 2021), radioligand-therapy targeting PSMA will remain a third-line option for heavily pretreated, symptomatic patients. Nonetheless, data published to date have indicated its safety and effectiveness, with rarely occurring higher-grade haematological toxicities (3-11%), and reported absolute safety regarding severe non-haematological toxicities [103-107]. Available literature reports encouraging data on progression-free survival (PFS = 3.6-13.7 months), overall survival rates (OS = 7.5-29.8 months) and re-administration safety [106, 107, 109-112]. Given the fact that most treated patients had undergone various cycles of different

autoimmunity [133-136]. Interfering with immune checkpoints in the PD-1, PD-L1, PD-L2, and CTLA-4 axes and developing resistance to immune pro-apoptotic signals are further mechanisms of tumour immune escape. Targeting these pathways is a mainstay of cancer immunotherapy and these approaches have already been used in clinical trials for other malignant neoplasms [137-139]. Immunotherapies fall into four major categories: checkpoint inhibitors, cytokines, therapeutic cancer vaccines and genetically engineered CAR-T cells. Positive clinical outcomes were observed in colon, renal, and lung cancer, and in metastatic melanoma [137-140]. Immune checkpoint blockade with antagonistic monoclonal antibodies (mAbs) targeting proteins of the B7 immunoglobulin superfamily (CTLA-4, PD-1, and PD-L1) generate long lasting anti-tumour immune responses translating into clinical benefit across many cancer types and reaffirming the role of immune system in the fight against cancer [141-142]. In prostate cancer, there have been numerous clinical trials on immune checkpoint therapy and therapeutic vaccines [126, 128, 131, 143].

1.3.1 Immune checkpoint blocking therapeutics

Cancer, and chronic infections alike, is facilitated by diverse immune subversion mechanisms, such as expressing regulatory phenotype of T-cells, secretion of immunomodulatory cytokines, such as IL-17, and by expressing so-called immune checkpoint surface proteins, that suppress immune response upon binding their ligands [132]. Imbalances in these mechanisms underlie a variety of autoimmune diseases and cancer of different tissue origin, including prostate cancer. Immune checkpoint blockade with antagonistic monoclonal antibodies (mAbs) targeting

B7 immunoglobulin superfamily molecules (CTLA-4, PD-1, and PD-L1) generate long lasting anti-tumour immune responses translating into clinical benefit across many cancer types. However, many patients are primarily resistant to immune checkpoint blockade - based monotherapy and many others will eventually relapse. In addition, prostate cancer immunotherapy did not manifest the same levels of success it did in e.g. melanoma, NSCLC or urothelial bladder cancer, i.e. those cancer sites that elicit a vivid immune response due to high mutational load - so called “immunologically hot” cancer. The mutational load levels of prostate cancer are considered intermediate [151, 152] relative to other cancer sites, so it is without surprise that clinical and pre-clinical studies so far have shown mixed success. Recent findings suggest that immune response in PCa is present, however requiring additional boost in order to serve as a substrate for immunotherapy.

Therefore, new immunostimulatory targets are needed to overcome primary and secondary resistance to immunotherapy in PCa [153-155]. Besides the B7 co-inhibitory receptors, the tumour necrosis factor receptor superfamily contains many other immune checkpoints, which could become the next generation immunomodulators. Among them stands OX40 (CD134), a co-stimulatory molecule that can be expressed by activated immune cells. Several anti-OX40 agonistic monoclonal antibodies are currently tested in early phase cancer clinical trials [160, 161]. Accumulating preclinical evidence supports their clinical development. However, conflicting results and controversies between *in vitro* and *in vivo* data point to the need for comprehensive ancillary studies to be performed in upcoming clinical trials to better understand the mechanism of action of anti-OX40 mAbs-based therapy [160, 162]. Antibodies targeting checkpoint inhibitors or co-stimulatory receptors on T cells have shown significant antitumor efficacy in preclinical and clinical studies.

Drug	Commercial name	Manufacturer	Target	First approval	Indication(s)
Pembrolizumab	Keytruda	MSD	PD-1	September 2015	Melanoma, NSCLC, classic M. Hodgkin, renal-cell carcinoma, head-and-neck SCC, urothelial carcinoma, solid tumours with high MSI or MRD levels
Atezolizumab	Tecentriq	Roche	PD-L1	May 2016	urothelial carcinoma
Avelumab	Bevancio	EMD/Pfizer	PD-L1	March 2017	Merkel-cell carcinoma, urothelial carcinoma
Durvalumab	Imfinzi	AstraZeneca	PD-L1	May 2017	NSCLC, urothelial carcinoma

Table 1.3. Immune checkpoint inhibiting agents approved for cancer therapy. MRD - minimal residual disease; MSD - Merck Sharp & Dohme Pharmaceuticals, MSI: microsatellite instability PD-L1: programmed death –ligand 1, PD-1: programmed death 1, NSCLC: non-small cell lung cancer.

Authors (year published)	Number of patients	Diagnosis	Treatment	Outcome
Slovin et al. (2013)	50	mCRPC	ipilimumab + RT	complete response in one patient, stable disease in 6, good biochemical response in 8 patients.
Borradori et al. (2016)	5	Progressive cutaneous SCC and basosquamous carcinoma	RT + adjuvant or neoadjuvant nivolumab/pembrolizumab	partial (n=2) and stable (n=3) response
Kwon et al. (2014)	799	mCRPC	ipilimumab versus placebo after RT	median OS=11.2 mo, OS at 1 year 46.8% PFS at 6 mo=30.7%
Golden et al. (2013)	1	metastatic NSCLC	concurrent ipilimumab and RT	complete response due to abscopal effect one year after treatment

Table 1.4. Studies reporting use of immune checkpoint inhibitors in non-melanoma patients [163-166]. mCRPC: metastatic castration-resistant prostate cancer; NSCLC: non-small cell lung cancer; OS: overall survival; PFS: progress-free survival; RT: radiotherapy; SCC: squamous cell carcinoma.

1.3.2 PCa immunotherapy

The immune response in prostate cancer patient is often suppressed and the outcomes of prostate cancer immunotherapy trials have been modest (Table 1.4) [148, 151-158]. Early results from checkpoint blockade trials have had mixed success in mCRPC. In particular, early anti-PD-L1 trials have failed to elicit responses predicted based on positive data from other tumours, although one trial showed response in 3 out of 10 patients treated with anti-PD-L1 therapy, with rapidly decreased PSA values [151]. The use of peptide-based immunotherapeutic approaches, DNA/RNA strategies and cell-based vaccines in prostate cancer has been a subject of pre-clinical and clinical research, again with mixed success. Prostavac, a PSA-targeted poxvirus-based vaccine failed to show satisfactory performance in phase III clinical studies. On the other hand, Sipuleucel-T, a dendritic cell-based active immunization drug, is currently approved by the Food and Drug Administration (FDA); however, the treatment is currently cost-prohibitive [154-156].

Drug	Number of patients	Phase	Key result	Author (year)
Sipuleucel-T	127	III	Improved OS compared to placebo (25.9 vs 21.4 months)	Small et al. (2007)
	98	III	improved OS compared to placebo (19 vs 15.7 months)	Higano et al. (2009)
	512	III	improved OS compared to placebo (25.8 vs 21.7 months)	Kantoff et al. (2010)
Ipilimumab	799	III	no difference in OS compared to placebo; trend of improved PFS rate by ipilimumab at 6 mo (30.7% vs 18.1%)	Kwon et al. (2014)

(continues on next page)

Drug	Number of patients	Phase	Key result	Author (year)
Prostvac-VF	125	II	improved OS compared to control vector placebo (25.1 vs 16.6 months)	Kantoff et al. (2010)
	32	II	improved OS compared to historical controls (26.6 vs 17.4 months)	Gulley et al. (2010)
	626	III	terminated early due to futility analysis results (<30% likelihood of meeting improved OS - primary endpoint)	

Table 1.5. Relevant clinical trials on prostate cancer immunotherapy [mo: months; OS: overall survival; PFS: progress-free survival; Prostvac-VF - vector-based PSA-targeting vaccine; GVAX – a pancreatic cancer vaccine. [145, 149, 156, 157, 163]

1.3.3 OX-40

OX-40 is a 50 kDa type I membrane glycoprotein and a member of the TNF receptor superfamily, also known as CD134 [158-160]. While it is transiently expressed on activated CD4 and CD8 T cells upon antigen stimulation and T_CR-signaling, resting naïve T cells and resting memory T cells are OX40-negative [158-181]. Contrary to historic beliefs, it has further been identified in activated T_{reg} cells, neutrophils, NK and NKT cells [159, 160, 168, 173-181, 234, 235].

OX40-signaling regulates NF- κ B-mediated differentiation, plays a major role in primary clonal expansion and memory development of CD4⁺ lymphocytes and initiates activation of CD8⁺ cells and cytokine release by upregulating the antiapoptotic proteins Bcl-xL and Bcl-2 [160]. Altogether, the antitumour effect is potentiated by its triggering. OX40's ligand – CD252; OX40L – is expressed on activated dendritic cells, B-cells and macrophages – also known as professional antigen-presenting cells – following stimulation with CD40, lipopolysaccharide or TSLP, and peaks 48-72 h after *in vitro* and *in vivo* stimulation [158-168]. Its expression on CD3⁺CD4⁺ accessory cells promotes T_H2 cell survival through interacting with T_H2-own OX40 [159, 162, 171, 179]. In experimental tolerogenic *in vivo* systems, triggering OX40 has been shown to prevent tolerance induction and to reverse lymphocyte hyporesponsiveness [167]. Furthermore, OX40 is largely involved in the pathogenesis of autoimmune disease; blocking the OX40 – OX40L axis ameliorates autoimmune symptoms [157-159, 167-169, 172, 173, 175, 180].

While inhibition of OX40 signaling is found to be beneficial to treat autoimmunity, its triggering improves immune response to cancer. Indeed, systemic OX40L – Ig fusion protein administration or OX86 agonist mAb induces the rejection of various types of subcutaneous

tumours in mice. OX40 triggering leads to functional inactivation of immune-regulatory populations, such as regulatory T-cells whose activity is essential in developing T-cell tolerance and the resulting resistance to cancer immunotherapy, and vice versa, OX40-depletion induces peripheral precursors to acquire regulatory phenotype [159-175, 177-179]. This is achieved in a variety of mechanisms: by modulating the homeostasis of nT_{reg} cells and their effector function, as well as by generating iT_{reg} (inducible/adaptive regulatory T-) cells [160]. Further, it leads to costimulatory signaling to antigen-reacting naïve T-cells to prolong proliferation, and finally, it augments secretion of several cytokines [159-180]. This is corroborated in experiments with OX-40 knockout mice that generated fewer primary effector CD4 T cells than wildtype mice, following immunization [227-229]. Furthermore, *in vivo* treatment with an agonist antibody to OX-40 has been shown to strongly enhance the generation of antigen-specific cytotoxic effector T cells, by providing so-called “fitness-signals”, and concurrently prevent the induction of T cell tolerance. Interestingly, experiments in tumor-bearing Rag1-knockout (KO) mice, showed that both regulatory and effector T cells must be triggered via OX40 for the tumor to be rejected. Upon intratumoral OX40 triggering, increased numbers of infiltrating dendritic cells (DCs) migrate to draining lymph nodes and generate a new wave of tumor-specific cytotoxic T lymphocytes, as detected by CD44 and tetramer staining of node CD8(+) T lymphocytes, allowing DCs to induce an adaptive immune response [160-167, 173-178, 180, 181, 230-232].

DC-derived OX40L expression critically enhances and maintains helper-2-cells responses, simultaneously promoting IFN γ -producing priming of helper-1-cells. Another established effect of OX40 is that, by increasing the number of effector T-cells and the surviving effector T-cells later acquiring memory phenotype, OX40 indirectly expands the pool of memory T-cells, which can again play a role in antitumour immunity [159, 160, 162-169, 173, 175, 177, 179].

In fact, experiments with OX40L-knockout mice showed significantly lower CD44^{hi}CD62L^{lo} effector memory population of polyclonal CD4⁺ T-cells, compared to wild-type mice [234, 235].

Additional effect was identified by Takeda et al., who found significantly lower number of CD25⁺ CD4⁺ nTreg cells in OX40-knockout mice than in their wild-type littermates. In contrast, transgenic strains with forced constitutive expression of OX40L exhibit increased nT_{reg} numbers in both spleen and thymus [236]. An essential role OX40 has for the functional T-cell-mediated antitumour efficiency is illustrated in findings by Rogers et al. and Song et al., namely that OX40-deficient CD4⁺ T-cells are unable to maintain high levels of antiapoptotic molecules, such as Bcl-xL, Bcl-2 and survivin, leading to decreased cellular life span.

Combination of anti-OX40 therapy with different anti-cancer agents is very promising and it has been proposed as a novel adjuvant therapeutic. Piconese et al. demonstrated that generation of iT_{reg} is hampered by intratumoural injection of an agonistic anti-OX40 mAb [167]. Hirschhorn-Cymerman et al., on the other hand, reported effective tumour immunity against poorly immunogenic B16 melanoma, as a result of cyclophosphamide treatment along with an OX40 agonist antibody [172]. The same group postulated the possibility of OX40-mAb-mediated induction of T_{reg} population expansion in the periphery and simultaneous apoptosis of intratumoural T_{reg} cells.

It has been speculated that IFN γ -rich environment as a result of OX40-signaling causes poor induction in iT_{reg} populations [171]. Additionally, stimulating signals to OX40 inhibit the TGF β -mediated differentiation of iT_{reg} cells, mediated by effector cytokines, especially IL-4 and IFN γ derived from OX40-stimulated T_{eff} cells from the immediate environment. Anti-OX40 agonists were found to especially promote immunologically mediated abscopal effects, extending

the benefits of radiation to systemic disease control, as a rationale for overcoming anti-PD1-resistant poorly immunogenic tumours.

This combination was effective in inhibiting local and systemic antitumour growth, limiting metastatic activity and improved survival rates in a PD1-inhibitor-resistant syngeneic mouse model of lung adenocarcinoma [239].

1.3.3.1 OX86

Agonistic antibodies targeting co-stimulatory tumor necrosis factor superfamily receptors (TNFRs) expressed by T cells, such as GITR (CD357) or OX40 (CD134), have been shown to enhance the proliferation and activation of isolated T cells [176]. Moreover, in preclinical tumour treatment studies, these agonistic antibodies have shown potent tumouricidal activity. The agonist anti-OX40 monoclonal antibody - OX86 - reacts with mouse species-specific OX-40 [158, 167, 172-180]. It has been shown to delay tumor growth *in vivo* [167, 172, 173] and moreover, intratumour OX86 injection was shown to induce tumor rejection in 80% of mice [172]. OX86 administration results in the depletion of intratumoural regulatory T cells in an activating FcγR-dependent manner, which correlates with tumour regression [12].

The agonistic anti-OX40 antibody, clone OX86 (rat IgG1), has been shown to mediate regressions in renal cancer, colon cancer, melanoma and B cell lymphoma models in syngeneic Balb/c mice [173, 241, 242].

Published data support a mechanism whereby antibodies targeting antigens highly expressed by intratumoural T cells can mediate reduction in tumour volume. Systemic OX86 administration resulted in a significant reduction in the density of tumour-infiltrating T_{reg} cells

and CD4⁺Foxp3⁺ T-cells, leading to an increase in the ratio of intratumoural CD8⁺ T-cells to regulatory T-cells. Impact of OX86 treatment on the total CD45⁺ tumour-associated frequency fails to appear, signifying selectivity following OX86 administration [158, 167, 172-181].

In conclusion, a huge body of evidence has been cumulating that speaks in favour of agonistic OX40-targeting as a novel immunotherapeutic for cancer. Among antibodies targeting OX40, OX86 has shown high performance and is the most extensively studied.

1.4 Abscopal effects of radiation

As previously mentioned, use of radiation is a pillar of treatment of various solid cancers, and improved understanding of its mechanisms has led to discovery of its systemic (“abscopal” – *ab + scopus* – Latin for “away from the target”) sensitizing effects. Interest in abscopal effects has increased particularly in the previous decade, since the use of checkpoint inhibitors in cancer therapy created possibilities for more potent combination therapy strategies. Use of radiation in combination with immunotherapy is indeed the subject of intense research interest. The rationale for such combinations is based on a series of factors, one of them being RT-induced increase in tumour-antigens, released from the irradiated mass, processed and presented by dendritic cells that signal CD4⁺ and CD8⁺ T-cells to activate and migrate to the tumour site. Additional mechanism of particular interest is the evasion of regulatory immune responses, such as suppression by MDSCs and T_{reg} cells, while CD103⁺ cells are upregulated following radiation. Of note is that radiation can act as an epigenetic modulator, allowing the OX40 and OX40L promoters to be methylated and acetylated. Another example of expanded antitumour immunity

is increased costimulatory signaling as a result of radiation-induced ligand expression, and this mechanism was precisely found to be the case with OX40L (CD252). Another established underlying mechanism of abscopal effect is radiation-induced MHC-I expression driven by interferon production, leading to increase in CD8⁺ T-cell infiltration, priming and activation. By increasing CD103⁺ subset of DCs and the OX40L⁺ CD4⁺ T-cells, radiation doses bridge innate and adaptive immune system, which can provide a vivid immune antitumour response [180-210].

1.5 Tumour model

Rodents are used as models in medical experiments due to their biological and genetic resemblance with humans. Many symptoms of human disease, including cancer, can be replicated in mice and rats. For the purpose of this type of study, various prostate cancer cell lines can be used in order to mimic the actual human disease state. In order to assess immune response to the therapy and support the OX86 in its anti tumour effects, an immunocompetent mouse model was selected. C57Bl/6 mice have been widely used for nearly a century and represent the most commonly used laboratory mouse strain altogether. Since mice lack PSMA-expression, a human cancer-derived cell line, such as LNCaP, can ignite robust anti-tumour immunity, resulting in rejection of tumour. TRAMP-C2 and other murine tumour cell lines do not express human PSMA; however, TRAMP-C2 was shown to be metastatic and androgen-insensitive in subcutaneous tumour models. Therefore, a transduced TRAMP-C2 model, expressing human PSMA upon induction with tetracycline-class antibiotic doxycycline, is at the same time non-immunogenic and target-expressing. Once transduced with a bacterial plasmid that incorporates a

PSMA-coding sequence, these cells become responsive to tet-induction (Tet-On system) in presence of doxycycline antibiotic. For the pre-clinical assessment of our combined therapeutic strategy, this tumour model is expected to accumulate [¹⁷⁷Lu]-PSMA617 and offer a substrate for anti-tumour immunity. The effects on TRAMP-C2 tumour growth will be compared to that observed in PSMA expressing human LNCaP mice implanted into immunocompromised mice. To assess possibility of *in vivo* TRAMP-C2-clones' viability, a strain of immunodeficient mice known as NRG was selected, due to reported use in nuclear medicine imaging and endoradiotherapy studies. Since a fully developed and functional immune system is required to examine the therapeutic effects of anti-OX40 agonistic antibody, a clone that shows PSMA-expression upon induction will later be propagated and inoculated into C57Bl/6J mice. If necessary, an alternative would be short-term metastatic experiments by TRAMP-C2 cells' intravenous injection [212-219].

1.6 Thesis Aims

1.6.1 Rationale

What is the potential of [¹⁷⁷Lu]-PSMA617 and anti-OX40 agonist, as a combination treatment, as opposed to either treatment alone? As can be read throughout the Introduction Chapter, while local radiotherapy can induce potent antineoplastic immune responses [197, 210, 212, 243] and improve effects of checkpoint inhibitors, there is evidence that prostate cancer is

only moderately immunogenic. However, a stronger, vivid immune response to PCa can be augmented by an immunotherapeutic, such as anti-OX40 mAb [244]. [¹⁷⁷Lu]-PSMA617 tRL targets both prostate and bone lesions, maximizing immunogenic cell death (ICD) and leading to increased spread of substrate for immunotherapy. A substantial body of evidence reaffirms the phenomena of radiation-induced antitumour immunity. To name some examples, vaccination plus an yttrium-90-labelled antibody showed more potent effects than either approach alone, in pre-clinical models [245]. [¹⁵³Sm]Sm-EDTMP increased LNCaP-susceptibility to cytotoxic T lymphocytes (CTLs). ¹⁷⁷Lu-labelled peptide administration resulted in increased NK and CD86+ antigen presenting cell infiltration [246]. Finally, pre-treating mice with ²¹³Bi prior to MC-38 implantation enhanced CTL and dendritic cell activation, which correlated with tumour size reduction and improved survival [247]. Since tRL is administered systemically, we anticipated increased effectiveness compared to external beam radiation therapy (EBRT) aimed at a single tumour volume. The ability to reach cell clusters in multiple organs may create a potent immunostimulatory environment and elicit a polyclonal T-cell response. Favourable response to [¹⁷⁷Lu]-PSMA617 has not been fully explained by the delivered radiation; hence the immune system can potentially be deemed responsible. Combination treatments involving [¹⁷⁷Lu]-PSMA617 have been evaluated by several groups, none of which, however, focused precisely on combinations with checkpoint inhibitors. As a further matter, emerging research confirmed immunostimulating properties of RT for some patients, and benefits of radiation in mCRPC are well-known. For the most part, the underlying mechanisms have been elucidated, including the abscopal effect. Most recently, the results of early trials in PCa immunotherapy show promise, especially if combination treatments were assessed [154, 155, 221, 222, 248].

In brief, relying on the need for novel therapy regimens of late-stage metastatic PCa, the described therapeutic success of [Lu]-PSMA617 together with its additional value in dosimetry, and the elucidated mechanisms of the abscopal effect, we will demonstrate the proposed dual treatment's potential in fighting prostate cancer.

1.6.2 Hypothesis

We hypothesize that the combination of [¹⁷⁷Lu]-PSMA617 and OX86 in a syngeneic mouse model will result in a more potent tumour burden reduction than either treatment alone, as could potentially be seen from decrease in tumour volume and difference in overall survival rates between treatment groups.

1.6.3 Specific aims

To test the hypothesis, we will use a transgenic, tet-inducible hPSMA-expressing mouse tumour cell-line (TRAMP-C2), generated by our collaborators at the Deeley Research Centre in Victoria, BC. Once a clone with high PSMA-expression is identified per flow cytometry studies, it will be expanded and inoculated into NRG mice for proof of protein-expression induction in ¹⁸F-labelled PET radiotracer studies (**Aim 1**). Upon successful induction, immunocompetent C57Bl/6J mice will be inoculated with the cell clones derived from the subcutaneous tumours, excised from NRG mice. Mice will be randomly assigned to 6 treatment groups [combined interventions (tRL + mAb), single interventions (tRL alone, mAb alone) and control (IgG2a isotype; IgG2a isotype + tRL; PBS)], monitored for weight, tumour size and signs of illness over

time (**Aim 2**). Therapeutic effects of combined therapy, compared to monotherapy and controls, will be assessed by the analysis of tumour growth inhibition in each treatment group (**Aim 2, sub-aim a**), while an ex vivo multiparametric high-resolution analysis of radiation distribution and the resulting pathohistological patterns of proliferation, oxygenation and tissue viability between treatment groups will further elucidate the mechanisms by which locally deposited radiation and OX86 attain synergistic effects (**Aim 2, sub-aim b**). For this purpose, we will perform beta-imaging and immunofluorescence studies in tumour and spleen tissues and compare the findings between different treatment groups and at different timepoints, delineating patterns of distribution of cytotoxic β -emissions, associated cellular DNA damage, degree of proliferation and localization of tumor infiltrating lymphocytes (TILs). The co-registration with perfusion and hypoxia markers will determine the *in vivo* distribution profile of [^{177}Lu]-PSMA617 and ICD relative to administered dose and presence of OX86. This can help guide dosage and sequences in repeated experiments and further projects. The hypoxic prostate tumor environment could possibly cause the lack of synergy of tRL and checkpoint blockade, which would reduce the effectiveness of radiation and/or suppress TIL responses. Using co-registration methods in Aim 2b, we will determine the role of hypoxia on TIL responses and potentially reverse hypoxia-mediated immune suppression by Avastin. 3 mice will be sacrificed prior to the treatment and a tumour core biopsy collected and spleen harvested for baseline flow and IF analyses.

Chapter 2: Materials and Methods

2.1 Reagents and Instrumentation

All chemicals and solvents were obtained from commercial sources and used without further purification. ^{18}F -fluoride was produced by ^{18}O (p,n) ^{18}F reaction in a cyclotron TR19, purchased from Advanced Cyclotron Systems Inc. [^{177}Lu]-chloride was purchased from Isotopen Technologien München AG (Garching, Germany) and delivered to the BCCA Cyclotron Facility. The activity was measured using a Capintec CRC®-25R/W dose calibrator.

2.2 Peptide synthesis

PSMA-617 was synthesized using a solid phase approach on an Aapptec (Louisville, KY) Endeavor 90 peptide synthesizer. Details of synthesis procedure are described later in Section 3.2.1.

2.3 Synthesis of [^{177}Lu]-PSMA-617

^{177}Lu labeling was performed with 5 equivalents LuCl_3 (5 equivalents) in NaOAc buffer (0.1 M, 500 μL , pH 4.2) at 90 °C for 15 min, and purified by HPLC using the semi-preparative column. The HPLC conditions were 25% acetonitrile in water with 0.1% TFA at a flow rate of 4.5 mL/min.

2.4 [¹⁸F]DCFPyL radiolabeling

[¹⁸F]DCFPyL radiolabeling was performed according to previously published procedures [249].

Radiochemical purity was confirmed by HPLC analysis using an analytical RP-C18 column with gradients of acetonitrile and water (both containing 0.1% TFA). Molar activity values were measured based on standard curve analysis. [248, 249].

Further specifications concerning Materials and Methods in this Thesis are listed in the following chapters.

2.5 Statistical tests

In order to compare tumour growth inhibiting potency in each treatment arm, and after excluding all tumours that were harvested for different purposes than reaching humane endpoint (e.g. biodistribution, FACS studies, autoradiography studies, immunostaining; see Chapter 5), an unpaired one-tailed t-test with unequal variance will be performed, comparing the incremental change in tumour volume between combination treatment and the monotherapies, as measured between the timepoint of treatment and a timepoint past day 13 (tumour infiltrating lymphocytes levels back to normal according to literature [185]). The second timepoint will be selected so that the increments will be comparable between different tumours and treatment groups. In case the results support the necessity to compare more than two treatment groups, an ANOVA test will be performed.

Chapter 3: Cell line validation

3.1 Introduction

The first set of experiments in this thesis was focused on the purpose of Aim 1 – establishing a cell line that can be compatible with our therapy study design. Ideally, such system should not trigger immune response, and it requires high degrees of biocompatibility, target-to-background contrast and sensitivity [258]. Our aim was to confirm successful induction of PSMA-expression *in vitro* in order to later test its inducibility in murine models, beginning with the immunocompromised phenotype.

3.1.1 Tetracycline-inducible protein expression

Tet-On and Tet-Off systems have been widely used in biomedical research as an important tool allowing for controlled gene expression in eukaryotic cells and organisms [259-262]. Based on a modified and improved bacterial operon, those systems become effective upon binding of a tetracycline class antibiotic [263], either by switching off gene expression in a so-called Tet-Off system, or by inducing gene expression in a (more favourable) Tet-On system, wherein a different variant of the transcription activator is employed [264, 265]. This non-invasive approach has found wide application in gene therapy and signal cascade-activation monitoring, as well as in cell motility tracking studies [266].

3.1.2 PSMA-expression in prostate cancer models

As opposed to several human-derived cell-lines, such as LNCaP, TRAMP-C2 (transgenic adenocarcinoma of the mouse prostate - cell line number 2), a transgenic murine (C57BL/6-derived) cell line expressing the SV40 large T-antigen, does not constitutively express human PSMA (FOLH1), however their advantage is, for this same reason, the absence of immunogenicity in animal models [76, 267]. Nevertheless, if successfully transfected with a plasmid allowing for inducible PSMA-expression, it can at the same time be utilized as a PSMA-expressing model, while maintaining its viability in an immunocompetent environment. This strategy was applied in generating a novel line at the Deeley Research Centre in Victoria, BC, four different clones of which were used in this thesis.

3.2 Materials and Methods

3.2.1 Peptide synthesis

PSMA-617 was synthesized using a solid phase approach on an Aapptec (Louisville, KY) Endeavor 90 peptide synthesizer, beginning with Fmoc-Lys (ivDde)-Wang resin. The isocyanate of the t-butyl-protected glutamyl moiety was first coupled, according to [247], and the ivDde-protecting group subsequently removed with 2% hydrazine in N,N-dimethylformamide (DMF). Next, coupling of Fmoc-2-Nal-OH, Fmoc-tranexamic acid and DOTA-tris(t-bu)ester, followed by trifluoroacetic acid (TFA) cleavage provided the crude product of PSMA-617. After HPLC

purification using the semipreparative column – (Agilent (Santa Clara, CA) HPLC systems equipped with a model 1200 quaternary pump and a model 1200 UV absorbance detector) with 25% acetonitrile in water containing 0.1% TFA at a flow rate of 4.5 mL/min (tR = 10.5 min), PSMA-617 was obtained in 25% yield.

In order to synthesize a lutetium-labelled tracer, a solution of PSMA-617 (5.5 mg, 5.3 μmol) was incubated with LuCl_3 (5 equivalents) in NaOAc buffer (0.1 M, 500 μL , pH 4.2) at 90 $^\circ\text{C}$ for 15 min, and then purified by HPLC using the semi-preparative column; with the following conditions: 25% acetonitrile in water with 0.1% TFA, flow rate of 4.5 mL/min (tR = 9.7 min). The yield was 62%.

Purification and quality control of the ^{177}Lu labeled peptide were performed on Agilent (Santa Clara, CA) HPLC systems equipped with a model 1200 quaternary pump and a model 1200 UV absorbance detector. The radio-HPLC system was equipped with a Bioscan (Washington, DC) NaI scintillation detector. The HPLC columns used were a Phenomenex (Torrance, CA) semi-preparative column (Luna C18, 5 μ , 250 \times 10 mm) and a Phenomenex analytical column (Luna C18, 5 μ , 150 \times 4.6 mm) [273].

3.2.2 Synthesis of [^{177}Lu]-PSMA-617

As previously described in Section 2.3, ^{177}Lu labeling was performed with 5 equivalents LuCl_3 (5 equivalents) in NaOAc buffer (0.1 M, 500 μL , pH 4.2) at 90 $^\circ\text{C}$ for 15 min, and purified by HPLC using the semi-preparative column. The HPLC conditions were 25% acetonitrile in water with 0.1% TFA at a flow rate of 4.5 mL/min.

3.2.3 [¹⁸F]DCFPyL radiolabeling

As previously described in Section 2.4, [¹⁸F]DCFPyL radiolabeling was performed according to previously published procedures [249].

Radiochemical purity was confirmed by HPLC analysis using an analytical RP-C18 column with gradients of acetonitrile and water (both containing 0.1% TFA). Molar activity values were measured based on standard curve analysis. [248, 249].

3.2.4 Cell cultures

The LNCaP cell line was obtained from ATCC (LNCaP clone FGC, CRL-1740). The cells were cultured in RPMI 1640 medium supplemented with 10 % FBS, penicillin (100 U/mL) and streptomycin (100 µg/mL) at 37 °C in a MCO-19AIC (Panasonic Healthcare) humidified incubator containing 5% CO₂. Cells grown to 80-90% confluence were then washed with sterile phosphate-buffered saline (1 × PBS, pH 7.4) and trypsinized. The collected cell number was counted with a hemocytometer and Bal Supply (Sylvania, OH) 202C laboratory counter.

The TRAMP-C2 cell culture, and the transfected clones derived thereof, were initially maintained in Dulbecco's modified Eagle's medium (DMEM) supplemented with 5% heat-inactivated FBS, 5% Nu-Serum IV, 1% penicillin/streptomycin, 0.005 mg/mL bovine insulin and 10 nmol/L dehydroisoandrosteron [250] and after one month's time and addition of 300 µg/ml of Geneticin (G418) to the media, cells were maintained in Dulbecco's modified Eagle's medium (DMEM) supplemented with 5% heat-inactivated FBS and penicillin (100 U/mL) and

streptomycin (100 µg/mL) at 37 °C in a MCO-19AIC (Panasonic Healthcare) humidified incubator containing 5% CO₂. Cells grown to 80-90% confluence were then washed with sterile phosphate-buffered saline (1 × PBS, pH 7.4) and trypsinized. The collected cell number was counted with a hemocytometer and Bal Supply (Sylvania, OH) 202C laboratory counter.

3.2.5 Transfected TRAMP cells

In this study, the tumour model used were TRAMP-C2 cells transfected with a, previously unpublished, plasmid carrying doxycycline-inducible PSMA-expression system, developed at the Deeley Research Centre (Victoria BC, Canada). The clones obtained from Deeley Research Centre, designated as clones 1, 14, 16 and 19, were IMPACT tested for contaminants upon receipt.

3.2.6 Isolating PSMA-expressing clonal populations

For the purpose of flow cytometry analysis, the clones were seeded in V-bottom 96-well-plates and pretreated with 1 µg of doxycycline hydrochloride (Sigma Aldrich, St. Louis MO, USA) per 1 ml media, 18-24 hours before the flow cytometry study. Media was removed and cells were washed with DPBS (Gibco, Carlsbad, CA, USA) supplemented with 10% fetal calf serum and 0.02% NaN₃, prior to and following a one-hour-long incubation in the dark with 1 µg of Alexa Fluor® 488 anti-human PSMA (FOLH1) Antibody (BioLegend, San Diego, CA, USA) per 10⁶ cells, whereas LNCaP cells and wildtype TRAMP-C2 cells were used as positive and negative controls, respectively. Additional negative controls were “unstained” cells - treated with

100-200 μ l/well of DPBS with 10% fetal calf serum and 0.02% NaN_3 , and isotype controls, incubated for one hour with Alexa Fluor® 488 Mouse IgG1, κ Isotype Ctrl (FC; Biolegend, San Diego, CA, USA), as well as cells without doxycycline-pre-treatment. Flow cytometry runs were performed on FACScalibur 2 Laser, 4 Color flow cytometers (Becton, Dickinson & Co., Franklin Lake, NJ, USA). Data were analyzed using FlowJo software (FlowJo LLC, Ashland, OR, USA).

Following a limit dilution of each of the four parental clones, subclonal populations were isolated and subsequently analyzed per flow cytometry studies, following the identical procedure as the parental clones with the goal of identifying homogenous subclonal populations with high level of PSMA-expression, isolated from poorly PSMA-expressing populations, as a preferable tumour model.

3.2.7 *In vivo* Studies

All animal studies were approved by the Animal Care Committee of the University of British Columbia, and in compliance with the Canadian Council on Animal Care guidelines.

3.2.7.1 Quantification and visualization of PSMA-expression in an immunocompromised model

10×10^6 cells of each of the four clones (“parental clones”: 1, 14, 16 and 19) in 200-250 μ l of media and Matrigel (1:1) were subcutaneously inoculated in the area dorsocaudomedial to the acromiotrapezius muscle of male NOD.Cg-Rag1^{tm1Mom} Il2rg^{tm1Wjl}/SzJ (“NRG”, NOD-Rag1^{null} Il2rg^{null}, NOD rag gamma) mice of 12 weeks of age and older (Jackson Laboratory, Bar Harbor,

ME, USA), using a 25 gauge needle. All mice had designations Cxy(z), x being cage number (1-22), y denoting the presence and/or the side of the ear punch (R - right, L - left, or NP - no punch), and z being number of punches (1 or 2). The harvested tumours had the same designation as the mouse that each of the tumours was harvested from. The mice were maintained in a pathogen-free animal facility with restricted access, on a 12:12 light cycle and monitored for tumour size, weight and general signs of illness following the protocol A16-0290-Mus-03 of the BCCRC Animal Resource Centre. 5-8 weeks post inoculation, mice with tumour volume of at least 200 mm³ were selected for *in vivo* imaging and biodistribution studies with ¹⁸F-labelled radiotracer DCFPyL [93, 251-254] and pre-treated with 50 mg doxycycline per kg bodyweight in 200-250 µl DPBS intraperitoneally, 36-48 hours prior to the study. Additional mice were selected as controls and did not receive the antibiotic prior to the study. A minimum of 6 mice per study were used, and per clone, a minimum of 4 mice without administered doxycycline and 9 mice with administered doxycycline were used altogether for the study of activity distributions within organs. Per clone, one mouse was selected for microPET/CT imaging before and after doxycycline induction. The range of activity for intravenous (tail vein) injection was 1.47 +- 0.28MBq for the biodistribution studies, and 5 +- 0.86 MBq for the imaging study (followed by biodistribution study unless the mouse was imaged without induction - in this case, mice were allowed to recover from anesthesia and used in another PET/CT + biodistribution study the following week).

3.2.7.1.1 PET/CT studies

PET/CT images were acquired one hour post tracer injection using a Siemens Inveon microPET/CT scanner (Siemens Medical Solutions, Knoxville, TN, USA) and reconstructed using an Inveon Research Workplace (Siemens Medical Solutions, Ann Arbor, MI, USA). *Ex vivo* biodistribution studies were performed immediately *post euthanasiam* in CO₂ (following anesthesia in 2% isoflurane in oxygen). Organs were harvested, weighed and counted on a PerkinElmer WIZARD 2480 gamma counter (PerkinElmer Inc., Waltham, MA, USA). Organ uptake was calculated in percent injected activity per gram (synonymous: injected dose per gram) tissue and an unpaired student's t-test was performed using GraphPad Prism 8 (GraphPad Software Inc., San Diego, CA, USA) with tumour uptake post doxycycline-induction in the test group and tumour uptake without doxycycline induction in the control group. The cutoff for significance was a p-value under 0.05. PET/CT images were compared side by side for the same mouse before and after induction using the same uptake bar with colour spectrum corresponding to the percentage of injected activity per gram tissue.

3.2.8 Repassaging TRAMP-C2 cells

To minimize the number of animals used in the study, a portion of tumour volume was harvested during the biodistribution study from a mouse inoculated with TRAMP-C2 parental clone 16. Harvested tissue was incubated at 37 °C for 2 hours, in 500 µl of DMEM media with 10% FBS and 1% penicillin/streptomycin and 500 µl of 10X collagenase/hyaluronidase in DMEM (Stemcell Technologies, Vancouver BC) until fully dissociated, centrifuged, and the

pellet trypsinized (0.25% trypsin-EDTA; Gibco, Carlsbad, CA, USA) to dissociate into single cells. The cells were filtered through a 40 µm cell strainer and plated in a 10 ml-plate for one hour before transferring to a new dish with fresh media. A subset of cells was later limit-diluted for the purpose of isolating fibroblast-free clonal populations with high PSMA-expression profiles.

3.2.9 *In vivo* proof of induced PSMA-expression in an immunocompetent model

Cells originating from the harvested tumour (parental clone 16) were cultured in TRAMP-media and subcutaneously inoculated into 4 C57Bl/6J mice age 12 weeks or older, dorsocaudomedially to the M. acromiotrapezius, in 200-250 µl media/Matrigel (1:1). Analog to the previously described studies (see subchapter 3.2.7.1) in immunocompromised mice, C57Bl/6J mice were monitored for tumour growth and weight until reaching the volume required for PET/CT imaging (1-2 weeks), intraperitoneally injected with 50 mg doxycycline per kg bodyweight and underwent PET/CT and biodistribution study with [¹⁸F]DCFPyL. A portion of the harvested tumour volume was dissociated and harvested cells were analyzed in a flow cytometry PSMA-expression study.

3.3 Results

3.3.1 Transfected TRAMP cells

All four parental clones received from Deeley Research Centre were confirmed to be contaminant-free in the IMPACT testing. Cells showed equally increased PSMA-expression in flow cytometry studies after having undergone antibiotic selection, regardless of the presence of Nu-serum, bovine insulin and DHEA in the media, or absence thereof.

3.3.2 Flow cytometry

The results of *in vitro* flow cytometry of parental clones are shown in Appendix A, as histogram plots of cell count versus FITC fluorescence detected in FL1-H. Except for the LNCaP cells as positive control, doxycycline-untreated cells showed identical PSMA-expressing profiles for unstained, isotype-stained and anti-FOLH1-stained tests. Upon doxycycline induction, all four parental clones showed increase in PSMA-expression upon doxycycline-induction with a shift in FL1-H fluorescence signal for anti-FOLH1-stained populations, except the negative control (wildtype TRAMP-C2 cells). All 4 clones consisted of subpopulations with a different degree of PSMA-expression, most significantly clone 14.

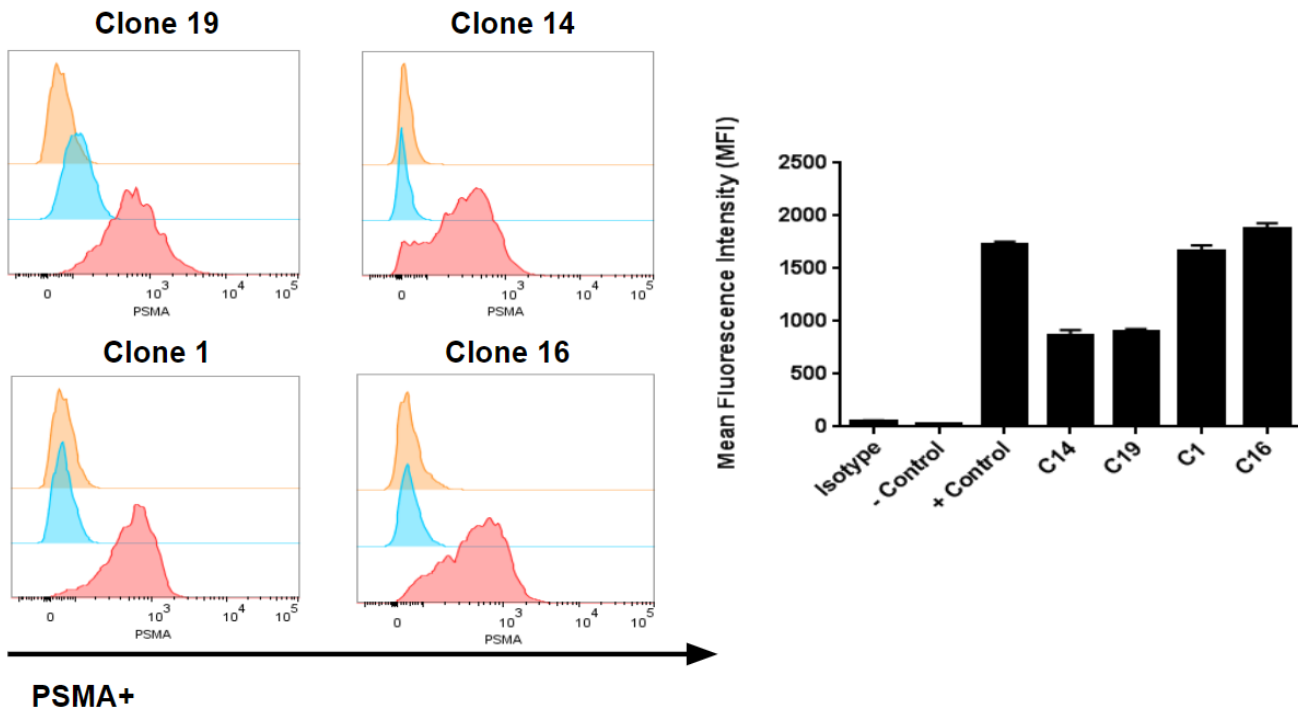


Figure 3.1. Four hPSMA expressing clones were isolated from the “bulk” population. Transduced TRAMP-C2 cells were single cell sorted to acquire clonal populations of hPSMA expressing cells. Four clones were isolated after cell sorting. Histograms and corresponding bar graph showing that clones 1 and 16 were high-PSMA expressing clones while clones 14 and 19 were medium expressing clones as analyzed through flow cytometry. Orange: doxycycline-uninduced cells; blue: isotype controls; red: doxycycline-induced cells.

3.3.3 *In vivo* proof of induced PSMA-expression in an immunocompromised model

- Imaging and biodistribution studies

Uptake of [¹⁸F]DCFPyL in NRG mice followed a similar pattern of distribution in different organs as in studies using LNCaP cells [248], with higher degrees of variability in uptake in adrenal (2.17 ± 2.3 % ID/g) and seminal glands (5.04 ± 12.32 % ID/g) due to transcontamination of sample; and urine (169.45 ± 90.49 % ID/g) due to varying vegetative patterns of each animal relative to the time of sample collection. Regardless of which clone the tumour mass originated from, pre-treatment with doxycycline significantly impacted the level of [¹⁸F]DCFPyL uptake in tumour mass (Figure 3.2), with clone 19 showing significantly lower uptake levels ($p=0.0001$). An unpaired t-test resulted in p-values under 0.0001 for all four clones, when comparing uptake levels without induction versus post induction, and PET/CT images of 4 mice, each inoculated with a different clone, confirmed this finding when images before and after induction were compared. In addition, tumours could only be visualized with high tumour-to-background ratio after undergoing induction per intraperitoneal doxycycline injection (Figure 3.2).

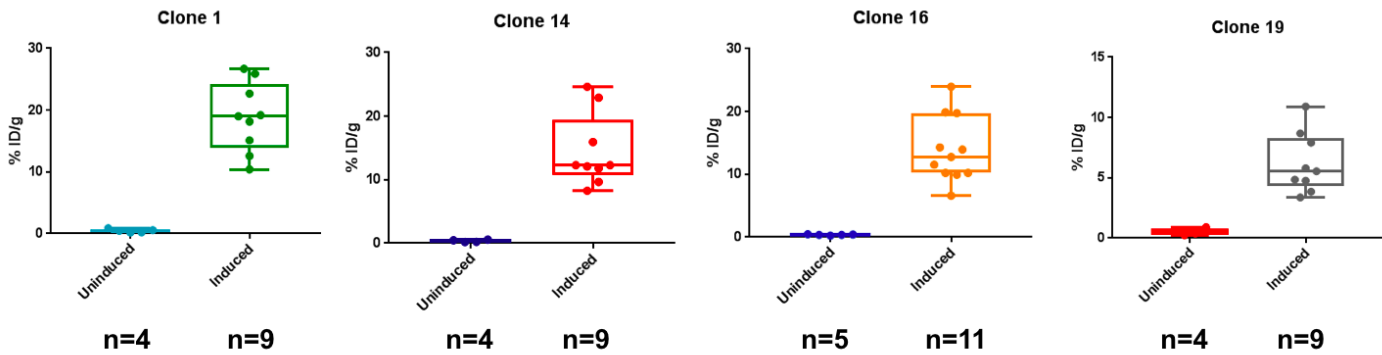


Figure 3.2. Transfected TRAMP-C2 clones express PSMA upon doxycycline-induction *in vivo*. Unpaired t-tests for all four clones showed a p-value of <0.0001 when comparing radioactivity uptake of [¹⁸F]DCFPyL, a PSMA-binding radiotracer in mice with or without pre-treatment with doxycycline. Significantly lower (p=0.0001, unpaired t-test) uptake was seen with clone 19 (mean uptake = 6.96% ID/g) when compared to clones 1, 14 and 16 combined (mean uptake = 15.43 % ID/g). %ID/g: percent injected dose (tracer activity) per gram tissue.

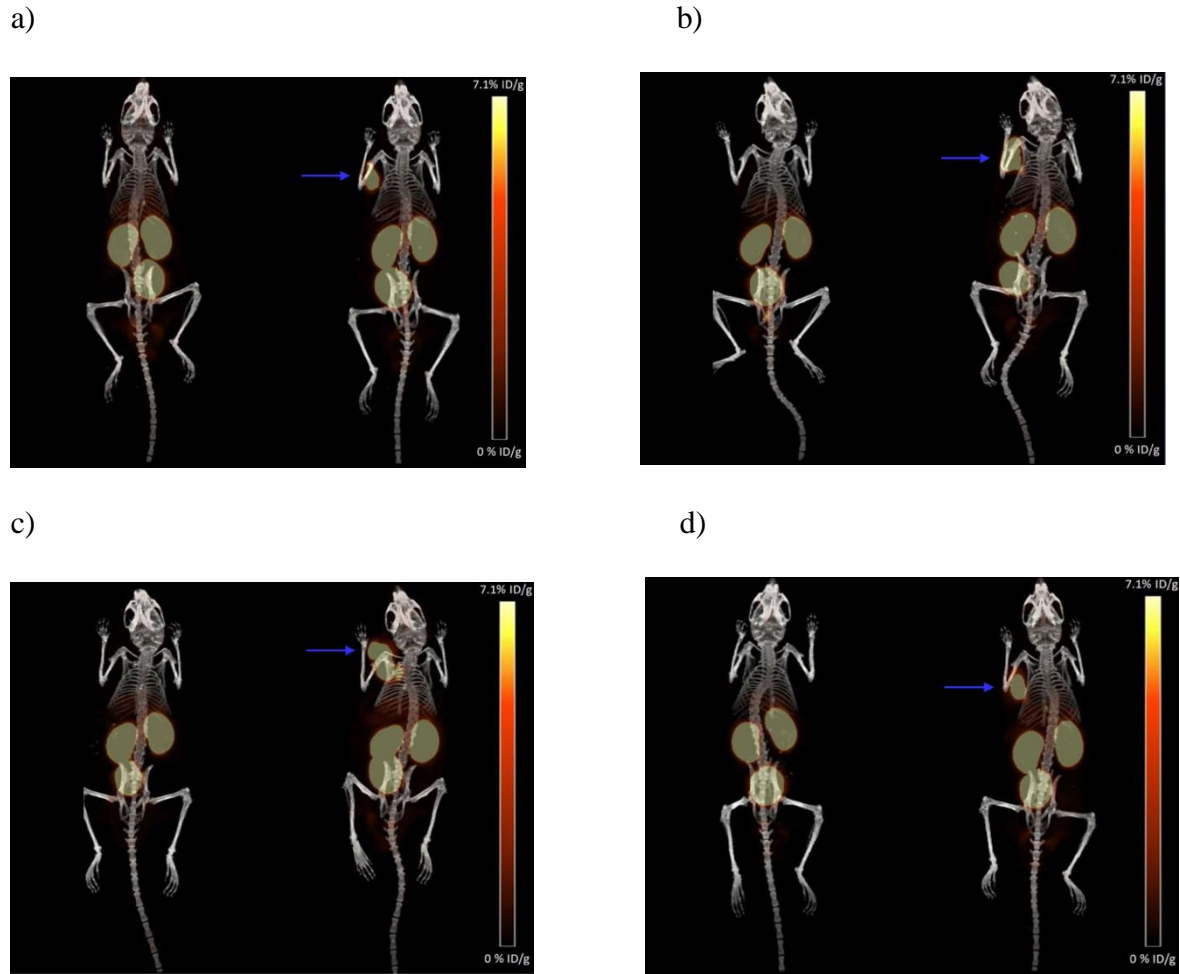


Figure 3.3. Comparison of PET/CT images before (left) and after (right) doxycycline-induction in 4 mice, each inoculated with one of the four transfected TRAMP-C2 clones: 1 (a), 14 (b), 16 (c) and 19 (d). All mice received intravenously 5 ± 0.86 MBq of [^{18}F]DCFPyL one hour before imaging. Uptake in the region tumours were inoculated in was only visualized after doxycycline administration. Physiological uptake was visualized in urinary bladder, kidneys, salivary glands, and, to a lesser extent, in liver and pancreas. Corresponding to all images are spectrum bars of 0-7.1 %ID/g for PET (yellow/red tones). Blue arrow points to the areas of increased tracer uptake corresponding to the inoculation sites of *in vivo* grown tumours. %ID/g: percent injected dose (tracer activity) per gram tissue.

3.3.4 *In vivo* proof of induced PSMA-expression in an immunocompetent model

- Imaging and biodistribution studies

On the 11th day post inoculation of 10×10^6 cells, cultured after harvesting clone 16 tumour grown in an NRG mouse, two out of four tumours in C57/B16J mice already reached a volume of 2000 mm^3 , and two remaining tumours were nearing the endpoint volume. Therefore, we performed the biodistribution study for 2 C57B1/6J mice, out of which one was imaged in PET/CT (Figure 3.4 and Table 3.1). Uptake was visualized in the corresponding area, confirming expression of PSMA upon induction, however due to the impressive size of the fast-growing mass, the biodistribution revealed 2-3 times lower uptake level than in the studies with NRG mice, but still several times above the uptake levels for uninduced expression.

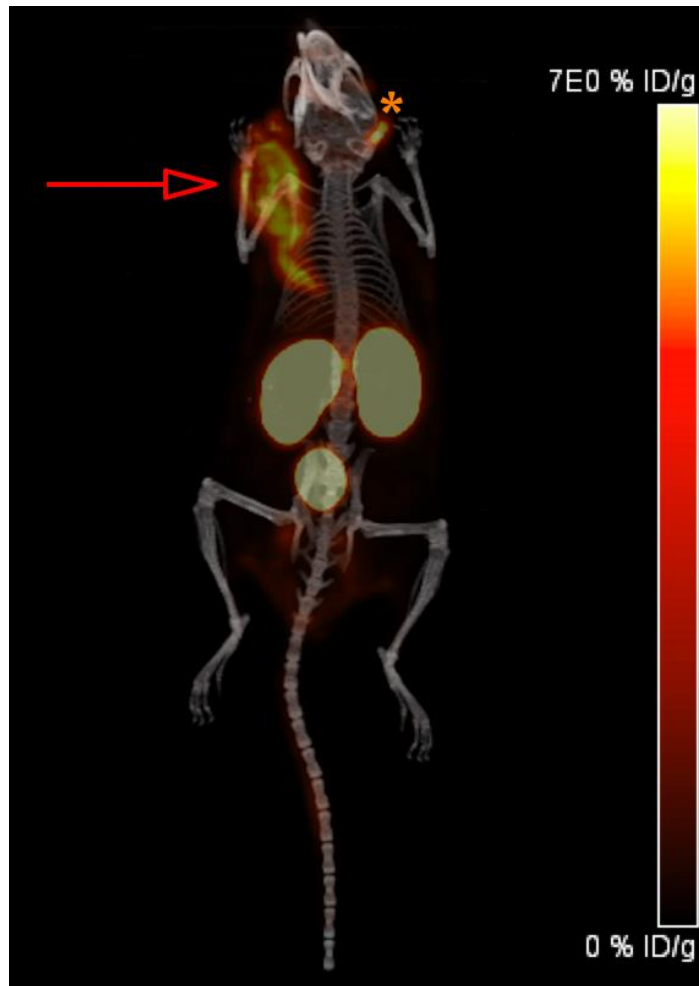


Figure 3.4. PET/CT image of a C57Bl/6J mouse, injected with 10 million clone 16-derived cells, harvested *ex vivo* from an NRG mouse and cultured in media prior to inoculation. The arrow points to the sizeable tumour mass with higher-than-background uptake levels. Star: salivary gland with increased radiotracer uptake, analog to the uptake pattern for PSMA-targeting radiotracers in pre-clinical and clinical settings. Spectrum bar for tumour uptake (0-7% ID/g) on the right. %ID/g: percent injected dose (tracer activity) per gram tissue.

Organ	Uptake in percent injected activity per gram tissue	
	<i>C1R1</i>	<i>C1RL</i>
Blood	0.59	0.71
Urine	73.77	23.44
Fat	0.83	0.49
Seminal	0.36	0.27
Testes	0.61	0.37
Intestine	1.24	0.56
Stomach	0.52	0.27
Spleen	1.74	0.85
Liver	2.45	1.39
Pancreas	0.89	0.83
Adrenal	2.18	2.15
Kidney	75.17	20.77
Lung	0.56	1.09
Heart	0.39	0.42
Tumour	5.04	2.86
Muscle	0.48	0.2
Bone	0.33	0.6
Brain	0.08	0.04
Tail	0.92	0.97
Salivary	2.43	1.28
Lacrimal	0.08	0.03
Tumor/muscle ratio	10.47	13.98
Tumor/blood ratio	8.54	4.04
Tumor/kidney ratio	0.07	0.14

Table 3.1. Biodistribution results for C1R1 and C1RL (strain C57Bl/6J), previously inoculated with cells originating from a tumour harvested from NRG strain that had previously been inoculated with clone 16 cells. C1R1 AND C1RL – tumours harvested from 2 different C57Bl/6J mice in cage #1, (C1) - right ear punched (C1R1), and both ears punched (C1RL).

3.4 Discussion

Both *in vitro* and *in vivo*, our experiments confirmed viability of cells and inducibility of PSMA-expression in all four transfected TRAMP-C2 clones. No adverse reactions were seen with the tumour model, and uptake away from the target had similar profiles as LNCaP-models (high uptake in kidney at an early timepoint post injection, due to renal tracer excretion; moderate uptake in liver, adrenal, spleen, intestine and salivary glands due to physiological PSMA-expression). Higher uptake was seen in NRG mice as compared to the C57Bl/6J mice due to the difference in tumour volumes, which is empirically known to affect tumour uptake levels [277].

The presented tumour model was confirmed to not elicit an anti-tumour immune response in immunocompetent mice and express low levels of PSMA (absence of “leaky Tet-On”) before induction [268]. This confirms the potential of PSMA e.g. as a reporting gene for successful transfection and activity of various pathways, which can be of use in immuno- or gene therapy monitoring in the clinic, but also as a tool in pre-clinical drug development for elucidating mechanisms of drug action [266, 270-272]. In clinical trials, therapeutic transgenes’ kinetics can easily be elucidated in this way, leading to improvement of agents and protocols. Studying kinetics can provide information about viability and proliferation of the engineered cells [268]. Indeed, the application field for this type of model is wide, incorporating various clinical and pre-clinical purposes. In addition, tracers targeting PSMA, such as [¹⁸F]DCFPyL used in our studies, are gaining popularity, meaning that this type of nuclear imaging technique would make this reporter gene monitoring method increasingly accessible.

The physiological pattern of PSMA expression is another reason why it is gaining interest as a reporter gene, even in monitoring T-cell function *in vivo*. Our model offers a possibility of monitoring prostate cancer cells through targeting a protein most significantly expressed in prostate cancer, with earlier discussed advantages of not expressing the protein constitutively.

Further example where this could be applied in would be the evaluation of PSMA-targeted therapy in combination with immunotherapeutics, for which this could represent an ideal model. It remains to isolate clonal, high PSMA-expressing, populations of cells in order to obtain a cell line with uniform expression and uptake patterns, and without non-cancerous cells such as fibroblasts.

Having successfully completed experiments in NRG mice for Aim 1 of this thesis, the uptake in induced PSMA-expressing cells had to be visualized in an immunocompetent model, such as the commonly used C57Bl/6J murine strain. The cells deriving from the excised tumours were able to grow rapidly once repassaged and inoculated, reaching endpoint at 11 days post inoculation. To an extent, this influenced the initial therapy study design, resulting in a large number of intended treatment groups, large treatment group sizes and extensive multidimensional experiments for each treatment group and timepoint. For this reason, the number of inoculated mice for the initial therapy study amounted to 83, in order to complete most of the intended experiments within weeks and monitor the change in tumour volume thereafter.

Chapter 4: PSMA617/anti-OX40 antitumour potency assessment

4.1. Introduction

After successfully validating PSMA-expressing clones and their viability in C57Bl/6J mice, we proceeded with experiments that were designed to verify the principal hypothesis – namely, if the combination treatment should outperform the monotherapies. This was necessary since, ideally, the cell line used for testing combination of an immunotherapeutic and a targeted radioligand is compatible with immunocompetent models, and at the same time expresses the target for the endoradiotherapeutic such as [¹⁷⁷Lu]-PSMA617.

The clone showing high PSMA-expression (Figure 3.2) in most biodistribution studies was Clone 16 (mean uptake = 13.92% ID/g; maximum uptake 19.88% ID/g). Cells deriving from excised tumours grown from this clone were shown to express PSMA in an immunocompetent model (Figure 3.4), at a high growth rate. Therapy study protocol was designed anticipating a similar growth rate; however, the protocol underwent modifications several times before the pilot study could be completed.

4.2. Materials and Methods

4.2.1 Reagents and Instrumentation; Peptide and Radiotracer Synthesis

All chemicals and solvents were obtained from commercial sources and used without further purification. ¹⁸F-fluoride was produced by ¹⁸O(p,n)¹⁸F reaction in a cyclotron TR19, purchased from Advanced Cyclotron Systems Inc. [¹⁷⁷Lu]-chloride was purchased from Isotopen

Technologien München AG (Garching, Germany) and delivered to the BCCA Cyclotron Facility.

The activity was measured using a Capintec CRC®-25R/W dose calibrator.

4.2.2 Cell cultures

The LNCaP cell line was obtained from ATCC (LNCaP clone FGC, CRL-1740). The cells were cultured in RPMI 1640 medium supplemented with 10 % FBS, penicillin (100 U/mL) and streptomycin (100 µg/mL) at 37 °C in a MCO-19AIC (Panasonic Healthcare) humidified incubator containing 5% CO₂. Cells grown to 80-90% confluence were then washed with sterile phosphate-buffered saline (1 × PBS, pH 7.4) and trypsinized. The collected cell number was counted with a hemocytometer and Bal Supply (Sylvania, OH) 202C laboratory counter.

The TRAMP-C2 cell culture, and the transfected clones derived thereof, were initially maintained in Dulbecco's modified Eagle's medium (DMEM) supplemented with 5% heat-inactivated FBS, 5% Nu-Serum IV, 1% penicillin/streptomycin, 0.005 mg/mL bovine insulin and 10 nmol/L dehydroisoandrosteron [250] and after one month's time and addition of 300 µg/ml of Geneticin (G418) to the media, cells were maintained in Dulbecco's modified Eagle's medium (DMEM) supplemented with 5% heat-inactivated FBS and penicillin (100 U/mL) and streptomycin (100 µg/mL) at 37 °C in a MCO-19AIC (Panasonic Healthcare) humidified incubator containing 5% CO₂. Cells grown to 80-90% confluence were then washed with sterile phosphate-buffered saline (1 × PBS, pH 7.4) and trypsinized. The collected cell number was counted with a hemocytometer and Bal Supply (Sylvania, OH) 202C laboratory counter.

4.2.2.1 Transfected TRAMP cells

In this study, the tumour model used were TRAMP-C2 cells transfected with a, previously unpublished, plasmid carrying doxycycline-inducible PSMA-expression system, developed at the Deeley Research Centre (Victoria BC, Canada). The clones obtained from Deeley Research Centre, designated as clones 1, 14, 16 and 19, were IMPACT tested for contaminants upon receipt.

4.2.3 Isolating PSMA-expressing clonal populations

For the purpose of flow cytometry analysis, the clones were seeded in V-bottom 96-well-plates and pretreated with 1 µg doxycycline hydrochloride (Sigma Aldrich, St. Louis MO, USA) per 1 ml media, 18-24 hours before the flow cytometry study. Media was removed and cells were washed with DPBS (Gibco, Carlsbad, CA, USA) supplemented with 10% fetal calf serum and 0.02% NaN₃, prior to and following a one-hour-long incubation in the dark with 1 µg of Alexa Fluor® 488 anti-human PSMA (FOLH1) Antibody (BioLegend, San Diego, CA, USA) per 10⁶ cells, whereas LNCaP cells and wildtype TRAMP-C2 cells were used as positive and negative controls, respectively. Additional negative controls were “unstained” cells - treated with 100-200 µl/well of DPBS with 10% fetal calf serum and 0.02% NaN₃, and isotype controls, incubated for one hour with Alexa Fluor® 488 Mouse IgG1, κ Isotype Ctrl (FC; Biolegend, San Diego, CA, USA), as well as cells without doxycycline-pre-treatment. Flow cytometry runs were performed on FACScalibur 2 Laser, 4 Color flow cytometers (Becton, Dickinson & Co., Franklin Lake, NJ, USA). Data were analyzed using FlowJo software (FlowJo LLC, Ashland, OR, USA).

Following a limit dilution of each of the four parental clones, subclonal populations were isolated and subsequently analyzed per flow cytometry studies, following the identical procedure as the parental clones with the goal of identifying homogenous subclonal populations with high level of PSMA-expression, isolated from poorly PSMA-expressing populations, as a preferable tumour model.

4.2.4 *In vivo* Studies

All animal studies were approved by the Animal Care Committee of the University of British Columbia, and in compliance with the Canadian Council on Animal Care guidelines.

4.2.4.1 PET/CT studies

PET/CT images were acquired one hour post tracer injection using a Siemens Inveon microPET/CT scanner (Siemens Medical Solutions, Knoxville, TN, USA) and reconstructed using an Inveon Research Workplace (Siemens Medical Solutions, Ann Arbor, MI, USA). Ex vivo biodistribution studies were performed immediately post euthanasiam in CO₂ (following anesthesia in 2% isoflurane in oxygen). Organs were harvested, weighed and counted on a PerkinElmer WIZARD 2480 gamma counter (PerkinElmer Inc., Waltham, MA, USA). Organ uptake was calculated in percent injected activity per gram (synonymous: injected dose per gram) tissue and an unpaired student's t-test was performed using GraphPad Prism 8 (GraphPad Software Inc., San Diego, CA, USA) with tumour uptake post doxycycline-induction in the test group and tumour uptake without doxycycline induction in the control group. The cut-off for

significance was a p-value under 0.05. PET/CT images were compared side by side for the same mouse before and after induction using the same uptake bar with colour spectrum corresponding to the percentage of injected activity per gram tissue.

4.2.5 Repassaging TRAMP-C2 cells

To minimize the number of animals used in the study, a portion of tumour volume was harvested during the biodistribution study from a mouse inoculated with TRAMP-C2 parental clone 16. Harvested tissue was incubated at 37 °C for 2 hours, in 500 µl of DMEM media with 10% FBS and 1% penicillin/streptomycin and 500 µl of 10X collagenase/hyaluronidase in DMEM (Stemcell Technologies, Vancouver BC) until fully dissociated, centrifuged and the pellet trypsinized (0.25% trypsin-EDTA; Gibco, Carlsbad, CA, USA) to dissociate into single cells. The cells were filtered through a 40 µm cell strainer and plated in a 10 ml-plate for one hour before transferring to a new dish with fresh media. A subset of cells was later limit-diluted for the purpose of isolating fibroblast-free clonal populations with high PSMA-expression profiles.

4.2.6 *In vivo* proof of induced PSMA-expression in an immunocompetent model

Cells originating from the harvested tumour (parental clone 16) were cultured in TRAMP-media and subcutaneously inoculated into 4 C57Bl/6J mice age 12 weeks or older, dorsocaudomedially to the M. acromiotrapezius, in 200-250 µl media/Matrigel (1:1). Analog to the previously described studies (see subchapter 3.2.7.1) in immunocompromised mice, mice had

designations Cxy(z), x being cage number (1-22), y denoting if ear punch was present and whether it was left or right (R, L, or NP-no punch), and z being number of punches (1 or 2). Mice cages labeling order was independent in studies in immunodeficient models versus studies in immunocompetent models, meaning that e.g. C1R1 NRG mouse is different from C1R1 in the studies using immunocompetent C57Bl6/J mice. That way we were able to keep track throughout the studies of which interventions (e.g. biodistribution, harvesting) were done with each mouse. Harvesting was always performed as part of biodistribution studies (each organ including tumour tissue was gammacounted in a vial, blood volume was entirely collected first to avoid contamination of results, and each organ is then washed in PBS. This is described in chapter 3.3.3 C57BL/6J mice were monitored for tumour growth and weight until reaching the volume required for PET/CT imaging (1-2 weeks), intraperitoneally injected with 50 mg doxycycline per kg bodyweight and underwent PET/CT and biodistribution study with [¹⁸F]DCFPyL. A portion of the harvested tumour volume was dissociated and harvested cells were analyzed in a flow cytometry PSMA-expression study.

4.2.7 Initial therapy study protocol

We designed a therapy study protocol for pre-clinical assessment of the proposed combination therapy, in comparison with the monotherapies and controls (Figure 4.1).

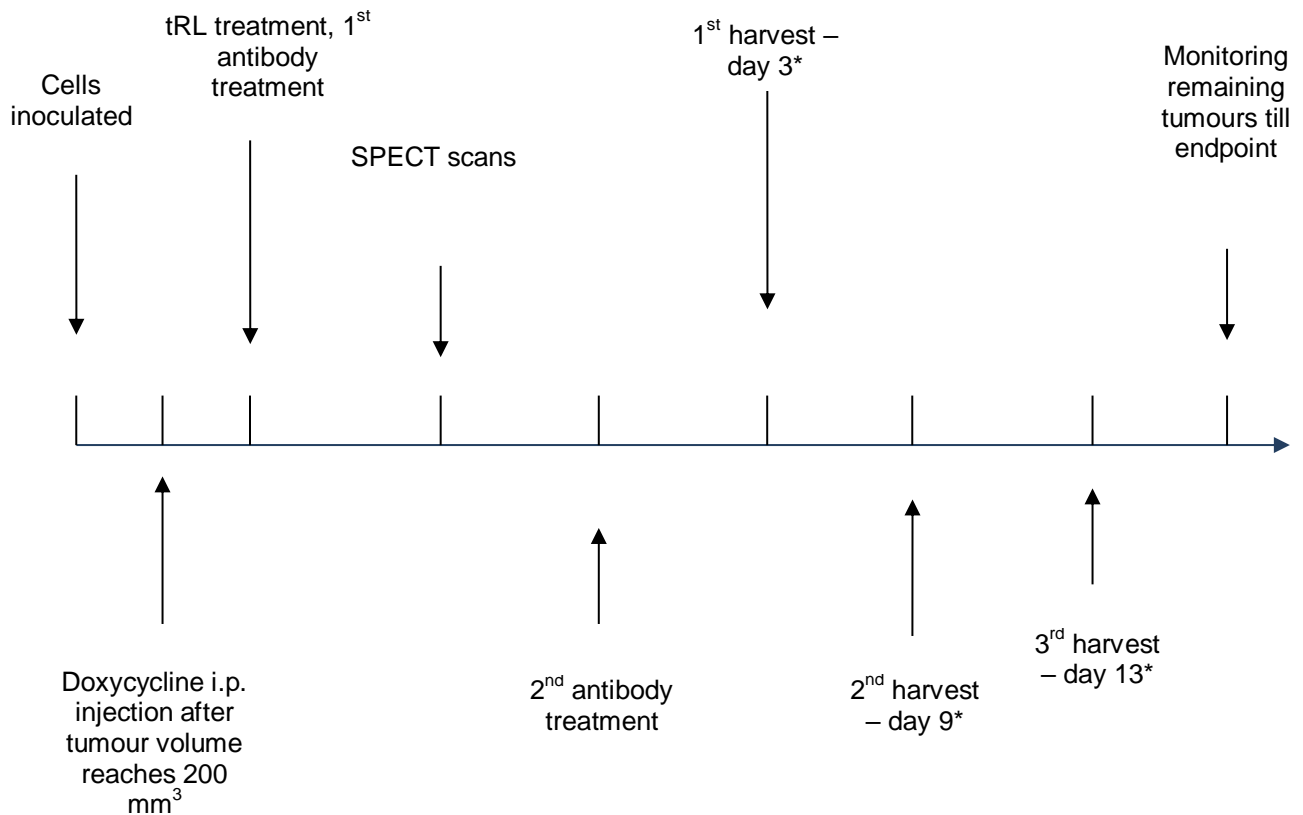


Figure 4.1 – A simplified scheme of the proposed therapy study protocol. Not to scale. *In parallel with harvesting tumours for autoradiography, staining and FACS studies, SPECT images are collected to confirm radiotracer accumulation in tumour. Harvesting tumours was performed from different mice on different timepoints. Timepoints were selected following TIL -infiltration patterns, as reported in literature [185]. i.p. intraperitoneal(ly), tRL: targeted radioligand,

For the first pass of the therapy study, 83 male C57Bl/6J mice, age 12 weeks or older, were inoculated with 10 million clone 16, subclone Q13, TRAMP-C2 cells, subcutaneously into the left dorsum. The mice had previously been attended to according to BCCA animal protocol

#A16-0128 (FB)-02, weighed and monitored for signs of illness at least once per week. Prior to inoculation, mice were assigned to treatment groups as shown in Table 4.1.

Group#	Intervention	Number of animals
0	No treatment	3
1	PSMA617 plus OX86	16
2	PSMA617	16
3	OX86	16
4	PSMA617 plus IgG2a	16
5	IgG2a	8
6	PBS	8

Table 4.1. Size of treatment groups according to the initial therapy study protocol. IgG2a: an immunoglobulin G subclass 2a control isotype; OX86: an agonist antibody targeting OX40. Note: by “PSMA617”, a lutetium-177-labelled compound is meant in this table, i.e. [¹⁷⁷Lu]Lu-PSMA617.

Post inoculation mice were monitored in intervals of at least 48 hours until palpable tumour mass was formed. 48 hours prior to first treatment (timepoint= -48h), each mouse receives 2.5 mg/kg intraperitoneal doxycycline injection. At timepoint 1 (=0h):

- 16 mice were to receive intraperitoneally 10 mg/kg bodyweight of OX86 (anti-OX40 antibody), followed by an intravenous injection of ~18.5 MBq (=0.5 mCi) [¹⁷⁷Lu]Lu-PSMA617 – Treatment Group 1;
- 16 mice were to receive intravenously 18.5 MBq (=0.5 mCi) [¹⁷⁷Lu]Lu-PSMA617 – Treatment Group 2;
- 16 mice were to receive intraperitoneally 10 mg/kg bodyweight of OX86 (anti-OX40 antibody) – Treatment Group 3;
- 8 mice were to receive intravenously 250 µL of PBS control – Treatment Group 6;
- 16 mice were to receive intraperitoneally 10 mg/kg bodyweight of IgG2a followed by an intravenous injection of 18.5 MBq (=0.5 mCi) [¹⁷⁷Lu]Lu-PSMA617 (anti-OX40 antibody isotype) – Treatment Group 4;
- 8 mice were to receive intraperitoneally 10 mg/kg bodyweight of IgG2a (anti-OX40 antibody control isotype) – Treatment Group 5;
- 3 mice are euthanized, their tumours (n=3), and one spleen is harvested for the baseline FACS studies (CD3, CD4, CD8, CD16/CD32, CD19, CD44, CD62L, CD69, PD-1, OX-40, TNF- α , TCR- β , IFN- γ) – group 0.

At timepoint 1a (= +24h), SPECT/CT scans were to confirm tracer uptake in tumour tissue for treatment groups #1, 2 and 4.

At timepoint 2 (= +48h), a second dose of the antibodies was to be administered:

- 16 mice in Treatment Group 1 were to receive intraperitoneally 10 mg/kg bodyweight of OX86 (anti-OX40 antibody);

- 16 mice in Treatment Group 3 were to receive intraperitoneally 10 mg/kg bodyweight of OX86 (anti-OX40 antibody);
- 16 mice in Treatment Group 5 were to receive intraperitoneally 10 mg/kg bodyweight of IgG2a;
- 8 mice in Treatment Group 6 were to receive intraperitoneally 10 mg/kg bodyweight of IgG2a.

According to the protocol, 2 hours before euthanasia at harvest timepoint 3 (= +72h), to 4 mice in each of the Treatment Groups #1, 2, 3 and 5, and to 2 mice in Treatment Groups 4 and 6, 250mg/kg Edu and 60 mg/kg pimonidazole per mouse are administered by an intraperitoneal injection, and 10 minutes before euthanasia Hoechst 33342 perfusion marker is administered by an intravenous injection. After euthanasia, tumours are harvested and flash frozen in a cassette with tissue tek (on dry ice for 10 minutes), transferred to -20 °C freezer and subsequently cryosectioned for betaimaging (16 µm thickness) and IF staining (10 µm thickness; to be stained for registration of anti-mouse IgG2a, Edu, caspase 3, Hoechst 33342, γ -H2AX, CD31 and pimonidazole accumulation in tissue).

At harvest timepoint 4 (= +120h), 2 mice in each treatment group were to be euthanized following pimonidazole, Edu and Hoechst 33342 administration, their tumours harvested and flash frozen in a cassette with tissue tek (on dry ice for 10 minutes), transferred to -20 °C freezer and subsequently cryosectioned for betaimaging (16 µm thickness) and IF staining (10 µm).

At harvest timepoint 5 (= 9 days = 216h), 4 mice in each of the treatment groups #1, 2, 3 and 5, and 2 mice in treatment Group 4 and 6 in are euthanized after pimonidazole, Edu and Hoechst 33342 administration, their tumours harvested and flash frozen in a cassette with tissue

tek (on dry ice for 10 minutes), transferred to -20 °C freezer and subsequently cryosectioned for IF staining (10 µm). In each group, small tumour samples and spleens are harvested for FACS studies on splenocytes and tumour tissue cells.

At harvest timepoint 6 (= 13 days = 312h) 2 mice in each treatment group are euthanized (after pimonidazole, Edu and Hoechst 33342 administration as described for timepoint 3), their tumours harvested and flash frozen in a cassette with tissue tek (on dry ice for 10 minutes), transferred to -20 °C freezer and subsequently cryosectioned for betaimaging (16 µm thickness) and IF staining (10 µm).

The remaining 4 mice in each of the treatment groups #1, 2, 3 and 5 were monitored every 48 hours for general signs of illness, tumour size (measured with a caliper) and bodyweight. The longest diameter of the tumour parallel to the scapular line was registered as tumour length; the longest diameter of the tumour perpendicular to the scapular line was registered as tumour width. The volume of each tumour was calculated using a formula $Volume = (Width\ squared \times Length) / 2$ [256, 257], bodyweight and tumour size data were plotted against time and compared between treatment groups. Once a humane endpoint of tumour volume measuring $>1000\text{ mm}^3$, on more than three consequent measurements, or more than 5 consecutive days; or in case body weight loss was $>20\%$ compared to any previously measured weight, animals were euthanized after sedation in 5% isoflurane in oxygen.

In euthanized mice, tumours and spleens are harvested, $<30\%$ of each tumour sample is stored for preparation of cell suspension, the rest is flash frozen. Both frozen samples and cell

suspensions are sent to Deeley Research Centre for further FACS and histological analysis (CD3, CD4, CD8, CD16/CD32, CD19, CD44, CD62L, CD69, PD-1, OX-40, TNF- α , TCR- β , IFN- γ).

The first pass of the therapy experiment was designed as described above. A repeated experiment with the same design was planned. Table 4.2 summarizes the timepoints and the pertaining procedures as foreseen by the study protocol.

Timepoint	Procedure	Number of mice
(-14 days)	Inoculated 10 million cells	86
(-5 d)	Tumours/spleens harvest	3
(-2 d)	Doxycycline i.p.	80
0	Treatments	80
1	3 SPECT scans	3
2	OX40/IgG2a second injection	56
3	First harvest – 72 h	20
5	Second harvest – 120 h	12
8	Third harvest	20
9	(Peak TIL infiltration) [187]	
13	Fourth harvest	12
15	Monitoring remaining mice till endpoint	16

Table 4.2. Simplified scheme of study timepoints according to the initial protocol. SPECT; single photon emission computed tomography

For reasons discussed in this chapter, first-pass experiment was performed following an adapted scheme, as shown in Tables 4.3 and 4.4.

Timepoint	Procedure	Number of mice
(-70 days)	Inoculated 10 million cells	86
(-5 d)	Tumours/spleens harvest	3
(-2 d)	Doxycycline i.p.	16
0	Treatments	16
1	2 SPECT scans	2
2	OX86 second injection	8
3	First harvest – 72h	6
5	Second harvest 120 hour	0 (2 SPECT scans only)
9	Third harvest (Peak TIL)	6
13	Fourth harvest	0 (only SPECT*2)
15	Monitoring remaining mice till endpoint	4

Table 4.3. Simplified scheme of study timepoints in the first-pass experiment, according to the adapted protocol.

Group	Intervention	Number of mice
0	No treatment	3
1	Lu-PSMA617 plus OX86	8
2	Lu-PSMA617	8
3	OX86	<i>omitted</i>
4	Lu-PSMA617 plus IgG2a	<i>omitted</i>
5	IgG2a	<i>omitted</i>
6	PBS – <i>converted to “no treatment”</i>	3

Table 4.4. Size of treatment groups according to the adapted therapy study protocol.

As it was intended in the initial design, only mice with tumours of a certain volume were about to be included in the therapy study, in order to have comparable sizes at timepoint of the first treatment, e.g. 200-600 mm³, and therefore comparable tracer/drug uptake. This was not possible since the tumours began forming with delay from the expected time, and at different timepoints. Therefore by the time the first pass therapy study could be organized, there were few tumours already formed, and with varying tumour volumes. However for the purpose of the pilot study, those mice were used and the study continued with reduced sample size.

For the same reason, it was not possible to randomize the tumours to each treatment arm, so that similar numbers of very small, medium, very large etc. tumours are present in each treatment group in the pilot study.

Timepoint	Procedure	Number of mice
(-112 days)	Inoculated 10 million cells	86
(-101)	Tumours/spleens harvest	3
(-2)	Doxycycline i.p.	16
0	Treatments; controls harvest	16 (3 controls)
1	2 SPECT scans	2
2	OX86 second injection	7
3	2 SPECT scans	2
5	1 SPECT scan	1
9	Third harvest (Peak TIL)	<i>omitted</i>
13	Fourth harvest	<i>omitted</i>
15	Monitoring remaining mice till endpoint	13

Table 4.5. Simplified scheme of study timepoints in the second-pass experiment according to the adapted protocol

4.3 Results and Discussion

4.3.1 Tumour growth inhibition curves

All tumours in the control group exhibited steady growth over time. Volumes were plotted against time, beginning with the initial volume at the timepoint the tumour mass was palpable, until the endpoint ($V > 1000 \text{ mm}^3$ on two consecutive measurements).

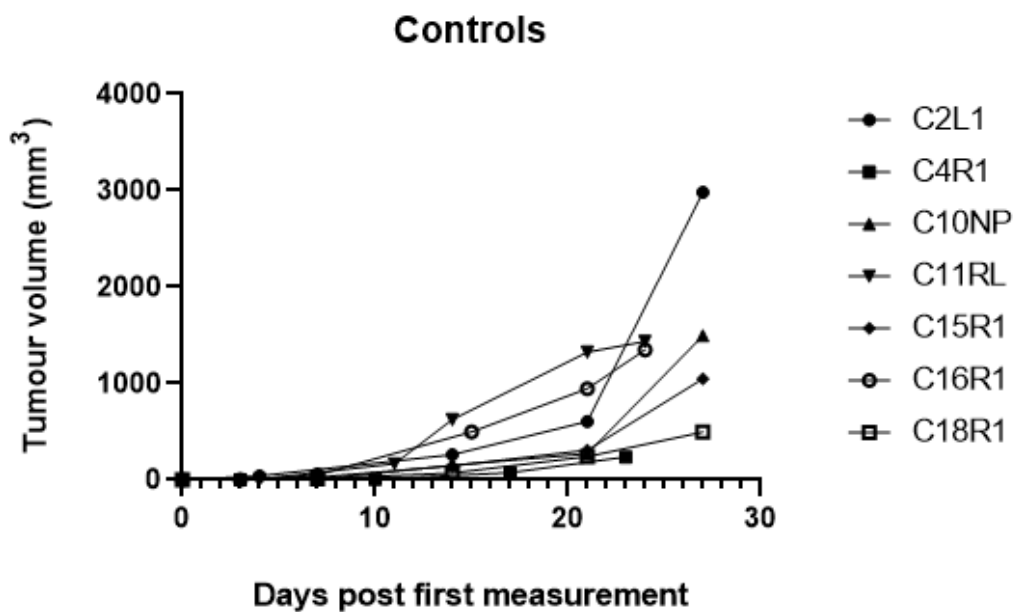


Figure 4.2. Graph showing tumour volumes in control group, from the first timepoint at which any formed mass was visible and palpable, until the endpoint (euthanasia or study termination; measured at least every 7 days). No reduction in volume for any of the tumours was detected. C2L1 - C18R1 – IDs of animals inoculated with TRAMP-C2 subclone Q13, not treated with neither of the agents in the therapy study.

In the control group, the growth was continuous for all the tumours measured (Figure 4.2, n=7). There was no bending or flattening of the curves that would indicate inhibition of tumour growth. No treatment was the only control in the final study design. Treatment groups with PBS (TG #6) and control IgG2a (TG #5) were discarded in the modified study protocol due to reduced sample size (Figure 4.3 shows unequal distribution of tumour volumes and presence of tumours in a small subset of inoculated animals 70 days post inoculation) since the primary goal of the pilot study was to detect any superiority of the combination treatment versus monotherapy. We did not expect the intervention itself versus absence of any intervention (PBS versus no treatment) to affect the results, hence TG #6 was not included in the pilot study, and was replaced by including more tumours in TG #0.

The same was decided for treatment group #5, since any tumour growth-inhibiting effect of the control IgG2a would mean an effect due to non-specific binding of the immunoglobulin isotype. We did not expect this treatment arm to differ significantly from controls in group 0, and for the same reason less animals were planned in this treatment arm already in the initial study design. Including this treatment arm would make sense in a larger, expanded therapy study, in order to establish whether the potential therapeutic effect of OX86 relies specifically on binding to the surface antigen OX40.

Following the same principle, we were able to omit Treatment Group #4 (targeted radioligand in combination with the control IgG2a), since no superior effect of this combination in comparison with the effect of targeted radioligand-monotherapy was expected. Again, in a larger therapy study, assuming that a stably PSMA-expressing subclone is identified and used, this treatment group could give answers to whether non-specific binding contributes to tumour growth inhibition, when used in combination with targeted radioligand therapy.

Finally, between Treatment Groups #2 (targeted radioligand monotherapy) and #3 (agonistic immunotherapeutic antibody), we decided to limit the pilot study to the targeted radioligand lutetium-177-PSMA617, since its effects as a monotherapy have previously been reported in similar models [273] and in clinical studies, therefore, a potentially superior therapeutic effect of the combination treatment (Treatment Group #1) could best be established in comparison with the targeted radioligand monotherapy (Treatment Group #2).

Tumour volumes 70 days post inoculation

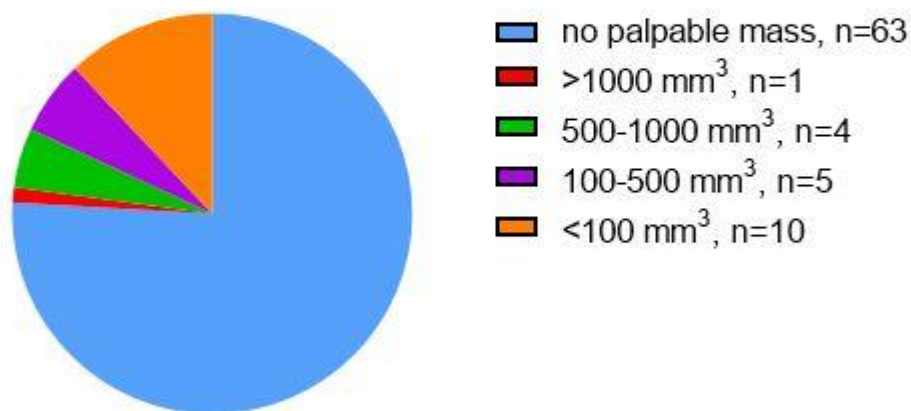


Figure 4.3. 70 days post inoculation more than three quarters of the inoculated mice showed no palpable/visible mass forming *in vivo*. The formed tumours were, however, used in the studies, although some of them were either smaller or larger than the volumes used in similar experiments (usually 200-600 mm³ [276]).

For the principal aim of this thesis, and in order to test the hypothesis, in each of the treatment arms a subset of animals were treated and intended for monitoring weight and tumour volume. Comparable trends were anticipated that can provide information on antitumour activity in each treatment arm. In other words, in order to confirm or reject the principal hypothesis, different therapeutic potency had to be clearly visualized, and statistically proven, when comparing Treatment Arms #1 and #2.

To an extent, the resulting curves (volume plotted against time) demonstrated intertumoural heterogeneity regarding size.

As previously mentioned, treatment groups #1 and #2 were selected as the crucial ones to focus on in the first pass of the study, since the treatment with [¹⁷⁷Lu]-PSMA617 was already known to show favourable outcomes in clinical studies, and also in studies similar to this, using animal models [273]. Therefore Treatment Group #2 remained included in the study. The contribution of this study was aimed at showing advantages of the combination treatment. For that reason, Treatment Group #1 was also included in the modified study protocols.

The reduced sample size resulted in eliminating threshold volume (>200 mm³ in the initial protocol) as a criteria for inclusion. In consequence, any palpable tumour volume below endpoint was included in the modified treatment protocol, in order to make best use of the available formed tumours in C57Bl/6J mice. Resulting intertumoural heterogeneity regarding size could also influence trends in growth inhibition, namely large tumours tended to grow at a steady rate, whereas small tumours were more likely to regress over time (Figure 4.4). As an example, tumours larger than 1000 mm³ (C9L1, C13RL, C20RL in Figure 4.4) did not show reduction in tumour volume over time and reached endpoints early in the study. On the other hand, those tumours which were barely visible and palpable as tiny masses at the beginning of the therapy

study (C2RL, C7NP, C9NP, C13R1 or C21RL) but still had to be included in the pilot study due to reduced sample size, remained with volumes close to 0 mm³ until endpoints. Based on this observation, we suspect that the tumour size at timepoint 0 did affect the growth inhibition curve. This can be supported by the previously mentioned effects of tumour size on drug distribution [277]. Since these tumours belonged to both treatment groups (C2RL, C9NP and C21RL – Treatment Group #1; C7NP and C13R1 – Treatment Group #2), this further corroborates the hypothesis that the initial tumour size could have affected the shape of the resulting growth inhibition curve.

Treatment groups 1&2 - therapy study

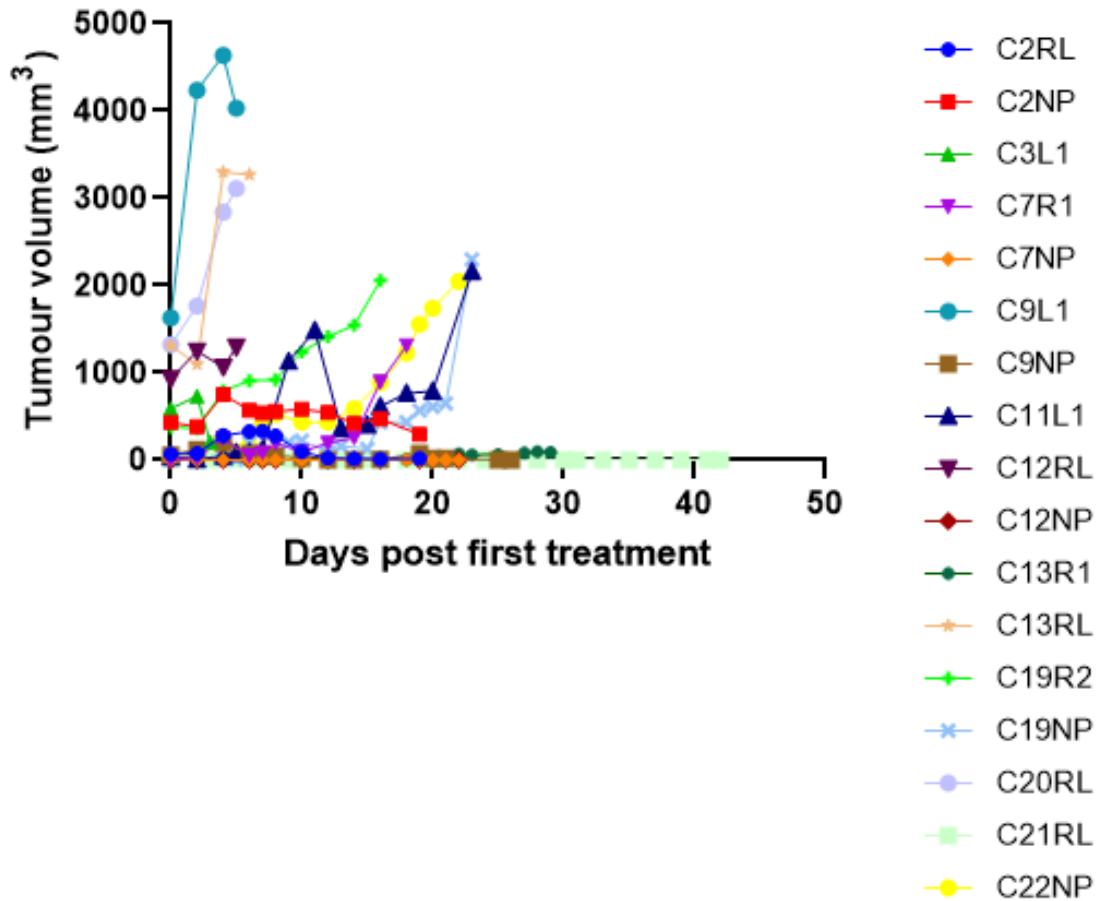


Figure 4.4. Volume of tumours monitored for growth inhibition, plotted over time, in treatment groups #1 and #2. Note that e.g. tumour ID C3L1 was harvested at day 3 p.i. for the purpose of FACS studies, autoradiography, immunostaining etc. and could not be monitored until reaching the endpoint. p.i.: post injection

The tendency of large tumours to reach endpoint early on in the experiment is better visualized in the graphs in Appendix B.

In treatment group #1 (Figure 4.5) this tendency is evident, since e.g. tumour IDs C6L1, C20R1 do not show any signs of growth inhibition, and tumour ID C9L1 shows limited inhibition, resulting in reaching endpoint at day 5 post inoculation.

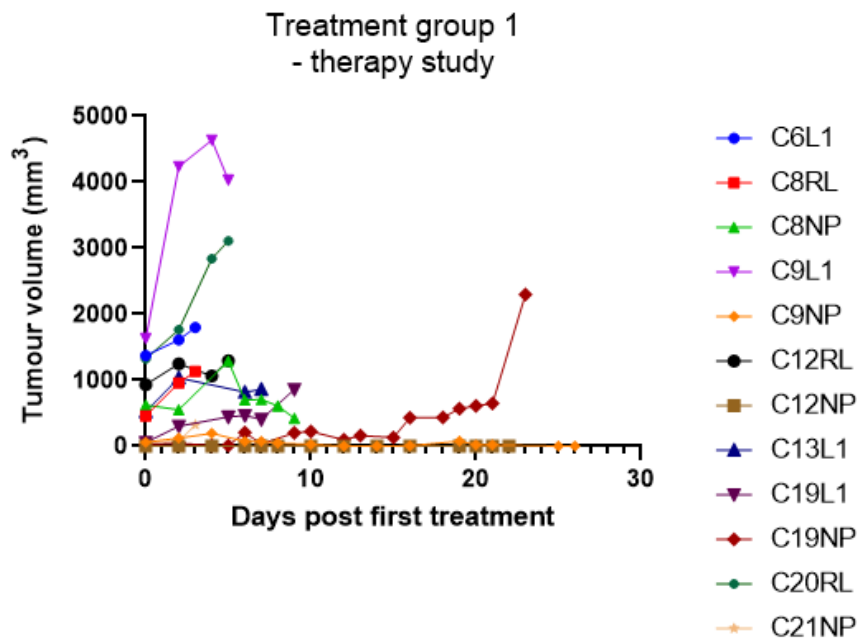


Figure 4.5. Volume of tumours monitored for growth inhibition in Treatment Group #1, plotted over time in days post first treatment.

Tumour volume in C21RL did not reach endpoint until the termination of the study, showing no palpable tumour volume up until day 42 post first treatment.

Of note is that in both treatment groups #1 (combined treatment) and #2 (endoradiotherapeutic), several tumours showed a rather pronounced growth inhibition between day 2 and day 13 p.i. This can be interpreted as the result of the abscopal effect, since TIL-infiltration in previous pre-clinical models was found to commence 3 days post radiotherapeutic treatment, peak around 9 days, and recede to the baseline around day 13. The examples of this tendency were visible especially for tumour IDs C12RL, C13L1 and C2RL in Treatment Group #1., and C11L1, C20NP and C22NP in Treatment Group #2 (Figures 4.6 and 4.7).

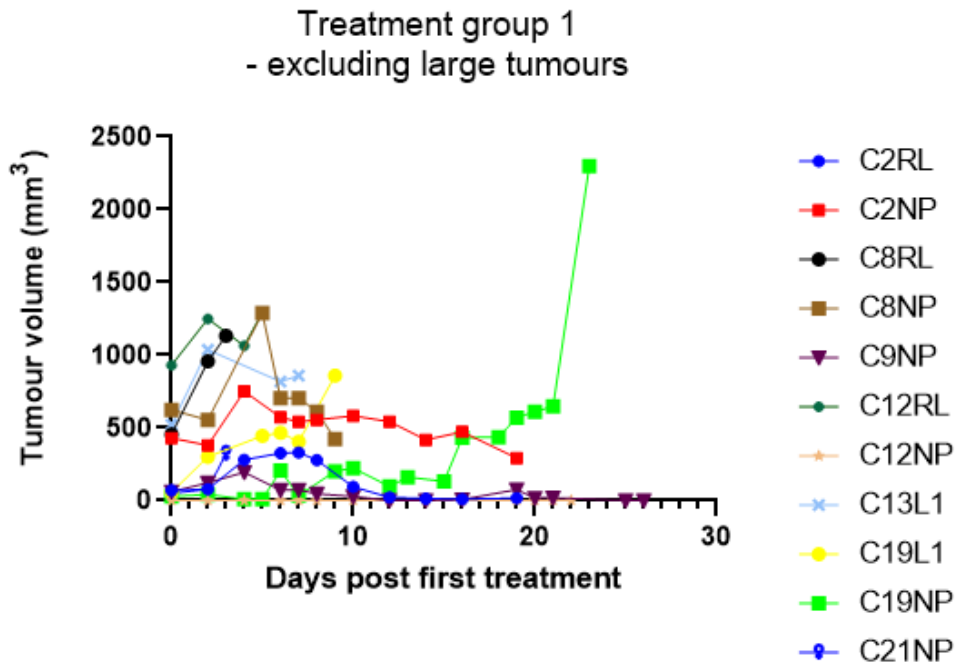


Figure 4.6. Volume of selected tumours monitored for growth inhibition in Treatment Group #1, excluding tumours with large volumes at timepoint 1, and tumours monitored past day 26 post inoculation.

Figure 4.6 shows the tumours in the same treatment group as 4.5, however it excludes mice C6L1, C9L1 and C20RL, which had large tumours at the timepoint of the treatment, which affected their survival time post treatment. In other words, with tumours that are larger, the treatment with the same dosage of both radioligand and antibody is likely to achieve the same therapeutic effect (in this case a weak tumour growth inhibition is evident) regardless of the treatment group. Therefore they are visualized in one graph.

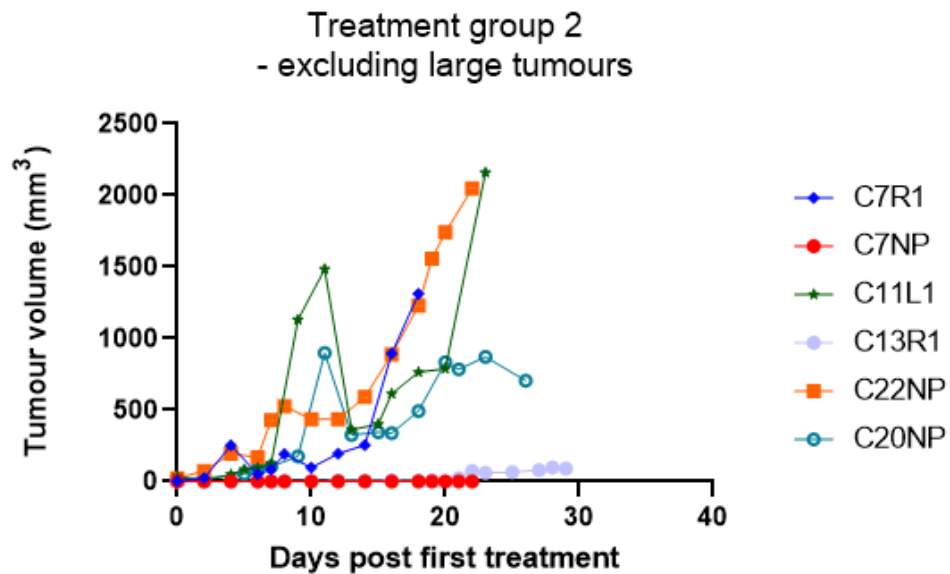


Figure 4.7. Volume of selected tumours monitored for growth inhibition in Treatment Group #2, excluding tumours with large volumes at timepoint 1.

More interestingly so, for tumour IDs C20NP, and to a lesser extent C11L1, tumour growth inhibition seems to be affected past day 13, potentially signifying ongoing immune activation. In the Treatment Group #1, the same effect is pronounced in tumour IDs C2RL and C2NP.

The reason for showing more graphs for each treatment group was that, if we eliminate very large tumours that reach endpoint relatively soon after the treatment, some degree of curve flattening can better be visualized for the smaller tumours, since the maximum volume on the y axis is smaller (different scale).

Figure 4.7 shows a subset of tumours with tumours already showing up and palpable, but relatively small so at this scale the volume at timepoint 0 days post treatment seems close to 0 mm³. It makes sense to compare these curves with those in Figure 4.2, where control tumours are monitored (no treatment) from the timepoint where any tumour mass was visible and palpable. By comparing them, we can conclude that growth inhibition does happen (as expected) with targeted radioligand treatment only.

Unfortunately, the sample size of this pilot study limits the potential of deriving significant information from the described trends. However, the shape of the therapy response curves for tumour IDs C2RL and C2NP possibly speaks for an incremental role of OX86 as a therapeutic. As a matter of interest, in Treatment Group #1 OX86 was administered on the same day as [¹⁷⁷Lu]-PSMA617, and an additional booster dose 48 hours later. This too could possibly affect the growth inhibition.

For statistical analysis, we performed an unpaired one-tailed t-test with unequal variances, applied to the incremental change in tumour volume between the Timepoint 0 (first treatment timepoint in Treatment Group #1 and the treatment timepoint in Treatment Group #2) and 20 days post Timepoint 0. Volumes of the tumours with IDs C2RL, C2NP and C13R1 were measured at 19 and 21 days post Timepoint 0, therefore for these tumours the timepoint of 19 days was accepted, instead. The resulting *p*-value amounted to 0.0263, showing that the treatment outcome was superior in Treatment Group #1.

To conclude, positive therapeutic effects were evident in both groups, however the data supported use of the combined treatment versus monotherapy.

4.3.2 Survival

After excluding all tumours that were harvested for different purposes than reaching humane endpoint (e.g. biodistribution, FACS studies, autoradiography studies, immunostaining; see Chapter 5), a Kaplan-Meier curve was plotted (Figure 4.8), showing survival probability in both treatment groups.

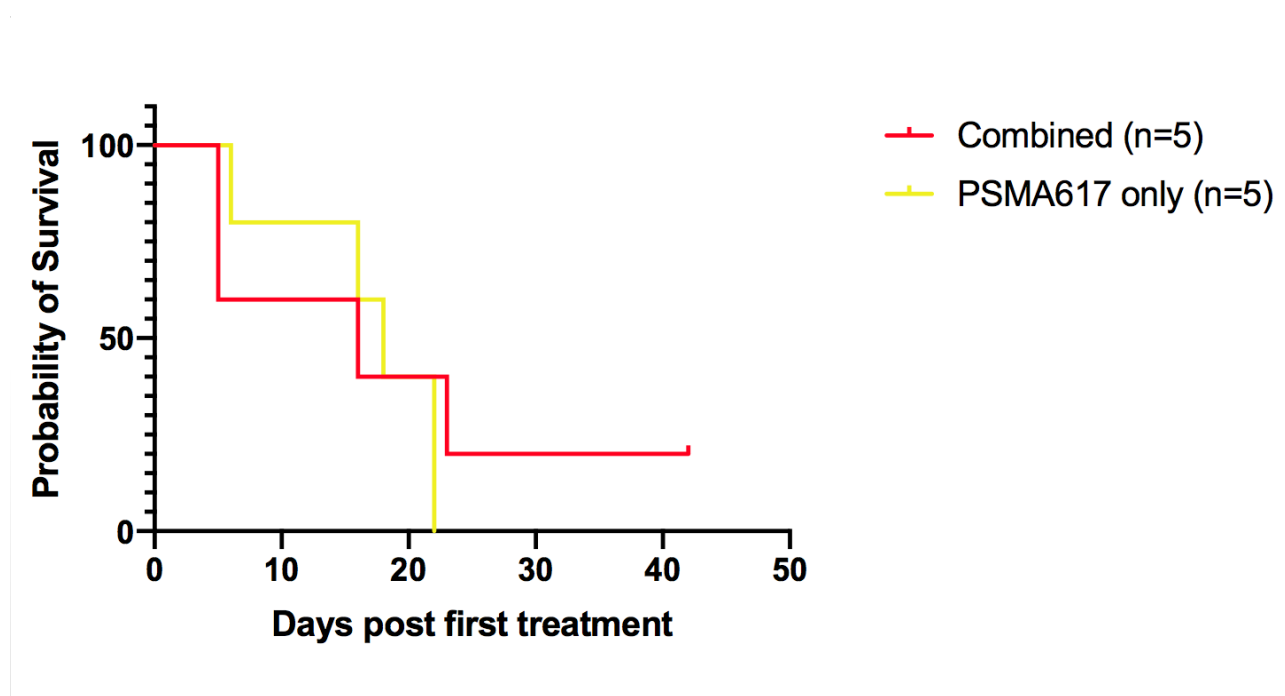


Figure 4.8. Kaplan-Meier curve showing probability of survival in Treatment Groups #1 (combination treatment with [^{177}Lu]Lu-PSMA617 and OX86; n=5) and #2 ([^{177}Lu]Lu-PSMA617 only; n=5).

Due to the small sample size in each group (n=5), these results have conditional value. A larger study, likely with a different design, could help clarify if indeed the combined treatment increases survival rates.

4.3.3 SPECT imaging

SPECT scans were scheduled for days 1, 3 and 9 post injection of radiotracer. The rationale for performing these scans was confirming tracer uptake in the newly established tumour model, establishing whether there is homogeneity between tumours and treatment arms, and monitoring changes in accumulation over time.

At day 1 post injection, uptake in tumour ID C19L1 was not visualized in a SPECT/CT scan, which naturally remained the same up until day 9 p.i. (Figure 4.9).

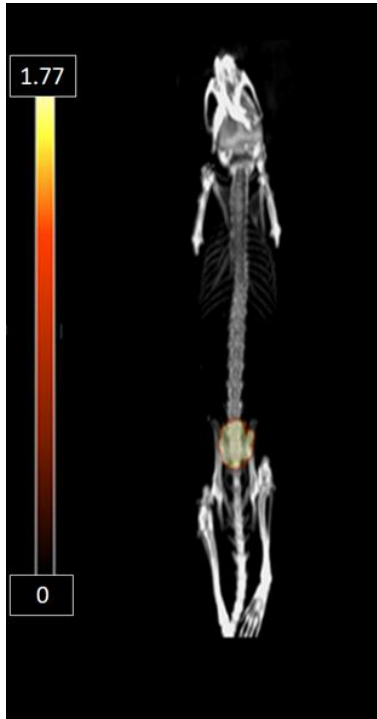


Figure 4.9. SPECT/CT image 24 hours post injection of [^{177}Lu]-PSMA617 and the first dose of OX86 antibody, mouse ID C19L1. Uptake in bladder is visualized. Tumour injected in the upper left dorsum. Bar: relative voxel intensity scale (no unit).

However, at the same timepoint, the imaged C57Bl/6J mouse from Treatment Arm #2 showed uptake in the tumour mass (Figure 4.10).

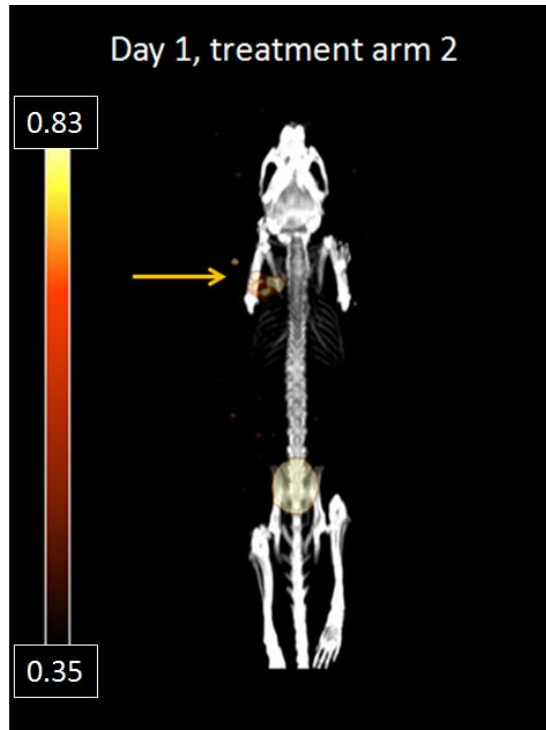


Figure 4.10. SPECT/CT image 24 hours post injection of [^{177}Lu]-PSMA617, mouse ID C9R1. Uptake in bladder and tumour mass is visualized. Tumour injected in the upper left dorsum. Bar: relative voxel intensity scale. Arrow pointing to the site of the tumour mass inoculation. The volume at this timepoint was 448 mm^3 , whereas at timepoint 0 it was 592 mm^3 , which speaks for efficient radioligand therapy to an extent.

Bar: relative voxel intensity scale (no unit).

Next, already at day 3 the tumour uptake in the inoculated tumour mass was significantly reduced to near-background levels (not shown). These results raised doubts about the efficiency of radioligand therapy in the proposed model. The fact that the uptake of the tracer in the tumour tissue could not be visualized at already such an early timepoint was not encouraging, since the aim was to grow PSMA-expressing tumours, and we could confirm that a PSMA-targeting tracer

was successfully injected into mouse, which can be seen from the high uptake in the bladder. The visualized low tumour uptake is consistent with the changes in tumour volume we measured – the volumes remained similar till day 7, and reaching $\sim 900 \text{ mm}^3$ at day 9, when the tumour was harvested for *ex vivo* studies. Ideally, an endoradiotherapeutic agent in a good tumour model would have to be detectable in tumour tissue and cleared from off-target tissues after this time, in order for cytotoxic emission to have an antitumour effect.

Later in Chapter 5 it will be explained how in autoradiography studies the issue at stake could be identified - the subclone inoculated into the mice did not express PSMA uniformly and at high levels. Hence, what we see here as a SPECT/CT image is later visualized in betaimages – a good model would have to express PSMA upon induction uniformly and at high levels.

In the second-pass study (see Chapter 2, section 2.9 for details), however, uptake in tumour mass was visualized in Treatment Group #1, at days 3 and 5 post injection (mouse ID C12RL; Figure 4.11). Endpoint was reached immediately after day 5 (tumour ulceration).

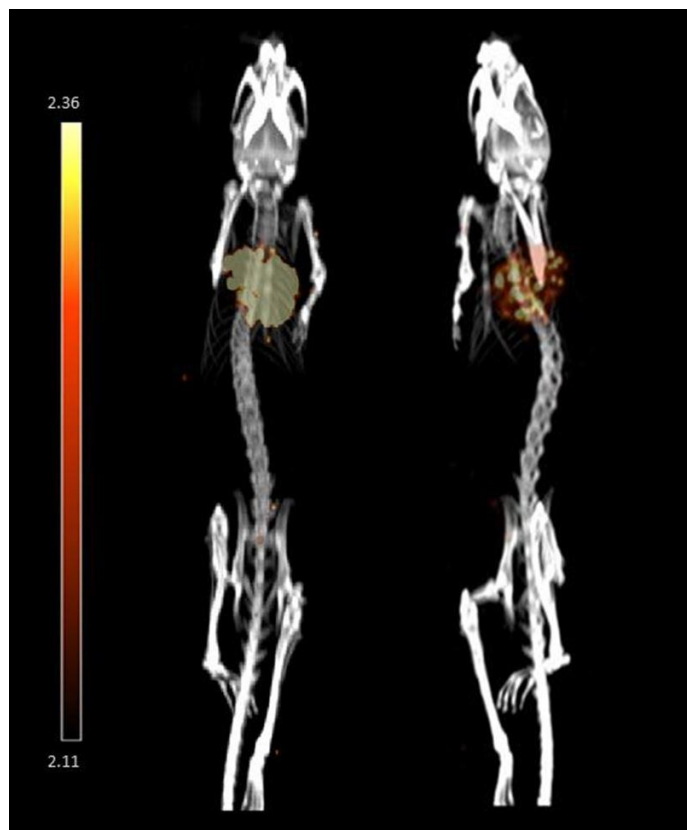


Figure 4.11. SPECT/CT images 3 (left) and 5 (right) days post injection of [^{177}Lu]-PSMA617 and the first dose of OX86 antibody, mouse ID C12RL. Uptake in bladder is low at day 3. Tumour injected in the upper left dorsum; of note is growth of the tumour mass along the upper midback line. Note the pyknotic pattern of tracer uptake at day 5, likely denoting regions of higher and regions of lower target expression within the tumour. Bar: relative voxel intensity scale.

Biodistribution study for mouse C12RL (Figure 4.11) was performed at day 5 post post injection of [^{177}Lu]-PSMA617 and the first dose of OX86 antibody. The tumour uptake after reaching endpoint was 0.85% ID/g.

Table 4.6 lists tumour uptake values in harvested tumours (pre-selected for biodistribution studies) in %ID/g at day 3 and day 9 post injection, in each treatment group.

Harvest timepoint and treatment group	Harvested tumour ID	Tracer uptake <i>ex vivo</i> measurement (in % injected activity per gram tissue)
Day 3 PSMA617+OX86 (Treatment Group #1)	C6L1	1.51
	C8RL	2.93
	C21NP	0.08
Day 3 PSMA617 (Treatment Group #2)	C3L1	0.01
	C15NP	0.02
	C20R1	19.5
Day 9 PSMA617+OX86 (Treatment Group #1)	C8NP	0.1
	C13L1	0
	C19L1	0
Day 9 PSMA617 (Treatment Group #2)	C9R1	0.01
	C15RL	0.03
	C17L1	0.22

Table 4.6. Tumour uptake values in %ID/g at day 3 and day 9 post injection.

A high degree of variability is evident, most evident examples for this are in Treatment Group #2 at day 3 (high uptake in the counted portion of the tumour with the ID C20R1 versus

uptake close to background levels for tumours harvested from animals with IDs C3L1 and C15NP).

4.4. Conclusion

We were able to deliver several interesting observations about the newly established cell line, its behaviour in an immunocompetent model and response to treatments. The initial experimental design aimed at delivering conclusions on the combination treatment, and at objective analysis of outcomes in different treatment arms. By comparing increments in tumour volume between day 0 and day 19/day 20, we were able to show stronger therapeutic potency of the combined treatment, when compared with the targeted radioligand monotherapy.

Second, the initially proposed timeline was based on cells' growth *in vivo*, that was likely facilitated by tumour-supportive microenvironment stemming from NRG mice-derived cells (see Chapter 3 for details), such as fibroblasts, adipocytes etc. However, literature reported longer intervals between inoculation and palpable mass forming [216, 267], which matched the actual timeline of the therapy study.

While tumour growth inhibition graphs, biodistribution studies and SPECT/CT scans showed a high degree of intertumoural heterogeneity, the dynamics of tumour response demonstrated a few facts to conclude:

- the cytotoxic activity (and the antibody dose) delivered was not sufficient to thwart tumour growth, if the initial volume was large, as was the case for tumours C6L1, C9L1 and C20RL in Figures 4.4, 4.5 and Appendix B);

- on the other end of the volume scale, tiny tumours receded early on, with 2 tumours vanishing (tumours C21RL and C7NP in Figures 4.4 and 4.7);
- variability in tracer uptake values was extreme (Table 4.6);
- most importantly, cells did remain non-immunogenic, which was evident from tumours forming *in vivo*, although with delay: and at the same time, PSMA-expressing if tet-induced, although not in all the monitored cases, as was evident from the tracer uptake values (Table 4.6).

Chapter 5: Delineating patterns of tissue response to PSMA617/OX40 therapy

5.1 Introduction

This chapter discusses *ex vivo* pilot experiments using tumours excised during therapy study. The main intent was to deliver high-resolution mapping of tissue response to delivered treatments, by co-registering density and distribution of several different markers.

5.2 Materials and Methods

Materials and methods for this chapter are described in Chapter 2, section 2.11.

5.2.1 *Ex vivo* Studies

For the purpose of characterizing tissue architecture and marker expression (selected markers being mouse IgG2a, Edu, caspase 3, Hoechst 33342, γ -H2AX, CD31 and pimonidazole), a set of co-registration staining and imaging studies was designed as described by *Baker et al.* in [258]: 10 μm tumor cryosections were cut using Cryostar HM560 (Microm International GmbH) cryotome, air-dried and fixed in 50% (v/v) acetone/methanol solution for 10 min at room temperature. The imaging system consisting of two set-ups (*a* and *b*): a robotic fluorescence microscope (axio Imager Z1_a or IIIRS; Zeiss_b), monochrome CCD camera (Retiga 4000R, Qimaging_a; or model 4922, Cohu_b), and a motorized slide loader with x-y stage (Ludl Electronic Products_a), or a custom-built motorized x-y stage_b. Customized (public domain program developed at the NIH) running on G5_a or G3_b Macintosh computers (Apple Computers) allows

for automated tiling of adjacent microscope fields. The resolutions of the entire tumour cryosections of up to 1 cm² surface area were 0.75 µm (for set up a), and 1.0 µm (for set up b) per pixel [258]. In the adapted study protocol, images of expression of 2-4 different markers were amalgamated as composite color images as follows: Hoechst 33342 and anti-CD31; anti-CD31 and pimonidazole; anti-CD31, pimonidazole and EdU; anti-CD31, pimonidazole, EdU and Hoechst 33342; EdU, anti-CD31, and Hoechst 33342; Hoechst 33342, EdU and anti-CD31; Hoechst 33342 and Caspase 3; Hoechst 33342, Caspase 3 and anti-CD31; Hoechst 33342 and γH2AX.

Autoradiography studies of deposited ¹⁷⁷Lu-activity were performed on 16 µm-thick sections, previously cut on a cryostat and placed on a microscope slide, in sets of three sections from different tumours pertaining to the same treatment group and timepoint. The sections were covered with scintillator foil and measured with a dFINE Betaimager (Biospace Lab, Paris, France) for 2 h on BetaIMAGER™ DFine (Biospace Lab, Paris, France). Exposition times varied between 18 and 37 hours.

5.3 Results and Discussion

5.3.1 Autoradiography Studies

During the pilot study, tumours collected at 3 and 9 days post injection were grouped by treatment group and timepoint and betaimaged in triplets, as shown in Figure 5.1:

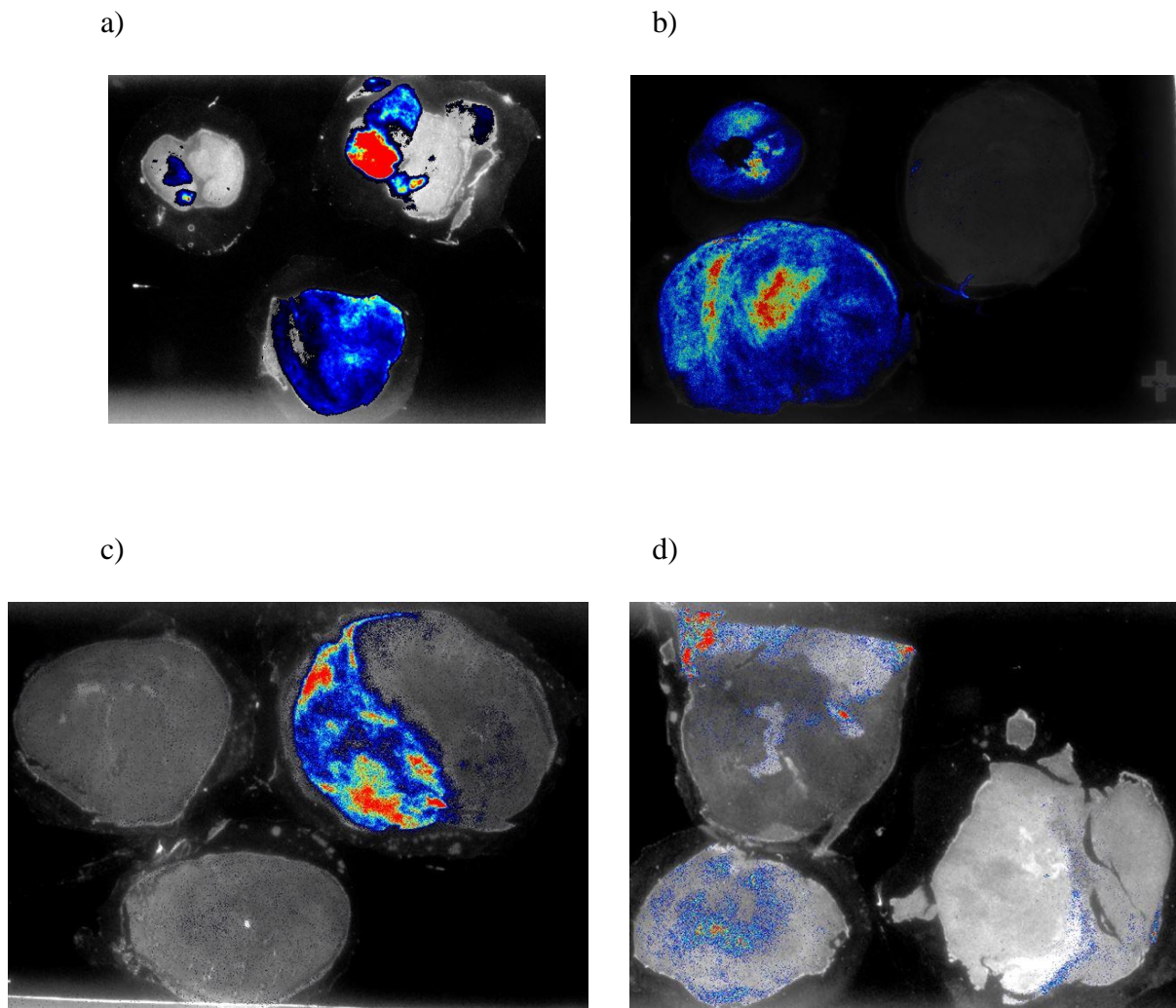


Figure 5.1. Overlaid beta- and optic images of tumour sections in treatment group 1, day 3 after first treatment (a), treatment group 2, day 3 after treatment (b), treatment group 1, day 9 after first treatment (c), treatment group 2, day 9 after treatment (d). Exposition time: 18-37 hours.

In each treatment group, betaimages revealed a significant degree of intertumoural heterogeneity. For example, in treatment group 2, day 3 (Figure 5.1-b), while the excised tumour's section ID C15NP (top right) showed near-background activity, a homogeneously

distributed uptake pattern was visualized for ID C3L1 (bottom left). We were able to conclude that there were other variables involved besides the treatment group and timepoint.

Examples of intratumoural heterogeneity in tracer uptake patterns were most pronounced for tumour ID C8RL (Figure 5.1-a, top right) and C8NP (Figure 5.1-c, top right). Of note is that 3 out of 12 imaged sections showed activity uptake near background levels: C15NP (Figure 5.1-b, top right), C19L1 (Figure 5.1-c, top left), and C13L1 (Figure 5.1-c, bottom).

We speculated that the most likely cause of the heterogeneous uptake pattern is due to non-uniform PSMA-expression in tissue. Other potential explanations were different degrees of vascularization and perfusion, presence of necrotic/apoptotic microregions resulting in tissue hypoxia. The next set of pilot experiments was aimed at elucidating precisely these tissue characteristics.

5.3.2 Tissue marker registration – Antibody- and click-chemistry staining and fluorescence microscopy

In the pilot study, overlaid images of multiparametric tissue imaging revealed further patterns of tissue marker expression. The pilot study was limited to delineating expression of: Hoechst 33342 (DNA– perfusion and viability), caspase 3 (apoptosis), EdU (proliferation marker), CD31 (endothelial cells marker), pimonidazole (hypoxia) and γ H2AX (DNA double strand breaks).

5.3.3 Co-registration and interpretation

Co-registration of up to 4 different markers resulted in characterizing the excised TRAMP-C2 tissue as viable, well perfused, highly proliferating, and highly vascularized (possibly with convoluted vessels and non-unidirectional bloodflow), with varying degrees of microregional apoptotic and tissue damage density. Presence of artifacts (not shown) and the small sample size in the pilot study limited the scope of the results for Aim 2, sub-aim b. The results were not quantified in the pilot study. Figures 5.2 - 5.4 show examples of tissue sections' fluorescence microscopy images.

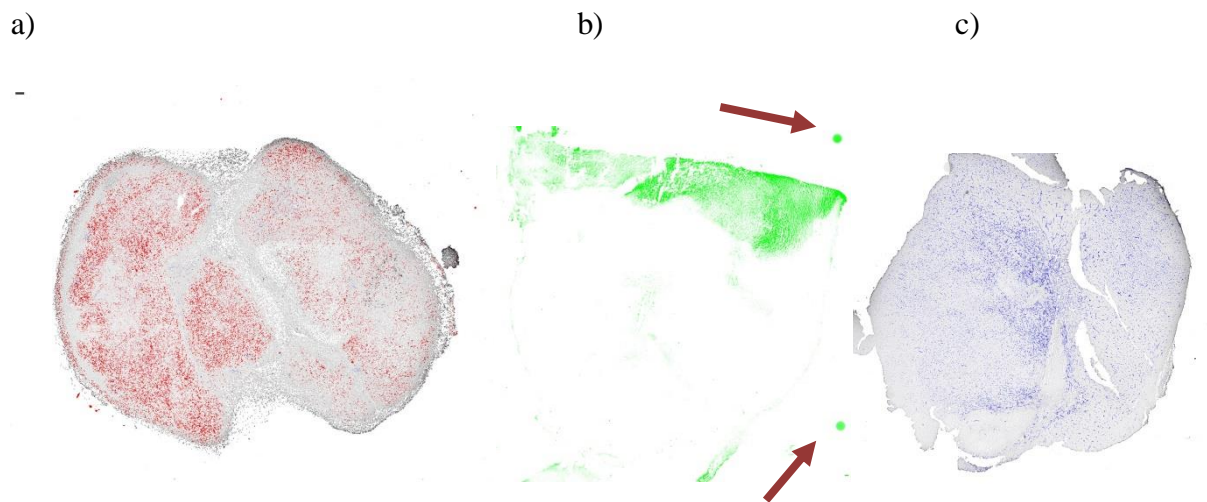
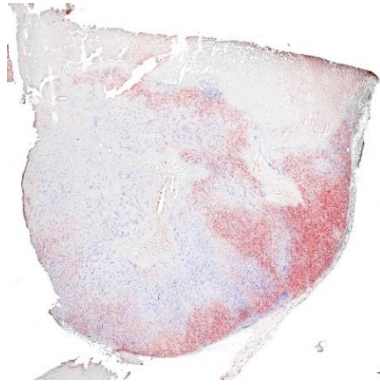


Figure 5.2. Fluorescence microscopy registration/co-registration of markers of proliferation, viability, perfusion and vascularization. a) tumour ID C21NP - Treatment Group 1, day 3; b) tumour ID C17L1 – Treatment Group 2, day 9; c) tumour ID C9R1 – Treatment Group 2, day 9. Red – EdU, green – pimonidazole, blue – CD31, grey- Hoechst 33342, arrows - artifacts.

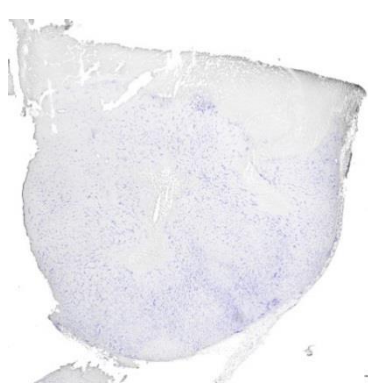
a)



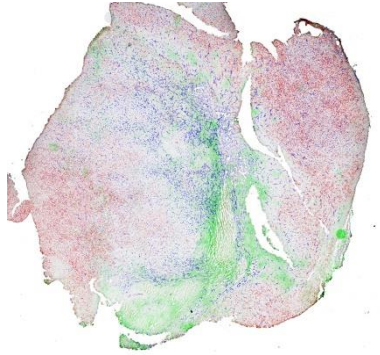
b)



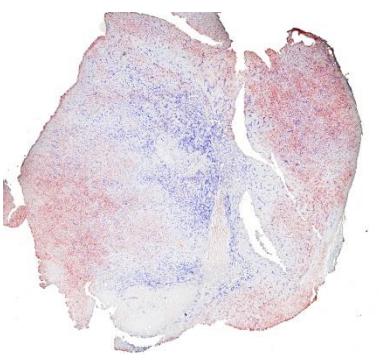
c)



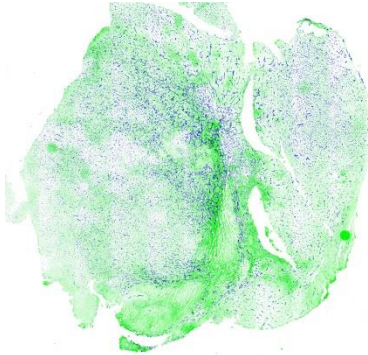
d)



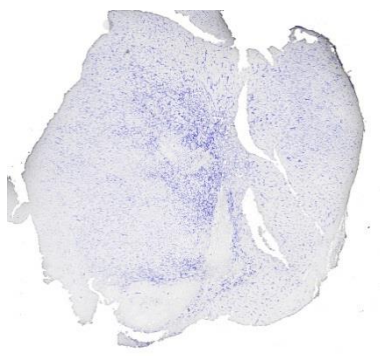
e)



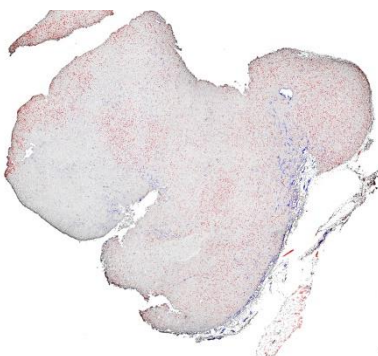
f)



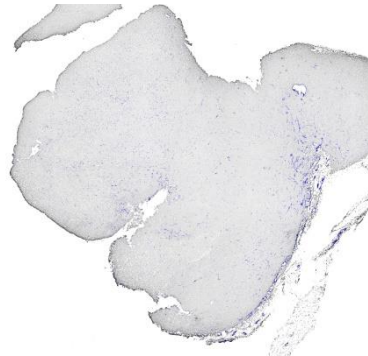
g)



h)



i)



(continues on next page)

j)

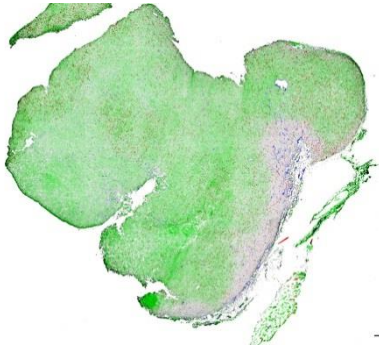


Figure 5.3. Fluorescence microscopy co-registration of 2-4 different markers of proliferation, viability, perfusion and vascularization. a-c) tumour ID C17L1 - Treatment Group 2, day 9; d-g) tumour ID C9R1 – Treatment Group 2, day 9; g-j) tumour ID C8RL Treatment Group 1, day 3. Red – EdU, green – pimonidazole, blue –CD31, grey- Hoechst 33342.

a)



b)



(continues on next page)

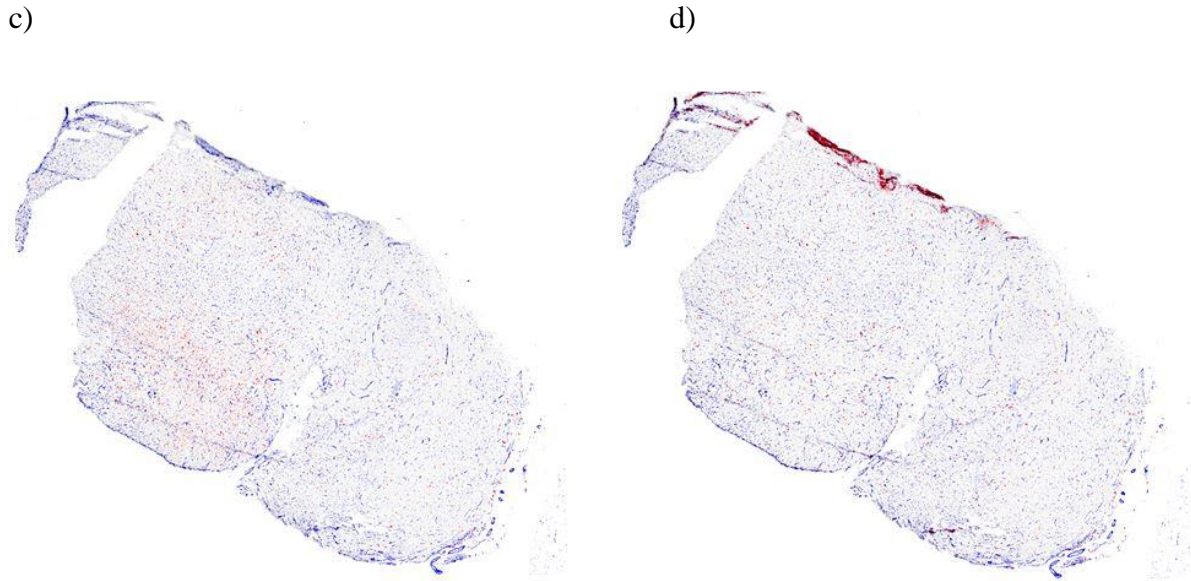


Figure 5.4. Fluorescence microscopy images of a section of tumour ID C8RL; a) grey – Hoechst 33342, red – γ H2AX; b) grey – Hoechst 33342, red – caspase 3; c) grey – Hoechst 33342, red – γ H2AX, blue – CD31; d) grey – Hoechst 33342, red – caspase 3, blue – CD31. This section was not betaimaged.

Figure 5.3 is best used for assessing intratumoral heterogeneity, e.g. by comparing figures 5.3.b), d) and g) – tumors show areas of varying marker expression for vasculature and proliferation. Images a-c, d-f and g-j in Figure 5.3 are registered on slices from three different tumours. Images g-j are registered on a different slice from the same tumour as in Figure 5.4.

In combination with the data from FACS, betaimaging and biodistribution studies etc., we were not able to assess impact of different treatments on tissue architecture. The principal findings of all the experiments in Chapter 5 speak for non-uniformity of the tumour phenotype. Similar to the data in the flow cytometry studies (Appendix C) and the betaimages (Figure 5.1),

both within each tumour section and within treatment groups, the fluorescence staining images confirmed varying levels of: proliferation (Figures 5.2-a, 5.3-a, b, d, and e), tissue viability (5.2-a, f and 5.3-h), hypoxia (figures 5.2-b, 5.3-b, d, f and j), vascularization (Figures 5.2-c, 5.3-a and c-g) and DNA damage (Figure 5.4-a). In addition, the small sample size did not allow for quantification of the results for Aim 2b. Although, as mentioned at the beginning of this subchapter, general conclusions could be made on the tumour tissue characteristics, it should be noted that these conclusions were based on limited sample size. Furthermore, the impact of the treatments on the marker expression could not be assessed, meaning that the goal of Aim 2-b was not fully reached in the pilot study. However, precisely the non-uniformity in fluorescence microscopy reaffirmed the conclusion from previous chapters – namely that the clone 16 – subclone Q13 TRAMP-C2 cells did not form homogeneous tissues *in vivo*.

In addition, when tumour uptake values from biodistribution studies (Table 4.1) were incorporated into the analysis, a high degree of variability of tracer accumulation in tissue was evident.

One observation to add is that Treatment Group 2 did show different patterns of TIL-infiltration, as can be seen in Appendix C.

Chapter 6: Conclusion and Future Directions

6.1 Results Summary

The experimental design in this thesis relied on commonly reported success of combination treatments in oncology. The principal aim was to determine potential advantages of [¹⁷⁷Lu]Lu-PSMA617 and anti-OX40 as a combination treatment of metastatic prostate cancer. In particular, we expected a favourable therapeutic efficiency based on abscopal effect.

Our first aim - to validate inducible TRAMP-C2 cell clones – was completed with clear, quantifiable results. We confirmed that all the parental clones provided to us were suitable for proceeding with in animal experiments. Proof of induction *in vivo* was reached as visualization in PET/CT and supported by *ex vivo* uptake distribution data. Significant uptake increase post induction directly confirmed the application potential of this model as a reporter gene tool. In addition to previously published use of human PSMA as a reporter gene for monitoring T-cells and adenoviral infection, our results support expanding its application to a murine prostate cancer cell line. In addition, we propose our model as a less intricate and time-consuming method, compared to the reported CAR-T approach [185].

Next, a large-scale therapy study was initiated, however its completion was delayed, and its scope reduced, due to the unexpectedly prolonged tumour growth rates. Here it is worth mentioning that the members of the project team agreed that the therapy experiment, done in two passes, was a pilot experiment before a potential expansion in the future. The fact that tumours proliferated with reduced speed after either of the treatments supports further use of similar models to study PCa therapy in a pre-clinical setting. The proof of superior efficiency is evident from Figures 4.4-4.7 and Appendix B, when the treatment groups #1 and #2 are compared with

the control group (Figure 4.1), and the proof of superior efficiency of the combination treatment versus the targeted radioligand therapy was evident from the statistical analysis. Moreover, we found encouraging that the patterns of tumour growth inhibition were in concordance with reported phases of TIL-infiltration patterns, due to abscopal effect. Therefore, much can be built upon the pilot results reported herein, in terms of the use of the described model for studies of endoradiotherapy in combination with immunotherapy in cancer. Comparing the treatment efficiency between the treatment arms #1 and #2 did deliver statistically significant differences, and this can possibly later be confirmed with higher certainty with verified stable PSMA-expressing clone.

Ultimately, a multi-parametric pilot study of microscopic tissue response to therapy elucidated both the advantages and the disadvantages of the used model. It is concluded that the formed tumour mass mimicks aggressive, highly proliferating prostate cancer tissue. Nevertheless, without further isolating and validating populations of cells that, once inoculated, would stably express equally high levels of PSMA, clones used in this study could possibly generate variable results.

6.2 Future Directions

A repetition of the therapy study was anticipated before the completion of this thesis. Results of such a study would increase sample size, add value to the reported results, and possibly aid in delivering useful information on the proposed combination therapy.

As previously mentioned, the timeline of the experiments had to be adapted multiple times due to slow, non-uniform rates of tumours starting to form *in vivo*. For this reason, a large-scale study could rather be completed if several identical sets of experiments for small sample sizes can be planned, and executed using only those tumour volumes that fall into a predefined range, e.g. tumours with volume between 200 and 500 mm³. Randomly assigning tumours to each treatment arm would certainly add to results' plausibility, however, it might additionally extend the time needed to complete the experiments.

For Aim 2, sub-aim b, a multitude of potential objectives can be decided on in order to assess impact of treatment on tumour tissue behaviour. To name a few example objectives, future studies can be directed at:

- Degree of radiation damage resulting from PSMA617 and its location relative to perfused vasculature
- Degree of proliferation inhibition (EdU) & cell death (caspase 3) resulting from PSMA617 versus from combination treatments
- Distribution of OX86 (using secondary antibody label) relative to perfused vessels (CD31/Hoechst 33342/pimonidazole)
- Impact of combination treatments (vs. single agents) on distribution of activity uptake/OX86 accumulation in tissue.

These, and further potential objectives, would require multiple times the number of tumour samples used in the pilot study.

Prior to scheduling another large-scale therapy study, isolating a reliable subclone would most likely be achieved with multiple FACS study repeats using candidate subclones,

PET/CT images, biodistribution and autoradiography studies. Once a clonal population with stable, high PSMA-expression is identified, it can be propagated in large amounts for first round of inoculation. Due to possible reduction, or loss, of expression, clones should be tested per flow cytometry repeatedly throughout the study, to confirm stable induction of expression.

6.3 Concluding Remarks

In this thesis, we evaluated a combination therapy strategy, consisting of a targeted radioligand [¹⁷⁷Lu]Lu-PSMA617 and an immunotherapeutic agonist OX86. We hypothesized that the combination therapy will outperform monotherapies with either [¹⁷⁷Lu]Lu-PSMA617 or OX86 alone, in a pre-clinical model. As it appears from the results reported herein, we were able to affirm the hypothesis – the tumour growth inhibiting potential of the combined treatment was significantly higher ($p < 0.05$). Within both treatment groups, however, a varying response to treatment was visualized, likely owing to the, varying degree of radiopharmaceutical uptake, as discussed in Chapter 5. Therefore, it would be useful to compare therapeutic potency between the treatment groups by using a reliable PSMA-expressing clone in the future. . However, the inducible cell line we used as a model of disease showed high radiotracer uptake after induction with doxycycline, signifying adequacy of this model for the purpose of gene expression reporting.

Bibliography

1. World Health Organization (2020, February 26th). Cancer - Key Facts. Retrieved from <https://www.who.int/news-room/fact-sheets/detail/cancer>.
2. World Health Organization - International Agency for Research on Cancer (2020, February 26th). Online Analysis Map. Retrieved from <http://gco.iarc.fr/today/online-analysis-map?projection=globe>.
3. Ferlay J *et al.* GLOBOCAN 2012 v1.0, Cancer Incidence and Mortality Worldwide: IARC CancerBase No. 11. International Agency for Research on Cancer; 2013.
4. Canadian Cancer Society, Statistics Canada, the Public Health Agency of Canada (2020, February 26th). Canadian Cancer Statistics 2019. Retrieved from <https://www.cancer.ca/~media/cancer.ca/CW/cancer%20information/cancer%20101/Canadian%20cancer%20statistics/Canadian-Cancer-Statistics-2019-EN.pdf?la=en>.
5. DeBlanc AG *et al.* (2020, February 26th). Recent trends in prostate cancer in Canada. Retrieved from <https://www150.statcan.gc.ca/n1/en/pub/82-003-x/2019004/article/00002-eng.pdf?st=IFkEFew8>.

6. Saad F *et al.* 2019 Canadian Urological Association (CUA) - Canadian Uro Oncology Group (CUOG) guideline: Management of castration-resistant prostate cancer (CRPC). *Can Urol Assoc J.* **2019**; 13(10): 307-314.

7. American Cancer Society (2020, March 12th). Prostate Cancer Risk Factors. Retrieved from <https://www.cancer.org/cancer/prostate-cancer/causes-risks-prevention/risk-factors.html>.

8. Gann PH. Risk factors for prostate cancer. *Rev Urol.* **2002**;4 Suppl 5(Suppl 5):S3-S10.

9. Dickinson J *et al.* Trends in prostate cancer incidence and mortality in Canada during the era of prostate-specific antigen screening. *CMAJ Open.* **2016**;4(1): E73-E79.

10. Keyes M *et al.* Treatment options for localized prostate cancer. *Can. Fam. Phys. Med. Fam. Can.* **2013**;59: 1269-1274.

11. Dai C *et al.* Androgen signaling in prostate cancer. *Cold Spring Harb. Perspect. Med.* **2017**;7: a030452.

12. Yap TA *et al.* Drug discovery in advanced prostate cancer: Translating biology into therapy. *Nat Rev Drug Discov.* **2016**;15: 699-718.

13. Sureka SK *et al.* Predictors for progression of metastatic prostate cancer to castration-resistant prostate cancer in Indians. *Indian J Med Res.* **2016**; 143(Supplement): S68-S73.
14. Drake CG *et al.* Metastatic castration-resistant prostate cancer: new therapies, novel combination strategies and implications for immunotherapy. *Oncogene.* **2014**(33): 5053-5064.
15. So I *et al.* Canadian Urological Association-Canadian Urologic Oncology Group guideline on metastatic castration-naïve and castration-sensitive prostate cancer. *Can Urol Assoc J.* **2020**;14(2): 17-23.
16. Gulley JL, Drake CG. Immunotherapy for prostate cancer: recent advances, lessons learned, and areas for further research. *Clin Cancer Res.* **2011**;17(12): 3884-3891.
17. Tsao CK *et al.* Overcoming castration resistance in prostate cancer. *Curr Opin Urol.* **2012**;22(3): 167-174.
18. Liu HH *et al.* Evolving Personalized Therapy for Castration-Resistant Prostate Cancer. *Biomedicine.* **2014**; 4: 2.

19. Laverdière J *et al.* Beneficial effect of combination hormonal therapy administered prior and following external beam radiation therapy in localized prostate cancer. *International Journal of Radiation Oncology*Biology*Physics*; **1997**;37(2): 247-252.
20. James ND *et al.* Abiraterone for prostate cancer not previously treated with hormone therapy. *N Engl J Med* **2017** Jun 3; [e-pub].
21. Fizazi K *et al.* Abiraterone plus prednisone in metastatic, castration-sensitive prostate cancer. *N Engl J Med* **2017** Jun 4; [e-pub].
22. Smith MD *et al.* Addition of radium-223 to abiraterone acetate and prednisone or prednisolone in patients with castration-resistant prostate cancer and bone metastases (ERA 223): a randomised, double-blind, placebo-controlled, phase 3 trial. *Lancet Oncol.* **2019**;20(3): 408-419.
23. Spratt DE *et al.* Androgen receptor upregulation mediates radioresistance after ionizing radiation. *Cancer research.* **2015**;75(22): 4688-4696.
24. Logothetis CJ *et al.* Effect of abiraterone acetate and prednisone compared with placebo and prednisone on pain control and skeletal-related events in patients with metastatic castration-resistant prostate cancer: exploratory analysis of data from the COU-AA-301 randomised trial. *Lancet Oncology*; **2012**;13(12): 1210-1217.

25. Ton FN *et al.* Effects of low-dose prednisone on bone metabolism. *Journal of bone and mineral research*; **2004**;20(3): 464-470.
26. Saad F *et al.* Radium-223 and concomitant therapies in patients with metastatic castration-resistant prostate cancer: an international, early access, open-label, single-arm phase 3b trial. *Lancet Oncology*; **2016**;17(9): 1306-1316.
27. Liss AL *et al.* Combination therapy improves prostate cancer survival for patients with potentially lethal prostate cancer: The impact of Gleason pattern 5. *Brachytherapy*; **2015**;14(4): 502-510.
28. Jadvar H *et al.* Radiotheranostics in Cancer Diagnosis and Management. *Radiology*. **2018**;286(2): 388-400.
29. Lee DY, Li KC. Molecular theranostics: a primer for the imaging professional. *AJR Am J Roentgenol*. **2011**;197(2): 318-324.
30. Thompson MK *et al.* Practice-changing radiation therapy trials for the treatment of cancer: where are we 150 years after the birth of Marie Curie?. *Br J Cancer*. **2018**;119(4): 389-407.
31. Bagheri R *et al.* Study of Bone Surface Absorbed Dose in Treatment of Bone Metastases via Selected Radiopharmaceuticals: Using MCNP4C Code and Available Experimental Data. *Cancer biotherapy & radiopharmaceuticals*. **2015**;30(4): 174-181.

32. Okoye N *et al.* Chelators and metal complex stability for radiopharmaceutical applications. *Radiochimica Acta*; **2019**;107(9-11): 1087-1120.
33. Wadas TJ *et al.* Coordinating radiometals of copper, gallium, indium, yttrium, and zirconium for PET and SPECT imaging of disease. *Chem Rev.* **2010**;110(5): 2858-2902.
34. Czarniecki M *et al.* Keeping up with the prostate-specific membrane antigens (PSMAs): an introduction to a new class of positron emission tomography (PET) imaging agents. *Transl Androl Urol.* **2018**;7(5): 831-843.
35. Gallamini A *et al.* Positron Emission Tomography (PET) in Oncology. *Cancers (Basel).* **2014**;6(4): 1821-1889.
36. Vaquero JJ, Kinahan P. Positron Emission Tomography: Current Challenges and Opportunities for Technological Advances in Clinical and Preclinical Imaging Systems. *Annu Rev Biomed Eng.* **2015**;17: 385-414.
37. Chakravarty R *et al.* Positron emission tomography image-guided drug delivery: current status and future perspectives. *Mol Pharm.* **2014**;11(11): 3777-3797.
38. Israel O *et al.* Two decades of SPECT/CT - the coming of age of a technology: An updated review of literature evidence. *Eur J Nucl Med Mol Imaging.* **2019**;46(10): 1990-2012.

39. Virgolini I *et al.* Current status of theranostics in prostate cancer. *Eur J Nucl Med Mol Imaging.* **2018**;45(3): 471-495.
40. Rowe SP *et al.* Prostate-Specific Membrane Antigen-Targeted Radiohalogenated PET and Therapeutic Agents for Prostate Cancer. *J Nucl Med.* 2016;57(Suppl 3): 90S-96S.
41. Jadvar H. Targeted Radionuclide Therapy: An Evolution Toward Precision Cancer Treatment [published correction appears in *AJR Am J Roentgenol.* **2017**;209(4): 949]. *AJR Am J Roentgenol.* 2017;209(2): 277-288.
42. Kiess AP *et al.* Prostate-specific membrane antigen as a target for cancer imaging and therapy. *Q J Nucl Med Mol Imaging.* **2015**;59(3): 241-268.
43. Weineisen M *et al.* ^{68}Ga - and ^{177}Lu -Labeled PSMA I&T: Optimization of a PSMA-Targeted Theranostic Concept and First Proof-of-Concept Human Studies. *J Nucl Med;* **2015**;56(8): 1169-1176.
44. Song H, Sgouros G. Radioimmunotherapy of solid tumors: searching for the right target. *Curr Drug Deliv.* **2011**;8(1): 26-44.
45. Frost SH *et al.* Comparative efficacy of ^{177}Lu and ^{90}Y for anti-CD20 pretargeted radioimmunotherapy in murine lymphoma xenograft models. *PLoS One.* **2015**;10(3): e0120561.

46. Orcutt KD *et al.* Effect of small-molecule-binding affinity on tumor uptake in vivo: a systematic study using a pretargeted bispecific antibody. *Mol Cancer Ther.* **2012**;11(6): 1365-1372.
47. Wright CL *et al.* Theranostic Imaging of Yttrium-90. *Biomed Res Int.* **2015**;2015: 481279.
48. Bouchelouche K *et al.* PET/CT Imaging and Radioimmunotherapy of Prostate Cancer. *Semin Nucl Med.* **2011**;41(1): 29-44.
49. Carlsson J *et al.* Tumour therapy with radionuclides: assessment of progress and problems. *Radiotherapy and Oncology.* **2003**;66(2): 107-117
50. Ballinger JR. Theranostic radiopharmaceuticals: established agents in current use. *Br J Radiol.* **2018**;91(1091): 20170969.
51. Sikkandhar MG *et al.* Theranostic Probes for Targeting Tumor Microenvironment: An Overview. *Int J Mol Sci.* **2017**;18(5): 1036.
52. Kulkarni HR *et al.* Theranostics of prostate cancer: from molecular imaging to precision molecular radiotherapy targeting the prostate specific membrane antigen. *Br J Radiol.* **2018**;91(1091): 20180308.

53. Chang SS. Overview of prostate-specific membrane antigen. *Rev Urol.* **2004**;6 Suppl 10(Suppl 10): S13-S18.
54. Bouchelouche K *et al.* Positron emission tomography/computed tomography and radioimmunotherapy of prostate cancer. *Curr Opin Oncol.* **2009**;21: 469-474.
55. Bouchelouche K *et al.* Prostate specific membrane antigen- a target for imaging and therapy with radionuclides. *Discov Med.* 2010;9(44): 55-61.
56. Baum RP *et al.* ¹⁷⁷Lu-labeled prostate-specific membrane antigen radioligand therapy of metastatic castration-resistant prostate cancer: safety and efficacy. *J Nucl Med*; **2016**;57: 1006-1013.
57. von Eyben FE *et al.* Third-line treatment and ¹⁷⁷Lu-PSMA radioligand therapy of metastatic castration-resistant prostate cancer: a systematic review. *Eur J Nucl Med Mol Imaging.* **2018**;45: 496-508.
58. Eisenhauer EA *et al.* New response evaluation criteria in solid tumours: revised RECIST guideline (version 1.1). *Eur J Cancer*; **2009**; 45: 228-247.
59. Young H *et al.* Measurement of clinical and subclinical tumour response using [¹⁸F]fluorodeoxyglucose and positron emission tomography: review and 1999 EORTC

recommendations. European Organization for Research and Treatment of Cancer (EORTC) PET Study Group. *Eur J Cancer*.**1999**;35: 1773-1782.

60. Langbein T *et al.* Salivary gland toxicity of PSMA radioligand therapy: relevance and preventive strategies. *J Nucl Med*. **2018**; 59: 1172-1173.

61. Barbet J *et al.* Radiolabeled Antibodies for Cancer Imaging and Therapy. *Methods in molecular biology (Clifton, N.J.)*;**2012**; 907: 681-697.

62. Chatalic KL *et al.* Towards personalized treatment of prostate cancer: PSMA I&T, a promising prostate-specific membrane antigen-targeted theranostic agent. *Theranostics*;**2016**;6: 849-861.

63. Yordanova A *et al.* Theranostics in nuclear medicine practice. *Onco Targets Ther*;**2017**;10: 4821-4828.

64. Baum RP, Kulkarni HR. THERANOSTICS: from molecular imaging using Ga-68 labeled tracers and PET/CT to personalized radionuclide therapy - the Bad Berka experience. *Theranostics*;**2012**;2(5): 437-447.

65. Ferdinandus J *et al.* Prostate-specific membrane antigen theranostics: Therapy with lutetium-177. *Curr. Opin. Urol*;**2018**;28: 197-204.

66. Braat A, Ahmadzadehfar H. Lutetium-177 labelled PSMA ligands for the treatment of metastatic castrate-resistant prostate cancer. *Tijdschr Nucl Geneesk.* **2016**;38: 1627-1634.
67. Pillai AM, Knapp FF Jr. Lutetium-177 labeled therapeutics: ¹⁷⁷Lu-PSMA is set to redefine prostate cancer treatment. *Curr Radiopharm;* **2016**;9: 6-7.
68. Emmett L *et al.* Lutetium ¹⁷⁷ PSMA radionuclide therapy for men with prostate cancer: a review of the current literature and discussion of practical aspects of therapy. *J Med Radiat Sci.* **2017**;64(1): 52-60.
69. Carter RE *et al.* Prostate-specific membrane antigen is a hydrolase with substrate and pharmacologic characteristics of a neuropeptidase. *Proc Natl Acad Sci U S A;* **1996**;93: 749-753.
70. Ross JS *et al.* Correlation of primary tumor prostate-specific membrane antigen expression with disease recurrence in prostate cancer. *Clin Cancer Res.* **2003**;9: 6357-6362.
71. Pinto JT *et al.* Prostate-specific membrane antigen: a novel folate hydrolase in human prostatic carcinoma cells. *Clin Cancer Res.* **1996**;2: 1445-1451.
72. Silver DA *et al.* Prostate-specific membrane antigen expression in normal and malignant human tissues. *Clin Cancer Res.* **1997**;3: 81-85.

73. Troyer JK *et al.* Detection and characterization of the prostate-specific membrane antigen (PSMA) in tissue extracts and body fluids. *Int J Cancer*. **1995**;62: 552-558.
74. Bařinka, C *et al.* Glutamate carboxypeptidase II in diagnosis and treatment of neurologic disorders and prostate cancer. *Curr. Med. Chem.* **2012**, (19), 856-870.
75. Evans JC *et al.* The therapeutic and diagnostic potential of the prostate specific membrane antigen/glutamate carboxypeptidase II (PSMA/GCPII) in cancer and neurological disease. *Br J Pharmacol.* **2016**;173(21): 3041-3079.
76. Wright GL, Jr, Haley C, Beckett ML, Schellhammer PF. Expression of prostate-specific membrane antigen in normal, benign, and malignant prostate tissues. *Urol Oncol.* **1995**;1: 18-28.
77. Silver DA *et al.* Prostate-specific membrane antigen expression in normal and malignant human tissues. *Clin Cancer Res.* **1997**;3(1): 81-85.
78. Heston WDW. Bedeutung des prostataspezifischen Membranantigens (PSMA) Eine Neurocarboxypeptidase und Membran-Folat-Hydrolase. *Der Urologe A.* **1996**;35(5): 400-407.
79. Wright GL *et al.* Upregulation of prostate-specific membrane antigen after androgen-deprivation therapy. *Urology*; **1996**;48(2): 326-334.

80. Ahmadzadehfar H *et al.* ^{68}Ga -PSMA-11 PET as a Gatekeeper for the Treatment of Metastatic Prostate Cancer with ^{223}Ra : Proof of Concept. *J Nucl Med.* **2017**;58: 438-444.
81. Afshar-Oromieh A *et al.* Radiation dosimetry of ^{68}Ga -PSMA-11 (HBED-CC) and preliminary evaluation of optimal imaging timing. *Eur J Nucl Med Mol Imaging.* **2016**;43(9): 1611-1620.
82. Afshar-Oromieh A *et al.* Diagnostic performance of ^{68}Ga -PSMA-11 (HBED-CC) PET/CT in patients with recurrent prostate cancer: evaluation in 1007 patients. *Eur J Nucl Med Mol Imaging.* **2017**;44(8): 1258-1268.
83. Schwenck J *et al.* Comparison of ^{68}Ga -labelled PSMA-11 and ^{11}C -choline in the detection of prostate cancer metastases by PET/CT. *Eur J Nucl Med Mol Imaging.* **2017**;44(1): 92-101.
84. Sterzing F *et al.* Ga-PSMA-11 PET/CT: a new technique with high potential for the radiotherapeutic management of prostate cancer patients. *Eur J Nucl Med Mol Imaging.* **2015**;43(1): 34-41.
85. Chang SS *et al.* Five different anti-prostate-specific membrane antigen (PSMA) antibodies confirm PSMA expression in tumor-associated neovasculature. *Cancer Res.* **1999**;59(3): 192-198.
86. Maurer T *et al.* Current use of PSMA-PET in prostate cancer management. *Nat Rev Urol.* **2016**;13: 226-235.

87. Bluemel C *et al.* ^{68}Ga -PSMA-PET/CT in patients with biochemical prostate cancer recurrence and negative ^{18}F -Choline-PET/CT. *Clin Nucl Med.* **2016**;41: 515-521.
88. Maurer T *et al.* Diagnostic efficacy of ^{68}Ga -PSMA-PET compared to conventional imaging in lymph node staging of 130 consecutive patients with intermediate to high-risk prostate cancer. *J Urol.* **2015**;195: 1436-1443.
89. Deitlein M *et al.* Comparison of [^{18}F]DCFPyL and [^{68}Ga]Ga-PSMA-HBED-CC for PSMA-PET in patients with relapsed prostate cancer. *Mol Imaging Biol.* **2015**;17: 575-584.
90. Mottet N *et al.* Members of the EAU - ESTRO - ESUR -SIOG Prostate Cancer Guidelines Panel. EAU - ESTRO - ESUR - SIOG Guidelines on Prostate Cancer. Edn. presented at the EAU Annual Congress Copenhagen 2018. 978-94-92671-02-8. Publisher: EAU Guidelines Office. Arnhem, The Netherlands, 2018.
91. Bodei L *et al.* Long-term evaluation of renal toxicity after peptide receptor radionuclide therapy with ^{90}Y -DOTATOC and ^{177}Lu -DOTATATE: The role of associated risk factors. *Eur J Nucl Med Mol Imaging* **2008**;35: 1847-1856.

92. Cremonesi, M. Correlation of dose with toxicity and tumour response to ⁹⁰Y- and ¹⁷⁷Lu-PRRT provides the basis for optimization through individualized treatment planning. *European Journal of Nuclear Medicine and Molecular Imaging*. **2018**;45(13): 2426-2441.
93. Kwekkeboom DJ *et al.* Overview of results of peptide receptor radionuclide therapy with 3 radiolabeled somatostatin analogs. *J Nucl Med*; **2005**;46(Suppl 1): 62S-66S.
94. Liu HH *et al.* Constitutive and antibody-induced internalization of prostate-specific membrane antigen. *Cancer Res*. **1998**;58: 4055-4060.
95. Wüstemann T *et al.* Design of Internalizing PSMA-specific Glu-ureido-based Radiotherapeutics. *Theranostics*; **2016**;6(8): 1085-1095.
96. Rajasekaran SA. A Novel Cytoplasmic Tail MXXXL Motif Mediates the Internalization of Prostate-specific Membrane Antigen. *Molecular Biology of the Cell*; **2003**;14(12): 4835-4845.
97. Ghosh A, Heston WD (2005a). Understanding prostate-specific membrane antigen and its implication in prostate cancer In: LaRochelle WJ; Shimkets RA, editor. (eds). *The Oncogenomics Handbook*. Springer: Totowa, NJ, pp. 597-615.

98. Rahbar K *et al.* Response and tolerability of a single dose of ^{177}Lu -PSMA-617 in patients with metastatic castration-resistant prostate cancer: a multicenter retrospective analysis. *J Nucl Med.* 2016;57:1334-1338.
99. Fendler WP *et al.* Preliminary experience with dosimetry, response and patient reported outcome after [^{177}Lu]-PSMA-617 therapy for metastatic castration-resistant prostate cancer. *Oncotarget.* **2017**;8: 3581-3590.
100. Yadav MP *et al.* [^{177}Lu]-DKFZ-PSMA-617 therapy in metastatic castration resistant prostate cancer: safety, efficacy, and quality of life assessment. *Eur J Nucl Med Mol Imaging.* **2017**;44: 81-91.
101. Ruigrok EAM *et al.* The Future of PSMA-Targeted Radionuclide Therapy: An Overview of Recent Preclinical Research. *Pharmaceutics*; **2019**;11(11): 560.
102. Gourni E, Henriksen G. Metal-Based PSMA Radioligands. *Molecules*; **2017**;22(4): 523.
103. Kwon H *et al.* Recent progress on PSMA-targeted radionuclide probes for Imaging and therapy of prostate cancer. *Asian Journal of Organic Chemistry*; **2019**.
104. Rahbar K *et al.* PSMA targeted radioligand therapy in metastatic castration resistant prostate cancer after chemotherapy, abiraterone and/or enzalutamide. A retrospective analysis of overall survival. *Eur J Nucl Med Mol Imaging.* **2018**;45(1): 12-19.

105. Hofman MS *et al.* [^{177}Lu]-PSMA-617 radionuclide treatment in patients with metastatic castration-resistant prostate cancer (LuPSMA trial): a single-centre, single-arm, phase 2 study. *The Lancet Oncology*; **2018**;19(6): 825-833.
106. Yordanova A *et al.* The impact of repeated cycles of radioligand therapy using [^{177}Lu] Lu-PSMA-617 on renal function in patients with hormone refractory metastatic prostate cancer. *Eur J Nucl Med Mol Imaging*. **2017**;44: 1473-1479.
107. Yordanova A *et al.* Outcome and safety of rechallenge [^{177}Lu]Lu-PSMA-617 in patients with metastatic prostate cancer. *European Journal of Nuclear Medicine and Molecular Imaging*; **2018**; 46(5):1073-1080.
108. Rathke H *et al.* Repeated (^{177}Lu)-labeled PSMA-617 Radioligand therapy using treatment activities of up to 9.3 GBq. *J Nucl Med*. **2018**;59: 459-465.
109. Awang ZH *et al.* Radioligand therapy of metastatic castration-resistant prostate cancer: current approaches. *Radiat Oncol*. **2018**;13(1):98.
110. Kratochwil C *et al.* Targeted α -Therapy of Metastatic Castration-Resistant Prostate Cancer with ^{225}Ac -PSMA-617: Swimmer-Plot Analysis Suggests Efficacy Regarding Duration of Tumor Control. *Journal of Nuclear Medicine*; **2018**;59(5): 795-802.

111. von Eyben F *et al.* [¹⁷⁷Lu]-PSMA radioligand therapy of predominant lymph node metastatic prostate cancer. *Oncotarget*. **2019**;10: 2451-2461.

112. Rasul S *et al.* Clinical outcome of standardized [¹⁷⁷Lu]-PSMA-617 therapy in metastatic prostate cancer patients receiving 7400 MBq every 4 weeks. *Eur J Nucl Med Mol Imaging*;**2020**;47: 713-720.

113. Ahmadzadehfar H *et al.* Overall survival and response pattern of castration-resistant metastatic prostate cancer to multiple cycles of radioligand therapy using [¹⁷⁷Lu]Lu-PSMA-617. *European Journal of Nuclear Medicine and Molecular Imaging*. **2017**;44(9): 1448-1454.

114. von Eyben FE *et al.* PSMA diagnostics and treatments of prostate cancer become mature. *Clinical and Translational Imaging*. **2018**;6(2): 145-148.

115. Sharifi *et al.* Optimized Production Assessment, Compartmental Modeling and Dosimetric Evaluation of [¹⁷⁷Lu]- PSMA-617 for Clinical Trials. *International Journal of Nuclear Medicine Research*. **2017**;4: 19-29.

116. Eppard E *et al.* Clinical Translation and First In-Human Use of [⁴⁴Sc]Sc-PSMA-617 for PET Imaging of Metastasized Castrate-Resistant Prostate Cancer. *Theranostics*. **2017**;7(18): 4359-4369.

117. Rowdo FP *et al.* Immunotherapy in cancer: a combat between tumors and the immune system; you win some, you lose some. *Front Immunol.* **2015**;6: 127.

118. Apetoh L *et al.* Combining immunotherapy and anticancer agents: the right path to achieve cancer cure? *Ann Oncol.* **2015**;26(9): 1813-1823.

119. Kabasakal L *et al.* Lu-177-PSMA-617 Prostate-Specific Membrane Antigen Inhibitor Therapy in Patients with Castration-Resistant Prostate Cancer: Stability, Bio-distribution and Dosimetry. *Molecular Imaging and Radionuclide Therapy.* **2017**;26(2): 62-68.

120. Gosewisch A *et al.* 3D Monte Carlo bone marrow dosimetry for Lu-177-PSMA therapy with guidance of non-invasive 3D localization of active bone marrow via Tc-99m-anti-granulocyte antibody SPECT/CT. *EJNMMI Res.* **2019**; 76: 9.

121. Kabasakal L *et al.* Pre-therapeutic dosimetry of normal organs and tissues of [¹⁷⁷Lu]-PSMA-617 prostate-specific membrane antigen (PSMA) inhibitor in patients with castration-resistant prostate cancer. *European Journal of Nuclear Medicine and Molecular Imaging.* **2015**;42(13): 1976-1983.

122. Delker A *et al.* Dosimetry for [¹⁷⁷Lu]-DKFZ-PSMA-617: a new radiopharmaceutical for the treatment of metastatic prostate cancer. *European Journal of Nuclear Medicine and Molecular Imaging*. **2015**;43(1): 42-51.

123. Violet JA *et al.* Dosimetry of Lu-177 PSMA-617 in metastatic castration-resistant prostate cancer: correlations between pre-therapeutic imaging and “whole body” tumor dosimetry with treatment outcomes. *Journal of Nuclear Medicine*. **2018**; jnumed.118.219352.

124. Helmy KY *et al.* Cancer immunotherapy: accomplishments to date and future promise. *Therapeutic Delivery*. **2013**;4(10): 1307-1320.

125. Smyth MJ *et al.* Multiple approaches to immunotherapy - the new pillar of cancer treatment. *Immunology and Cell Biology*. **2017**;95(4): 323-324.

126. Hunter P. The fourth pillar. *EMBO Reports*. **2017**;18(11): 1889-1892.

127. Kelly PN. The Cancer Immunotherapy Revolution. *Science*. **2018**;359(6382): 1344-1345.

128. Immunotherapy: The Path to Win the War on Cancer? *Cell*. **2015**;161(2): 185-186.

129. Baxevanis CN *et al.* Cancer immunotherapy. *Critical Reviews in Clinical Laboratory Sciences*. **2009**;46(4): 167-189.

130. Yang Y. Cancer immunotherapy: harnessing the immune system to battle cancer. *Journal of Clinical Investigation*. **2015**;125(9): 3335-3337.

131. Kruger S *et al.* Advances in cancer immunotherapy 2019 - latest trends. *J Exp Clin Cancer Res*. **2019**;38(1): 268.

132. Hanahan D, Weinberg RA. Hallmarks of Cancer: The Next Generation. *Cell*. **2011**;144(5): 646-674.

133. Weinberg R. *The Biology of Cancer*. 2nd, revised edition. Taylor & Francis 2013.

134. Shitara K, Nishikawa H. Regulatory T cells: a potential target in cancer immunotherapy. *Annals of the New York Academy of Sciences*. **2018**;1417(1): 104-115.

135. Kumar P *et al.* (2018). A comprehensive review on the role of co-signaling receptors and Treg homeostasis in autoimmunity and tumor immunity. *Journal of Autoimmunity*. **2018**;95: 77-99.

136. Tanaka A , Sakaguchi S. Regulatory T cells in cancer immunotherapy. *Cell Research*. **2016**;27(1): 109-118.

137. Zou W. Regulatory T cells, tumour immunity and immunotherapy. *Nature Reviews Immunology*. **2006**;6(4): 295-307.

138. Haanen JBAG, Robert C. Immune Checkpoint Inhibitors. *ImmunoOncology*. **2015**; 42: 55-66.

139. Darvin P *et al.* Immune checkpoint inhibitors: recent progress and potential biomarkers. *Experimental & Molecular Medicine*. **2018**;50(12): 1-11.

140. Tang J *et al.* Trial watch: The clinical trial landscape for PD1/PDL1 immune checkpoint inhibitors. *Nature Reviews Drug Discovery*. **2018**;17(12): 854-855.

141. Mir MA. Developing Costimulatory Molecules for Immunotherapy of Diseases. Elsevier 2015.

142. Peters S, Stahel RA. Successes and Limitations of Targeted Cancer Therapy. Prog Tumor Res Basel - Karger. **2014**;(41): 1-6.

143. Janiczek M *et al.* Immunotherapy as a Promising Treatment for Prostate Cancer: A Systematic Review. J Immunol Res. 2017;2017:4861570 .

144. Lu YC, Robbins PF. Cancer immunotherapy targeting neoantigens. Seminars in Immunology. **2016**;28(1), 22-27.

145. Kantoff PW *et al.* Overall survival analysis of a phase II randomized controlled trial of a Poxviralbased PSA-targeted immunotherapy in metastatic castration-resistant prostate cancer. J Clin Oncol. **2010**;28: 1099-1105.

146. Noguchi M *et al.* A randomized phase II trial of personalized peptide vaccine plus low dose estramustine phosphate (EMP) versus standard dose EMP in patients with castration resistant prostate cancer. Cancer Immunol Immunother. **2010**;59: 1001-1009.

147. Sonpavde G *et al.* HLA-restricted NY-ESO-1 peptide immunotherapy for metastatic castration resistant prostate cancer. Invest New Drugs. **2014**;32: 235-242.

148. McNeel DG *et al.* Safety and immunological efficacy of a DNA vaccine encoding prostatic acid phosphatase in patients with stage D0 prostate cancer. *J Clin Oncol.* **2009**;27: 4047-4054.
149. Kantoff PW *et al.* Sipuleucel-T immunotherapy for castration-resistant prostate cancer. *N Engl J Med*; **2010**;363: 411-422.
150. Topalian SL *et al.* Safety, activity, and immune correlates of anti-PD-1 antibody in cancer. *N Engl J Med*; **2012**;366: 2443-2454.
151. Alexandrov LB *et al.* Signatures of mutational processes in human cancer. *Nature*; **2013**;500:415–421.
152. Mansurov, A *et al.* Collagen-binding IL-12 enhances tumour inflammation and drives the complete remission of established immunologically cold mouse tumours. *Nature Biomedical Engineering*; **2020**;4(5):531-543.
153. Graff *et al.* Early evidence of antiPD1 activity in enzalutamide-resistant prostate cancer. *Oncotarget.* **2016**;7(33): 52810-52817.
154. De Velasco MA, Uemura H. Prostate cancer immunotherapy. *Current Opinion in Urology.* **2018**;28(1): 15-24.

155. Bilusic M *et al.* Immunotherapy of Prostate Cancer: Facts and Hopes. *Clinical Cancer Research*. **2017**;23(22): 6764-6770.
156. Risk M, Corman JM. The role of immunotherapy in prostate cancer: an overview of current approaches in development. *Rev Urol*. **2009**;11(1): 16-27.
157. Pizzola C *et al.* A New Era of Immunotherapy in Prostate Cancer. *2016*;9(3): 217-225.
158. Al-Shamkhani A *et al.* OX40 is differentially expressed on activated rat and mouse T cells and is the sole receptor for the OX40 ligand. *European Journal of Immunology*. **1996**;26(8): 1695-1699.
159. Webb GJ *et al.* OX40, OX40L and Autoimmunity: a Comprehensive Review. *Clin Rev Allergy Immunol*. **2015**; 50(3): 312-32.
160. Redmond WL *et al.* The role of OX40-mediated co-stimulation in T-cell activation and survival. *Crit Rev Immunol*. **2009**;29(3): 187-201.
161. Fromm G *et al.* Agonist redirected checkpoint, PD1-Fc-OX40L, for cancer immunotherapy. *Journal for ImmunoTherapy of Cancer*. **2018**;6(1).

162. Aspeslagh S *et al.* (2016). Rationale for anti-OX40 cancer immunotherapy. *European Journal of Cancer*. 2016;52: 50-66.

163. Slovin SF *et al.* Ipilimumab alone or in combination with radiotherapy in metastatic castration-resistant prostate cancer: results from an open-label, multicenter phase I/II study. *Ann Oncol*. **2013**;24: 1813-1821.

164. Borradori *et al.* Rescue therapy with anti-programmed cell death protein 1 inhibitors of advanced cutaneous squamous cell carcinoma and basosquamous carcinoma: preliminary experience in five cases. *Br J Dermatol*. **2016**;175(6): 1382-1386.

165. Kwon ED *et al.* Ipilimumab versus placebo after radiotherapy in patients with metastatic castration-resistant prostate cancer that had progressed after docetaxel chemotherapy (CA184-043): a multicentre, randomised, double-blind, phase 3 trial. *Lancet Oncol*. **2014**;15: 700-712.

166. Golden EB *et al.* An abscopal response to radiation and ipilimumab in a patient with metastatic non-small cell lung cancer. *Cancer Immunol Res*. **2013**; 1(6): 365-372.

167. Piconese S *et al.* OX40 triggering blocks suppression by regulatory T cells and facilitates tumor rejection. *The Journal of Experimental Medicine*. **2008**;205(4): 825-839.

168. Buchan SL *et al.* The immunobiology of CD27 and OX40 and their potential as targets for cancer immunotherapy. *Blood*. **2017**; 131(1): 39-48.

169. Berrong Z *et al.* Antigen-Specific Antitumor Responses Induced by OX40 Agonist Are Enhanced by the IDO Inhibitor Indoximod. *Cancer Immunology Research*. **2018**;6(2): 201-208.

170. Shrimali RK *et al.* Concurrent PD-1 Blockade Negates the Effects of OX40 Agonist Antibody in Combination Immunotherapy through Inducing T-cell Apoptosis. *Cancer Immunology Research*. **2017**;5(9): 755-766.

171. Piconese S. Human OX40 Tunes the Function of Regulatory T Cells in Tumor and Nontumor Areas of Hepatitis C Virus-Infected Liver Tissue. *Hepatology*. **2014**;60: 1494-1507.

172. Hirschhorn-Cymerman D. OX40 engagement and chemotherapy combination provides potent antitumor immunity with concomitant regulatory T cell apoptosis. *The Journal of Experimental Medicine*. **2009**;206(5): 1103-1116.

173. Sadun RE *et al.* Fc-mOX40L Fusion Protein Produces Complete Remission and Enhanced Survival in 2 Murine Tumor Models. *Journal of Immunotherapy*. **2009**;31(3): 235-245.

174. Chonan M *et al.* CD40/CD40L expression correlates with the survival of patients with glioblastomas and an augmentation in CD40 signaling enhances the efficacy of vaccinations against glioma models. *Neuro-Oncology*. **2015**;17(11): 1453-1462.
175. Bresson D *et al.* Antigen-specific prevention of type 1 diabetes in NOD mice is ameliorated by OX40 agonist treatment. *Journal of Autoimmunity*. **2011**;37(4): 342-351.
176. Zhang P *et al.* Ligand-Blocking and Membrane-Proximal Domain Targeting Anti-OX40 Antibodies Mediate Potent T Cell-Stimulatory and Anti-Tumor Activity. *Cell Reports*. **2019**;27(11): 3117-3123.e5.
177. Jin H *et al.* OX40 expression in neutrophils promotes hepatic ischemia/reperfusion injury. *JCI Insight*. **2019**;4(21): e129736.
178. Bulliard Y *et al.* OX40 engagement depletes intratumoral Tregs via activating FcγRs, leading to antitumor efficacy. *Immunology and Cell Biology*. **2014**;92(6): 475-480.
179. Burocchi A *et al.* Intratumor OX40 stimulation inhibits IRF1 expression and IL-10 production by Treg cells while enhancing CD40L expression by effector memory T cells. *European Journal of Immunology*. **2011**;41(12): 3615-3626.

180. Liu K *et al.* OX40 regulates the conversion and suppressive function of double-negative regulatory T cells. *International Immunopharmacology*. **2018**;65: 16-22.

181. Ngwa W *et al.* Using immunotherapy to boost the abscopal effect. *Nature Reviews Cancer*. **2018**;18(5): 313-322.

182. Liu Y *et al.* Abscopal effect of radiotherapy combined with immune checkpoint inhibitors. *Journal of Hematology & Oncology*. **2018**;11(1): 104.

183. Hu ZI *et al.* The Abscopal Effect of Radiation Therapy: What Is It and How Can We Use It in Breast Cancer? *Current Breast Cancer Reports*. **2017**;9(1): 45-51.

184. Abuodeh Y *et al.* Systematic review of case reports on the abscopal effect. *Current Problems in Cancer*. **2016**;40(1): 25-37.

185. Rodríguez-Ruiz ME *et al.* Immunological Mechanisms Responsible for Radiation-Induced Abscopal Effect. *Trends in Immunology*. **2018**;39(8): 644-655.

186. Reynders K *et al.* The abscopal effect of local radiotherapy: using immunotherapy to make a rare event clinically relevant. *Cancer Treatment Reviews*. **2015**;41(6), 503-510.

187. Buchwald ZS *et al.* Radiation, Immune Checkpoint Blockade and the Abscopal Effect: A Critical Review on Timing, Dose and Fractionation. *Frontiers in Oncology*. **2018**;8: 612.

188. Dagoglu N *et al.* Abscopal Effect of Radiotherapy in the Immunotherapy Era: Systematic Review of Reported Cases. *Cureus*. **2019**;11(2): e4103.

189. Yilmaz M *et al.* Abscopal Effect, From Myth to Reality: From Radiation Oncologists' Perspective. *Cureus*. **2019**;11(1): e3860.

190. Macki M *et al.* Trends in the Abscopal Effect After Radiation to Spinal Metastases: A Systematic Review. *Cureus*. **2019**;11(10): e5844.

191. Suek N, Khalil D. Targeted APC activation in cancer immunotherapy to enhance the abscopal effect. *Front Immunol*. **2019**;10: 604.

192. Jatoi I *et al.* Hypothesis: can the abscopal effect explain the impact of adjuvant radiotherapy on breast cancer mortality? *NPJ Breast Cancer*. **2018**; 4(1): 8.

193. Lauber K, Dunn L. Immunotherapy Mythbusters in Head and Neck Cancer: The Abscopal Effect and Pseudoprogession. American Society of Clinical Oncology Educational Book. **2019**;(39): 352-363.
194. Grass GD *et al.* The immune mechanisms of abscopal effect in radiation therapy. Current Problems in Cancer. **2016**;40(1): 10-24.
195. Wani SQ *et al.* Radiation Therapy and its Effects Beyond the Primary Target: An Abscopal Effect. Cureus. **2019**;11(2): e4100.
196. Yasuda K *et al.* Intratumoral injection of interleukin-2 augments the local and abscopal effects of radiotherapy in murine rectal cancer. Cancer Sci. **2011**;102: 1257-1263.
197. Demaria S *et al.* Ionizing radiation inhibition of distant untreated tumors (abscopal effect) is immune mediated. Int J Radiat Oncol Biol Phys. **2004**;58: 862-870.
198. Dewan MZ *et al.* Fractionated but not single-dose radiotherapy induces an immune-mediated abscopal effect when combined with anti-CTLA-4 antibody. Clin Cancer Res. **2009**;15: 5379-5388.

199. Postow MA *et al.* Immunologic correlates of the abscopal effect in a patient with melanoma. *N Engl J Med.* **2012**;366: 925-931.

200. Hiniker SM *et al.* A systemic complete response of metastatic melanoma to local radiation and immunotherapy. *Transl Oncol.* **2012**;5:404-407.

201. Golden EB *et al.* Local radiotherapy and granulocyte-macrophage colony-stimulating factor to generate abscopal responses in patients with metastatic solid tumours: a proof-of-principle trial. *Lancet Oncol.* **2015**;16: 795-803.

202. Poleszczuk JT *et al.* Abscopal benefits of localized radiotherapy depend on activated T-cell trafficking and distribution between metastatic lesions. *Cancer Res.* **2016**;76: 1009-1018.

203. Stamell EF *et al.* The abscopal effect associated with a systemic anti-melanoma immune response. *Int J Radiat Oncol Biol Phys.* **2013**;85: 293-295.

204. Antoniades J *et al.* Lymphangiographic demonstration of the abscopal effect in patients with malignant lymphomas. *Int J Radiat Oncol Biol Phys.* **1977**;2: 141-147.

205. Robins HI *et al.* The abscopal effect: demonstration in lymphomatous involvement of kidneys. *Med Pediatr Oncol.* **1981**;9: 473-476.

206. Kingsley DP. An interesting case of possible abscopal effect in malignant melanoma. *Br J Radiol.* **1975**;48: 863-866.

207. Reynders K *et al.* The abscopal effect of local radiotherapy: using immunotherapy to make a rare event clinically relevant. *Cancer Treat Rev.* **2015**;41: 503-510.

208. O'Regan B, Hirshberg C. Spontaneous remission: an annotated bibliography. Petaluma: Institute of Noetic Sciences Sausalito, **1993**.

209. Hodge JW *et al.* Abscopal regression of antigen disparate tumors by antigen cascade after systemic tumor vaccination in combination with local tumor radiation. *Cancer Biother Radiopharm.* **2012**;27:12-22.

210. Demaria S *et al.* Immune-mediated inhibition of metastases after treatment with local radiation and CTLA-4 blockade in a mouse model of breast cancer. *Clin Cancer Res.* **2005**;11: 728-734.

211. Vatner RE *et al.* Combinations of immunotherapy and radiation in cancer therapy. *Front Oncol.* **2014**;4: 325.

212. Formenti SC, Demaria S. Combining radiotherapy and cancer immunotherapy: a paradigm shift. *J Natl Cancer Inst.* **2013**;105(4) :256-265.

213. Olson B *et al.* Mouse Models for Cancer Immunotherapy Research. *Cancer Discovery.* **2018**;8(11): 1358-1365.

214. Risbridger GP *et al.* Preclinical Models of Prostate Cancer: Patient-Derived Xenografts, Organoids, and Other Explant Models. *Cold Spring Harbor Perspectives in Medicine.* **2018**;8(8): a030536.

215. Grabowska MM *et al.* Mouse models of prostate cancer: picking the best model for the question. *Cancer and Metastasis Reviews.* **2014**;33(2-3): 377-397.

216. Kelsey R. Prostate cancer: Mouse model for testing treatments. *Nature Reviews Urology.* **2018**;15(4): 205.

217. Hurwitz AA *et al.* The TRAMP Mouse as a Model for Prostate Cancer. *Current Protocols in Immunology*. **2001**; Chapter 20: Unit 20.5.
218. Lardizabal J *et al.* A TRAMP-derived orthotopic prostate syngeneic (TOPS) cancer model for investigating anti-tumor treatments. *The Prostate*. **2018**;78(6): 457-468.
219. Urano K *et al.* Establishing a Laboratory Animal Model From a Transgenic Animal. *Veterinary Pathology*. **2001**;49(1): 16-23.
220. Schaeffer LR. Necessary changes to improve animal models. *Journal of Animal Breeding and Genetics*. **2018**;135(2): 124-131.
221. Jindal V. Immunotherapy: a glimmer of hope for metastatic prostate cancer. *Chin Clin Oncol*. **2018**;7(6): 61.
222. Marin-Acevedo JA *et al.* Cancer immunotherapy beyond immune checkpoint inhibitors. *Journal of Hematology & Oncology*. **2018**;11(1): 8.
223. Fendler WP *et al.* Establishing [¹⁷⁷Lu]-PSMA-617 Radioligand Therapy in a Syngeneic Model of Murine Prostate Cancer. *J Nucl Med*. **2017**;58(11): 1786-1792.

224. Heitkötter B *et al.* Expression of PSMA in tumor neovasculature of high grade sarcomas including synovial sarcoma, rhabdomyosarcoma, undifferentiated sarcoma and MPNST. *Oncotarget*. **2017**;8(3): 4268-4276.

225. Zaini J *et al.* OX40 ligand expressed by DCs costimulates NKT and CD4+ Th cell antitumor immunity in mice. *J Clin Invest*. **2007**;117(11): 3330-3338.

226. Melero I *et al.* Agonist antibodies to Clinix Rev Allerg Immunol TNFR molecules that costimulate T and NK cells. *Clin Cancer Res: Off J Am Assoc Cancer Res*. **2013**;19(5): 1044-1053.

227. Baumann R *et al.* Functional expression of CD134 by neutrophils. *Eur J Immunol*. **2004**;34(8): 2268-2275.

228. Gramaglia I *et al.* The OX40 costimulatory receptor determines the development of CD4 memory by regulating primary clonal expansion. *J Immunol*. **2000**;165: 3043-3050.

229. Maxwell J *et al.* Danger and OX40 receptor signaling synergize to enhance memory T cell survival by inhibiting peripheral deletion. *J Immunol*. **2000**;164: 107-112.

230. Wang HC, Klein JR. Multiple levels of activation of murine CD8(+) intraepithelial lymphocytes defined by OX40 (CD134) expression: effects on cell-mediated cytotoxicity, IFN-gamma, and IL-10 regulation. *J Immunol.* **2001**;167: 6717-6723.
231. Biagi E *et al.* Molecular transfer of CD40 and OX40 ligands to leukemic human B cells induces expansion of autologous tumor-reactive cytotoxic T lymphocytes. *Blood.* **2005**;105(6): 2436-2442.
232. Pan PY *et al.* OX40 ligation enhances primary and memory cytotoxic T lymphocyte responses in an immunotherapy for hepatic colon metastases. *Mol Ther.* **2002**;6(4): 528-536.
233. Croft M *et al.* The significance of OX40 and OX40L to T-cell biology and immune disease. *Immunological Reviews.* **2009**;229(1): 173-191.
234. Murata K *et al.* Constitutive OX40/OX40 Ligand Interaction Induces Autoimmune-Like Diseases. *The Journal of Immunology.* **2002**;169(8): 4628-4636.
235. Soroosh P *et al.* Differential Requirements for OX40 Signals on Generation of Effector and Central Memory CD4 + T Cells . *The Journal of Immunology.* **2007**;179(8): 5014-5023.
236. Takeda I *et al.* Distinct Roles for the OX40-OX40 Ligand Interaction in Regulatory and Nonregulatory T Cells. *The Journal of Immunology.* **2004**;172(6): 3580-3589.

237. Rogers PR *et al.* OX40 Promotes Bcl-xL and Bcl-2 Expression and Is Essential for Long-Term Survival of CD4 T Cells. *Immunity*. **2001**;15(3): 445-455.

238. Song J *et al.* The costimulation-regulated duration of PKB activation controls T cell longevity. *Nat Immunol*. **2004**;5: 150-158.

239. Niknam S *et al.* Radiation followed by OX40 stimulation drives local and abscopal antitumor effects in an anti-PD1-resistant lung tumor model. *Clinical Cancer Research*. **2018**;24(22): S735-S744.

240. Zhang D *et al.* Fc γ RII-binding Centyrins mediate agonism and antibody-dependent cellular phagocytosis when fused to an anti-OX40 antibody. *mAbs*. **2018**;10(3): 463-475.

241. Sagiv-Barfi I *et al.* Eradication of spontaneous malignancy by local immunotherapy. *Science Translational Medicine*. **2018**;10(426): eaan4488.

242. Yu JW *et al.* Tumor-immune profiling of murine syngeneic tumor models as a framework to guide mechanistic studies and predict therapy response in distinct tumor microenvironments. *PLOS ONE*. **2018**;13(11): e0206223.

243. Demaria S, *et al.* Role of Local Radiation Therapy in Cancer Immunotherapy. *JAMA Oncol*; **1**: 1325.

244. Alexandro LB *et al.* Signatures of mutational processes in human cancer. *Nature*. **2013**;500: 415-421.
245. Chakraborty M *et al.* Use of radiolabeled monoclonal antibody to enhance vaccine-mediated antitumor effects. *Cancer Immunol Immunother* 2008; **57**: 1173-1183.
246. Chakraborty M *et al.* The use of chelated radionuclide (samarium-153-ethylenediaminetetramethylenephosphonate) to modulate phenotype of tumor cells and enhance T cellmediated killing. *Clin Cancer Res* 2008; **14**: 4241-4249.
247. Gorin JB *et al.* Antitumor immunity induced after alpha irradiation. *Neoplasia*; **16**: 319-328.
248. Schepisi G *et al.* Immunotherapy for prostate cancer: Where we are headed. *Int. J. Mol. Sci.* **2017**;18: E2627.
249. De Santis M. Immuntherapie beim Prostatakarzinom - aus Alt macht Neu?. *Urologe*. **2018**;57: 1342-1345.
250. Benesova M *et al.* Linker modification strategies to control the prostate-specific membrane antigen (PSMA)-targeting and pharmacokinetic properties of DOTA-conjugated PSMA inhibitors. *J Med Chem.* **2016**;59:1761-1775.

251. Kuo HT *et al.* One-Step ^{18}F -Labeling and Preclinical Evaluation of Prostate-Specific Membrane Antigen Trifluoroborate Probes for Cancer Imaging. *J Nucl Med* **2019**;60(8):1160-1166.
252. Bouvet V *et al.* Automated synthesis of [^{18}F]DCFPyL via direct radiofluorination and validation in preclinical prostate cancer models. *EJNMMI Res.* **2016**;6: 40.
253. Kitagawa K *et al.* Preclinical development of a WT1 oral cancer vaccine using a bacterial vector to treat castration-resistant prostate cancer. *Mol Cancer Ther* **2019**;18(5): 980-990.
254. Bouchelouche K *et al.* PSMA PET and Radionuclide Therapy in Prostate Cancer. *Semin Nucl Med.* **2016**;46(6): 522-535.
255. Sheikhabaei S *et al.* Pearls and pitfalls in clinical interpretation of prostate-specific membrane antigen (PSMA)-targeted PET imaging. *Eur J Nucl Med Mol Imaging* **2017**;44(12): 2117-2136.
256. Haberkorn U *et al.* New Strategies in Prostate Cancer: Prostate-Specific Membrane Antigen (PSMA) Ligands for Diagnosis and Therapy. *Clin Cancer Res* **2016**;22(1): 9-15.

257. Chen Y *et al.* 2-(3-{1-Carboxy-5-[(6-[¹⁸F]fluoro-pyridine-3-carbonyl)-amino]-pentyl}-ureido)-pentanedioic acid, [¹⁸F]DCFPyL, a PSMA-based PET imaging agent for prostate cancer. *Clin Cancer Res* **2011**;17(24): 7645-53.
258. Baker *et al.* Direct Visualization of Heterogeneous Extravascular Distribution of Trastuzumab in Human Epidermal Growth Factor Receptor Type 2 Overexpressing Xenografts. *Clinical Cancer Research*. **2008**;14(7), 2171–2179.
259. Euhus DM *et al.* Tumor measurement in the nude mouse. *Journal of Surgical Oncology*. **1986**;31(4): 229–234.
260. Tomayko MM *et al.* Determination of subcutaneous tumor size in athymic (nude) mice. *Cancer Chemotherapy and Pharmacology*. **1989**;24(3), 148–154.
261. Castanares MA *et al.* Evaluation of Prostate-Specific Membrane Antigen as an Imaging Reporter. *J Nucl Med* **2014**(55): 805-811.
262. Das A *et al.* Selecting the optimal Tet-On system for doxycycline-inducible gene expression in transiently transfected and stably transduced mammalian cells. *Biotechnol J* **2016**(11); 71-79.
263. Gossen M *et al.* Tetracyclines in Biology, Chemistry and Medicine, Birkhäuser Verlag, Basel CH **2001**, pp. 139-157.

264. Baron U *et al.* Tet repressor-based system for regulated gene expression in eukaryotic cells: Principles and advances. *Methods Enzymol.* **2000**;327: 401-421.
265. Berens C *et al.* Gene regulation by tetracyclines. Constraints of resistance regulation in bacteria shape TetR for application in eukaryotes. *Eur J Biochem* **2003**;70: 3109-3121.
266. Gossen M *et al.* Tight control of gene expression in mammalian cells by tetracycline-responsive promoters. *Proc Natl Acad Sci USA* **1992**;89: 5547-5551.
267. Gossen M *et al.*, Transcriptional activation by tetracyclines in mammalian cells. *Science* **1995**(268): 1766-1769.
268. Mohammadi S *et al.* Delay in resumption of the activity of tetracycline-regulatable promoter following removal of tetracycline analogues. *Gene Ther* **1997**(4), 993-997.
269. Brader P *et al.* Noninvasive molecular imaging using reporter genes. *J Nucl Med* **2013**(54), 167-172.
270. Foster BA *et al.* Characterization of prostatic epithelial cell lines derived from transgenic adenocarcinoma of the mouse prostate (TRAMP) model. *Cancer Res* **1997**;57(16):3325-30.

271. Costello A *et al.* Leaky Expression of the TET-On System Hinders Control of Endogenous miRNA Abundance. *Biotechnology Journal*. **2019**;14(3): e1800219.
272. Brader P *et al.* Noninvasive molecular imaging using reporter genes. *J Nucl Med* **2013**;(54): 167-172.
273. Volpe A *et al.* Cousins at work: How combining medical with optical imaging enhances in vivo cell tracking. *Int J Biochem Cell Biol* **2018**;(02):40-50.
274. Fruhwirth GO *et al.* The Potential of In Vivo Imaging for Optimization of Molecular and Cellular Anti-cancer Immunotherapies. *Mol Imaging Biol*. **2018** ;20(5): 696-704.
275. Bhatnagar A *et al.* AEG-1 promoter-mediated imaging of prostate cancer. *Cancer Res*. **2014**;74(20): 5772-81.
276. Kuo HT *et al.* Enhancing Treatment Efficacy of [¹⁷⁷Lu]-PSMA-617 with the Conjugation of an Albumin-Binding Motif: Preclinical Dosimetry and Endoradiotherapy Studies. *Mol Pharm*. **2018**;15(11): 5183–5191.
277. Zhan W *et al.* The effect of tumour size on drug transport and uptake in 3-D tumour models reconstructed from magnetic resonance images. *PLoS ONE* **2012**;12(2):e0172276.

Appendices

Appendix A – Flow cytometry study results – clones 1, 14, 16 and 19

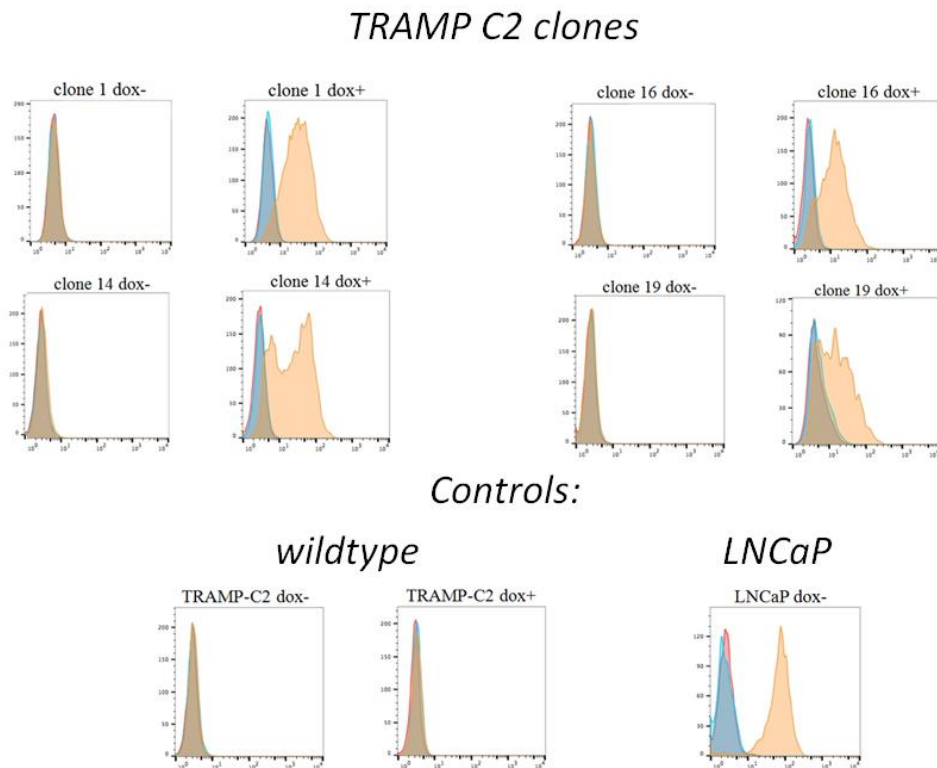


Figure A-1: Flow cytometry histograms for 4 parental TRAMP-C2 transfected clones with and without doxycycline induction; and wildtype TRAMP-C2 and LNCaP controls. Of note is successful induction of parental clones and evident presence of subpopulations in clones 14 and 19, with varying degrees of PSMA-expression.

Abscissae: FL1-H

Ordinates: Cell count

Red: unstained

Blue: isotype IgG

Orange: anti-FOLH1 (= anti-PSMA)

Appendix B – Tumour growth inhibition graphs

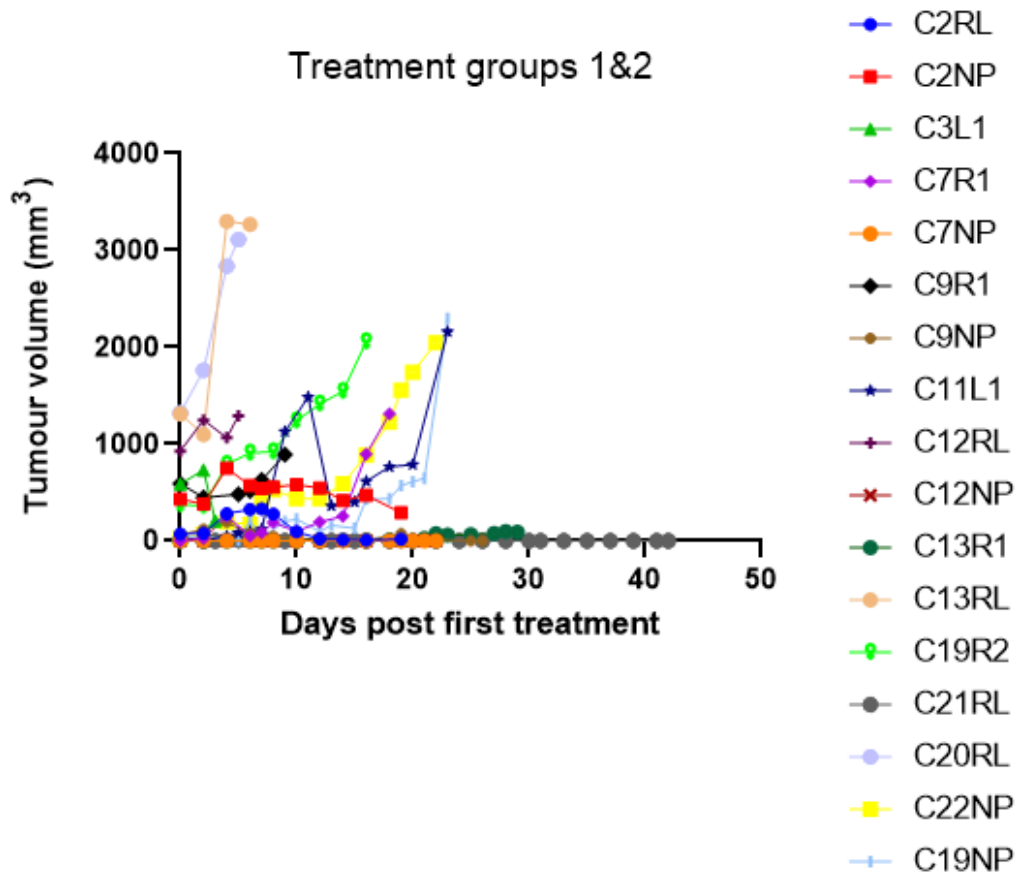


Figure B-1: Tumour volumes plotted over time for 17 different tumours in treatment groups #1 and #2. Of note is tumour growth inhibition happening for a series of tumours in both groups (C2RL, C2NP, C11L1). Volume differences for tumours with low volume at the timepoint of the (first) treatment is difficult to interpret in this graph.

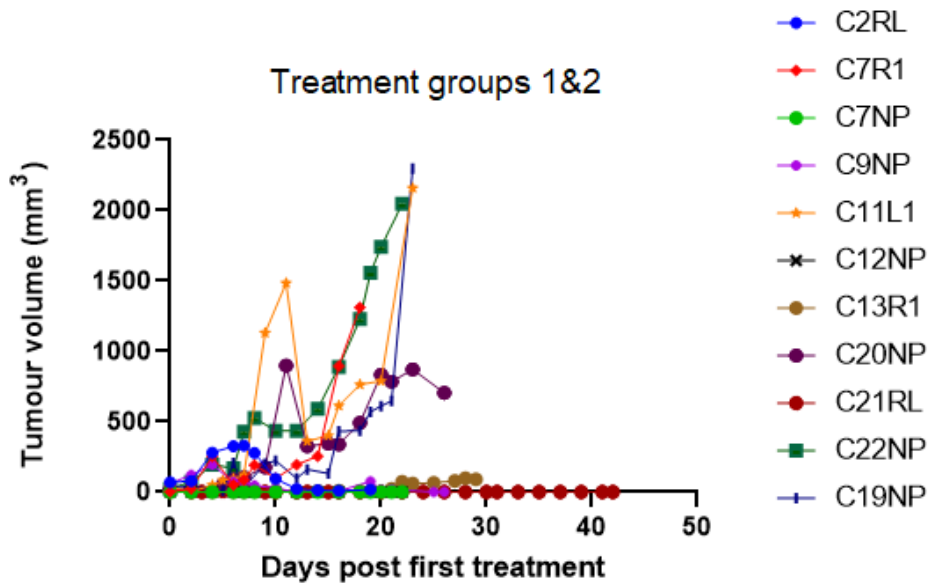


Figure B-2: Tumour volumes plotted over time for 11 different tumours in treatment groups #1 and #2, excluding larger tumours for better visualization. Of note is intermittent growth inhibition for tumours C11L1, C20NP and C22NP.

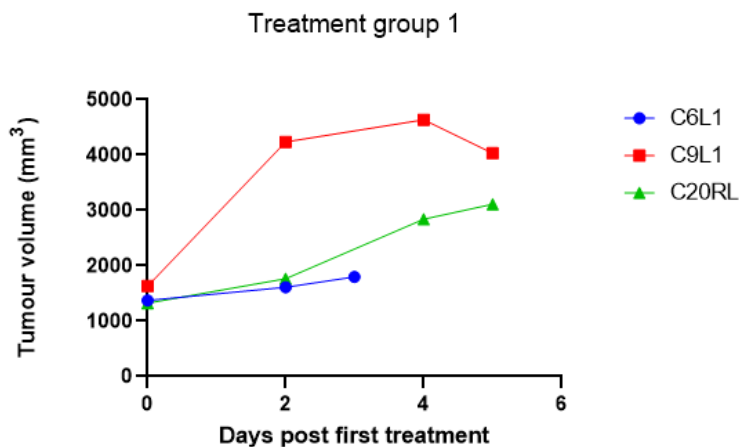


Figure B-3: Tumour volumes plotted over time for 3 different tumours in treatment group #1, showing weak growth inhibition for tumours with volumes larger than 1000 mm³ at the timepoint of the first treatment.

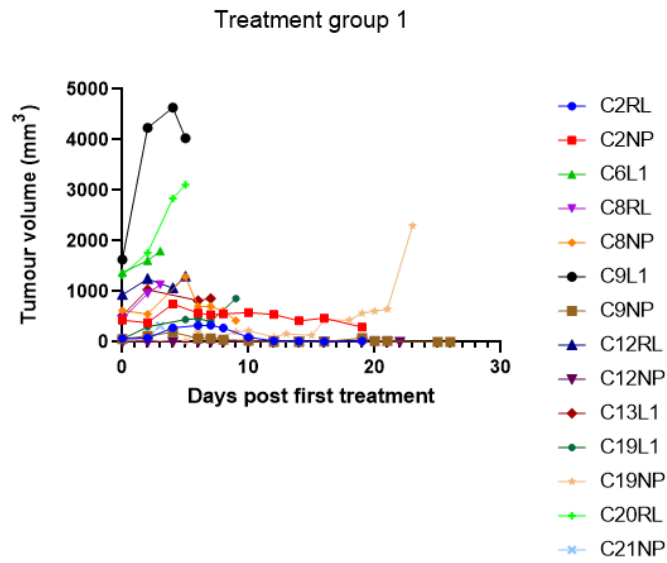


Figure B-4: Tumour volumes plotted over time for 14 different tumours in treatment group #1, showing stronger growth inhibition for tumours with volumes below 1000 mm³ at the timepoint of the first treatment.

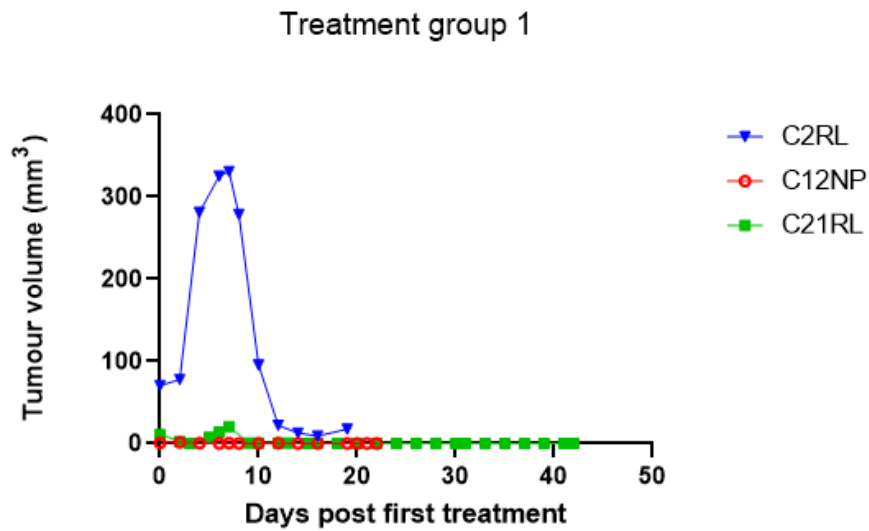


Figure B-5: Tumour volumes plotted over time for 3 different tumours in treatment group #1, with volumes below 100 mm³ at the timepoint of the first treatment, showing efficient tumour growth inhibition.

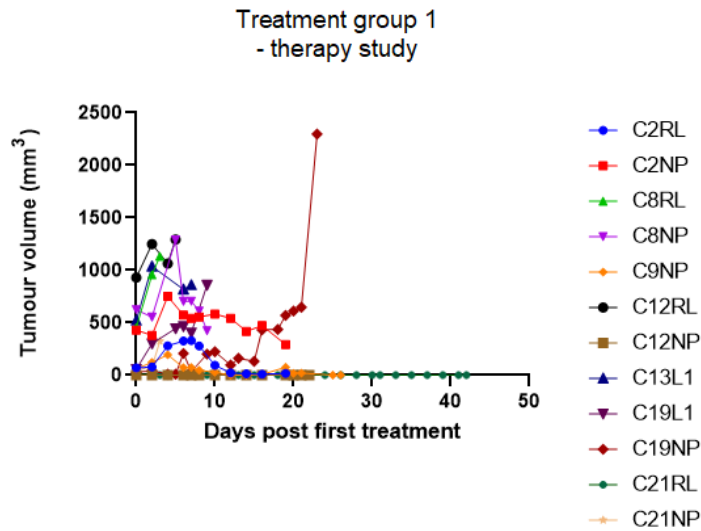


Figure B-6: Tumour volumes plotted over time for 12 different tumours in treatment group #1, with volumes below 1000 mm³ at the timepoint of the first treatment, showing efficient tumour growth inhibition for 6 tumours up until day 20 and for tumour ID C21RL until the termination of the study. Of note is quick growth in tumour C19NP after 22 days of successful growth inhibition.

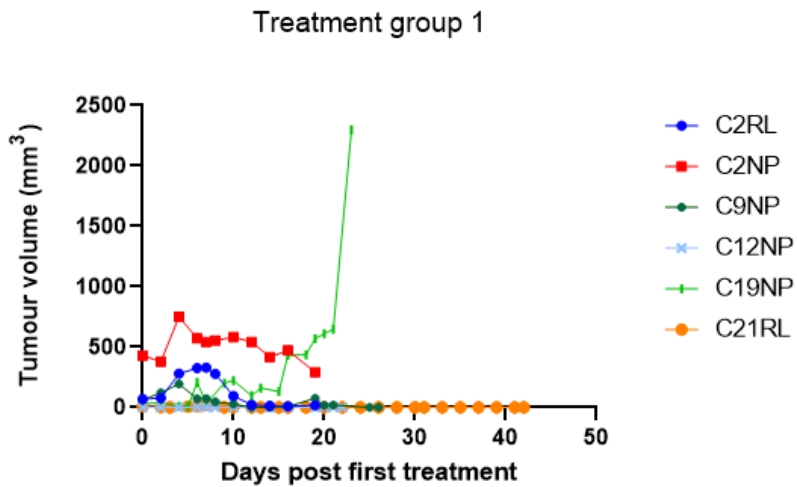


Figure B-7: Tumour volumes plotted over time for 6 different tumours in treatment group #1, with volumes below 500 mm³ at the timepoint of the first treatment, showing efficient tumour growth inhibition for 5/6 tumours in the study.

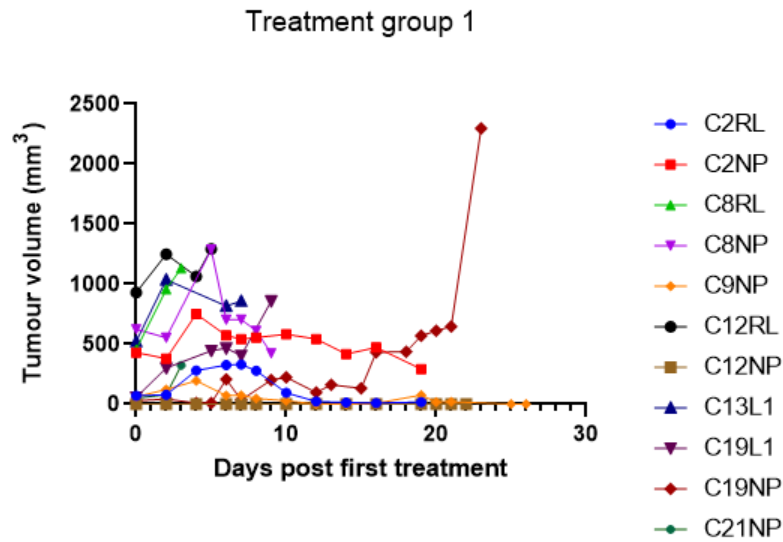


Figure B-8: Tumour volumes plotted over time for 11 different tumours in treatment group #1, with volumes below 1000 mm³ at the timepoint of the first treatment, showing efficient tumour growth inhibition for all tumours except tumour ID C8RL (tumour used for harvesting).

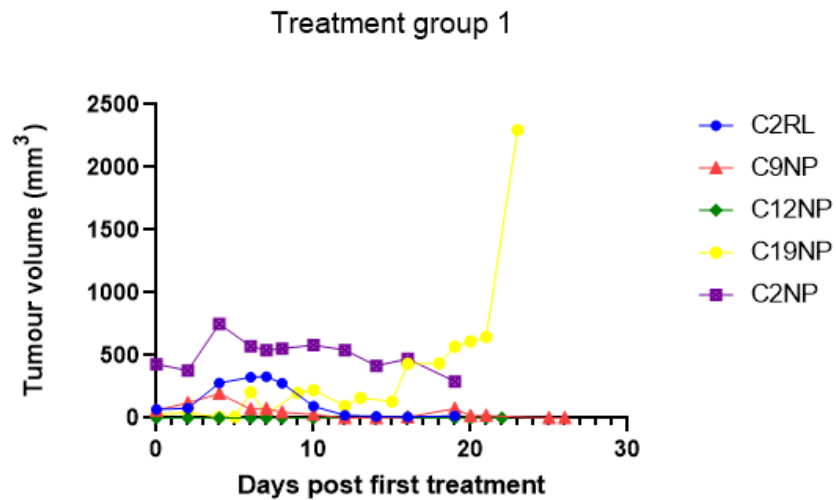


Figure B-9: Tumour volumes plotted over time for 5 different tumours in treatment group #1, with volumes below 500 mm³ at the timepoint of the first treatment, showing efficient tumour growth inhibition for all tumours up until day 20 post first treatment.

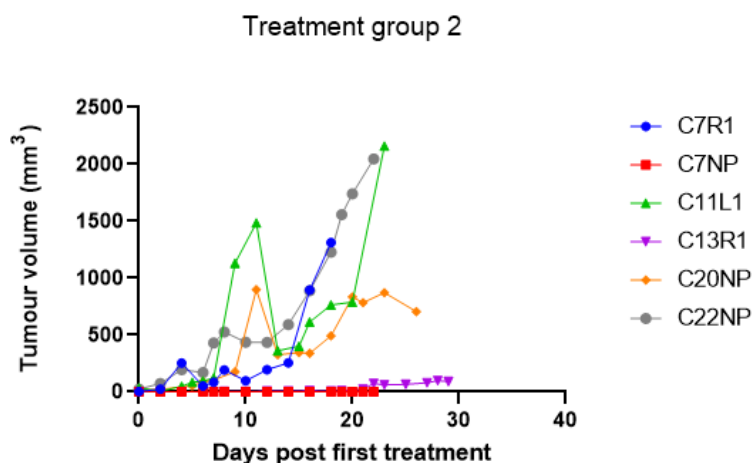


Figure B-10: Tumour volumes plotted over time for 6 different tumours in treatment group #2, with volumes below 100 mm³ at the timepoint of the first treatment, showing efficient tumour growth inhibition for tumours C7NP, C13R1 and C20NP during the entire study, and for tumours C7R1 C11L1 and C22NP for longer than 14 days post treatment.

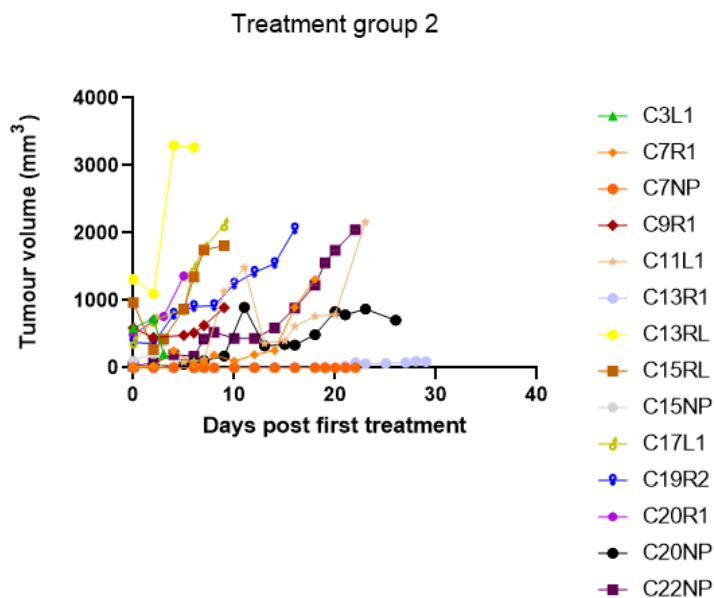


Figure B-11: Tumour volumes plotted over time for 14 different tumours in treatment group #2, showing varying tumour growth inhibition.

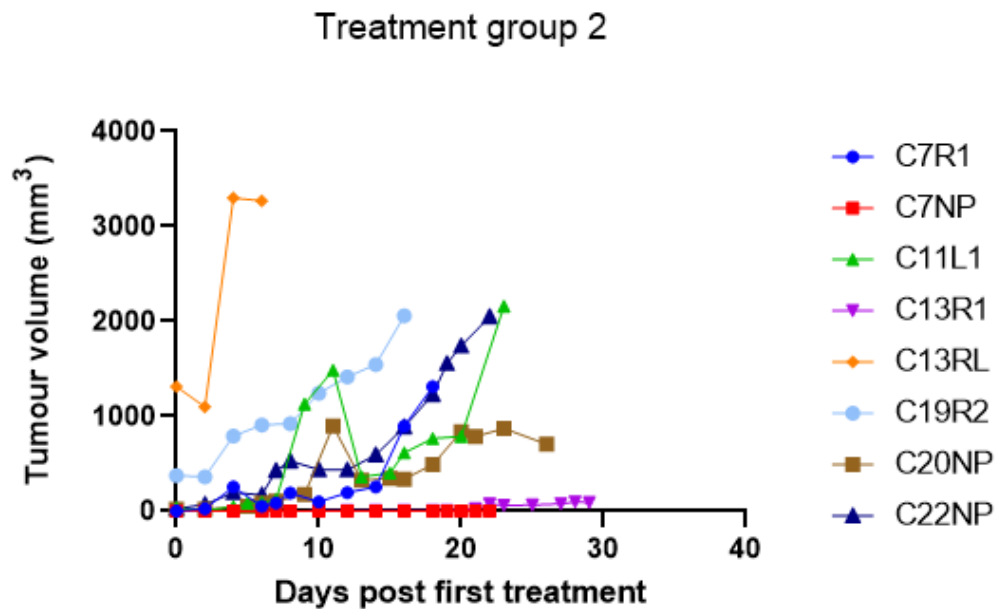


Figure B-12: Tumour volumes plotted over time for 8 different tumours in treatment group #2, showing different degrees of tumour growth inhibition.

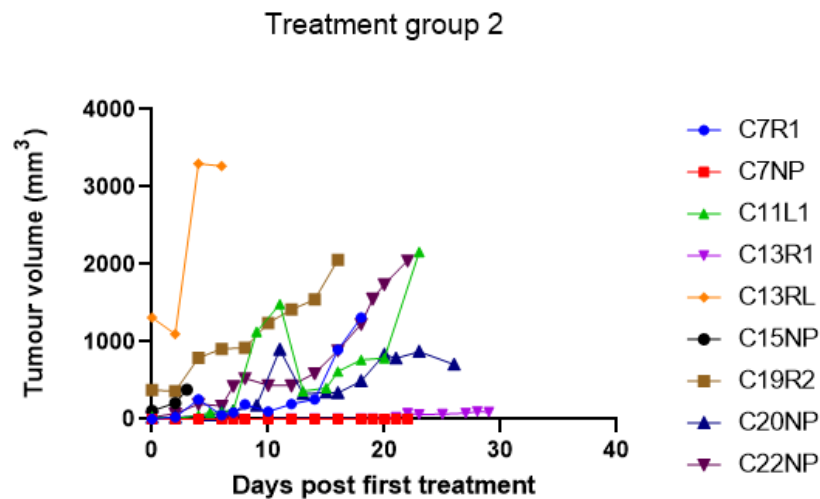


Figure B-13: Tumour volumes plotted over time for 9 different tumours in treatment group #2, showing varying degrees of tumour inhibition. Of note is that tumour ID C15NP was used for harvesting early on in the study (Table 4.6; Figure 5.1b).

Appendix C

FACS studies on excised TRAMP-C2 tumour tissue

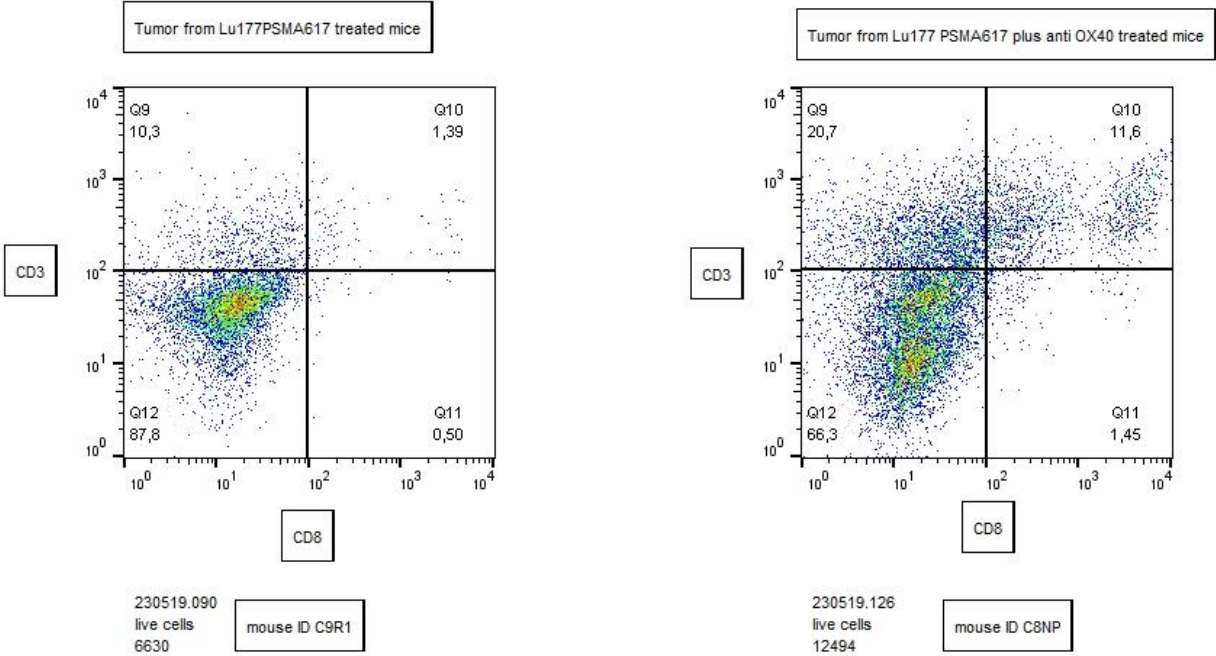


Figure C-1: Flow cytometry data depicting larger proportion of CD3⁺CD8⁺ tumour-infiltrating cytotoxic T-lymphocytes in Treatment Group #1.

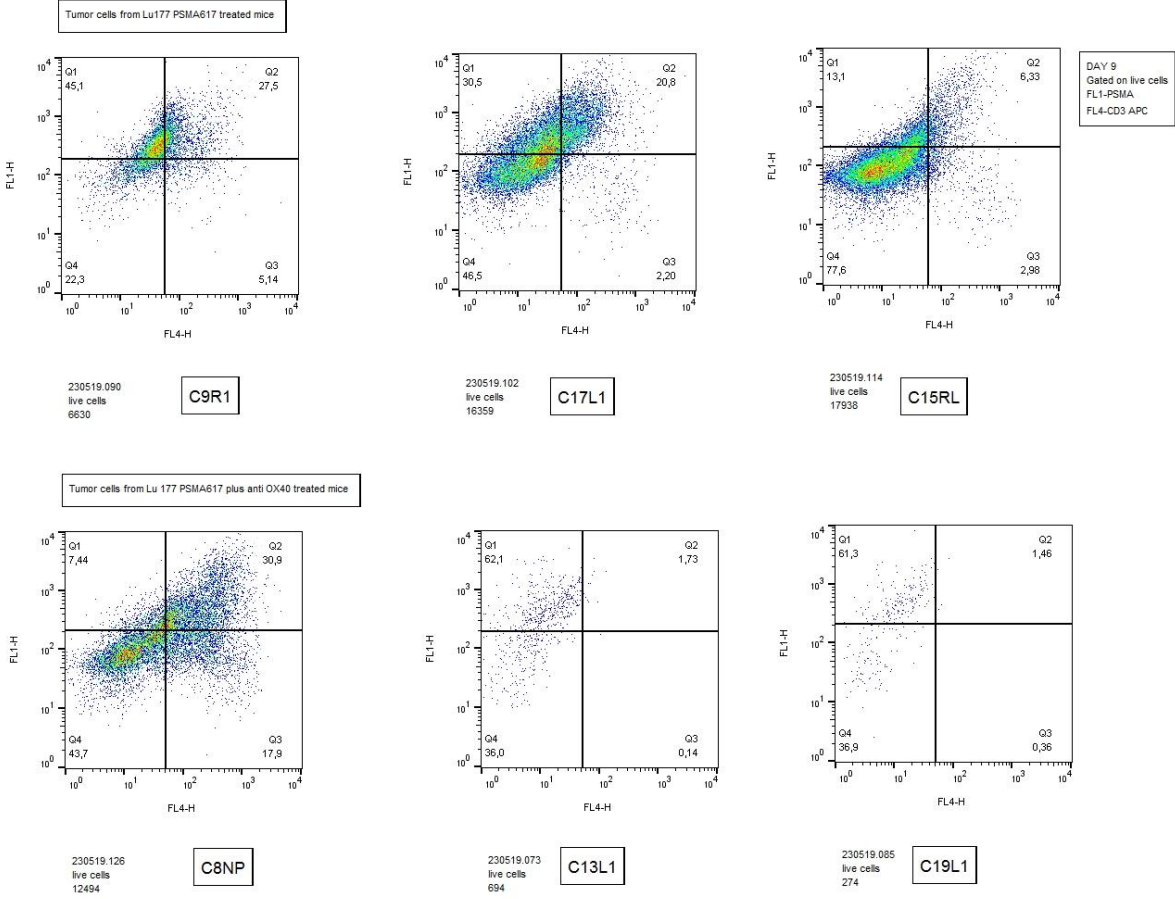


Figure C-2: Flow cytometry data depicting varying degrees of PSMA-expression and TIL-infiltration in the tumours excised 9 days post (first) treatment. Of note is low number of cells in tumours C13L1 (~900 mm³ at excision timepoint) and C19L1(~860 mm³ at excision timepoint).

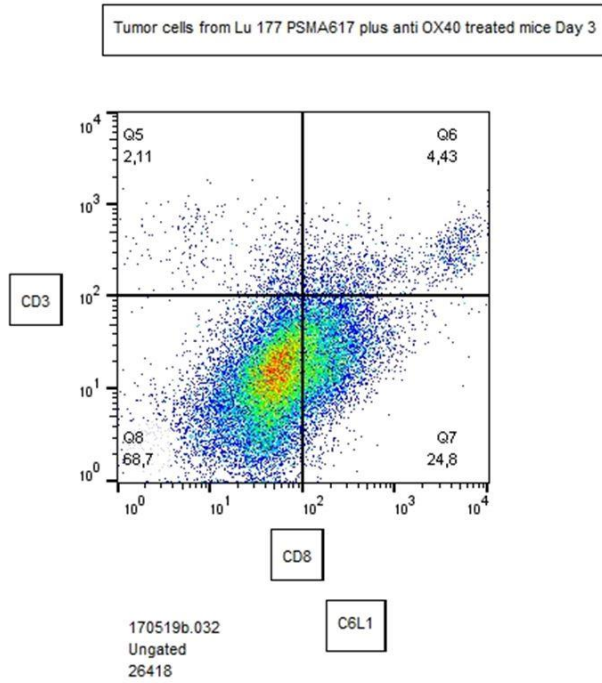
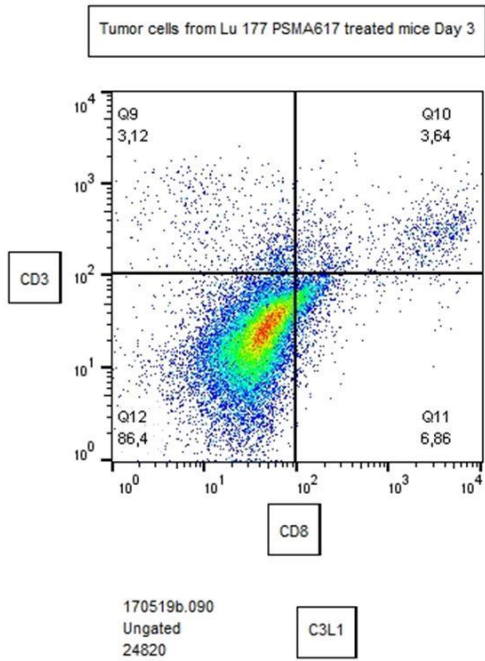


Figure C-3: Flow cytometry data depicting larger proportion of CD3⁺CD8⁺ tumour-infiltrating cytotoxic T-lymphocytes in Treatment Group #1.